Improving thermoelectric properties of oxide semiconductor thin films by controlling carrier concentration and crystal structure

(キャリア密度と結晶構造制御による
酸化物半導体薄膜の熱電性能改善)

Jenichi Clairvaux Escubio Felizco

February 2021

Division of Materials Science
Graduate School of Science and Technology
Nara Institute of Science and Technology

Table of Contents

Chapter 1. Introduction

1.1. Thermoelectric Device Technology

1.1.1. Thermoelectric Generation Principle

The thermoelectric effect was first discovered by T. J. Seebeck in 1821, where he demonstrated that an electromotive force can be generated by applying heat at the junction between two different electrically conducting materials. This phenomenon was later referred to as the Seebeck effect [1]. Thermoelectric generators (TEGs) are therefore defined as those capable of directly converting heat to electrical energy without any moving or noisy components through the Seebeck effect [1-2]. The working principle of a conventional TEG is depicted in Fig. 1 [3]. It consists of an n-type and a p-type semiconductor connected by a metal. When a thermal gradient is applied between the semiconductors, the holes in the p-type semiconductor and the electrons from the n-type semiconductor flows from the hot to the cold reservoir. The maximum thermoelectric efficiency of an ideal TEG can be approximated using the ff. equation, with the first term inside the parentheses being the Carnot efficiency [4]:

$$efficiency_{max} = (\frac{T_H - T_C}{T_H})(\frac{\sqrt{1+zT}-1}{\sqrt{1+zT}+\frac{T_c}{T_H}})$$

where T_H and T_C are the temperatures at the hot and cold reservoir, respectively, and zT is the dimensionless figure of merit. The zT defines how efficiently the thermal energy can be converted into electrical energy in a material, and is expressed as follows:

$$zT = \frac{S^2\sigma}{\kappa}$$

where S represents the Seebeck coefficient, σ is the electrical conductivity and κ is the thermal

conductivity. The numerator component $S^2\sigma$, which is commonly referred to as the thermoelectric power factor (*PF*), is the electrical contribution to the figure of merit. The aim is therefore to develop materials with high *PF* and low κ. Several studies are devoted to optimizing the PF, since there is a known coupling but inverse relation between *S* and σ. This coupling effect arises from their opposing relationship with carrier concentration (*n*), in which *S* varies inversely while σ relates linearly. This therefore drives research towards solving this coupled relationship in order to maximize the *PF*. The key to lowering κ has less to do with the optimization of *n*, since this property is mostly dominated by lattice contributions [1].

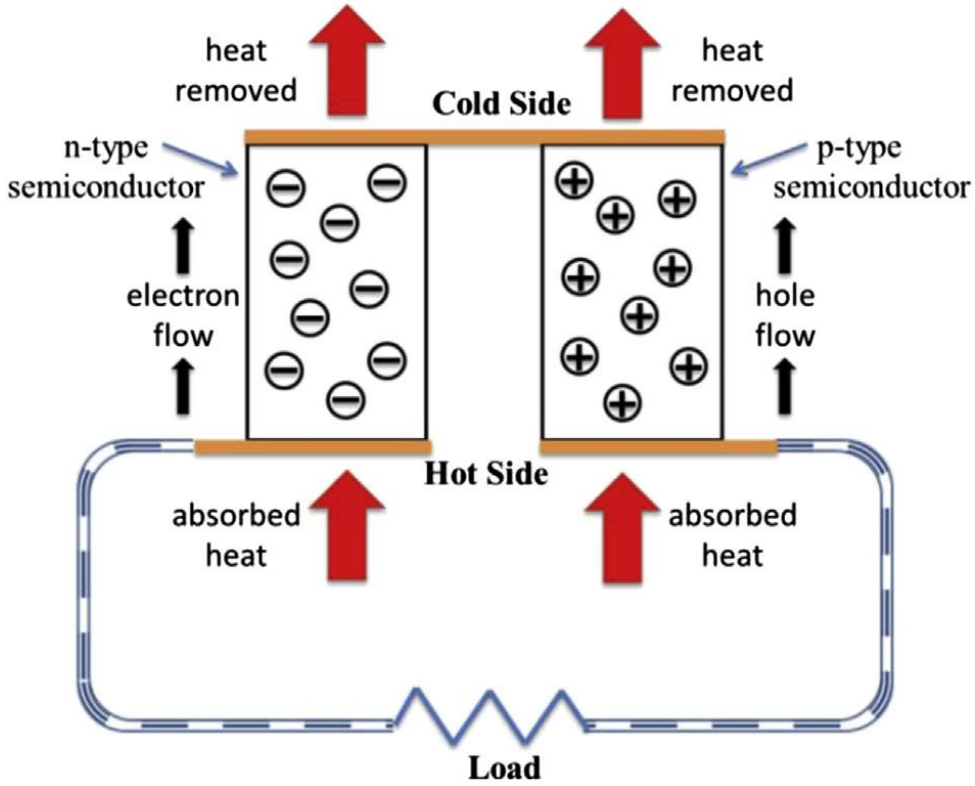

Fig. 1.1. The working principle of a typic thermoelectric generator (TEG) [3]. Reproduced with permission from ref 3. Copyright 2015 Elsevier.

TEGs have been of remarkable interest as sustainable energy harvesting devices. Heat from natural sources such as solar, geothermal and body heat, as well as ubiquitous waste heat

from the transportation and industrial sector, are widely abundant sources of energy. In addition, reducing heat in the surroundings is a valuable contribution towards solving current problem on global warming. However, harvesting heat at a relatively low temperature, such as body heat, is advantageous for future wearable devices for the Internet of Things (IoT). For wearable TEGs, it is essential to develop transparent and flexible devices. For example, Uenuma, et. al has demonstrated a flexible transverse-type InGaZnO TEG deposited onto polyethylene naphthalate (PEN) substrates [5]. Another is the study by Ruoho, et. al, wherein they designed a transparent and flexible thermal touch panel based on Al-doped ZnO deposited via atomic layer deposition [6]. Kim, et. al also developed a Bi_2Te_3/Sb_2Te_3 TEG deposited onto glass fabric by screen printing [7].

However, it is noteworthy that in order to be utilized as an energy source for IoTs, the power generated by a TEG should range within microwatts or milliwatts. Illustrated in Fig. 1.2 is the relationship between power density and ΔT. In order to achieve high power density, thermoelectric materials with high PF are certainly needed. However, lower *PF* materials (~0.1 mW/mK^2) can be utilized when a large ΔT is applied, or the device area is sufficiently large.

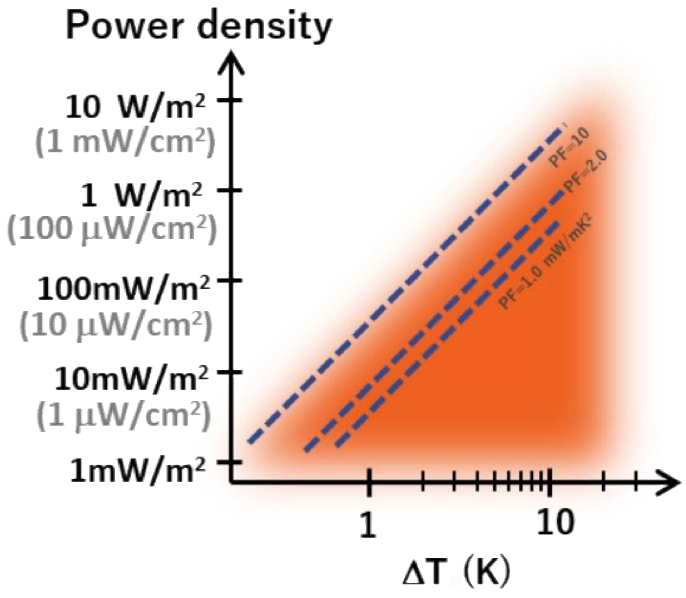

Fig. 1.2. Graph showing the ΔT and power density relationship.

1.1.2. Improving the Thermoelectric Power Factor

1.1.2.1. Optimizing the Carrier Concentration

As established in the previous section, one way of realizing competitive thermoelectric performance is by maximizing the PF through modulation of *n*. A great number of previous papers propose various means by which *n* can be controlled. Jiang, et. al. suggested a point defect chemistry approach for $Mg_2(Si, Sn)$ solid solutions. Effective *n* tuning can be attributed to Sb dopants, Mg vacancies and Mg interstitials in $Mg_2Si_{0.4}Sn_{0.6-x}Sb_x$ [8]. Band structure engineering is another effective technique, as demonstrated by Pei, et. al in MgTe-alloyed PbTe [9]. They also used this to decrease the temperature-dependence of *n*, which allows the PbTe to be used for a wider temperature range [9].

1.1.2.2. Crystal Structure Engineering

Engineering the crystal structure is also an efficient method for improving the *zT*. In a study by Abutaha, et. al, a shift in the crystal orientation of ZnO thin films caused by changing the substrate temperature during laser deposition led to a significant improvement in σ [10]. A synchronous increase in *S* and σ was successfully achieved in Sb_2Te_3 thin films by microstructure control and crystal orientation shifting as reported by Shen, et. al [11]. According to Brinks, et. al, controlling the grain size and crystallinity of Na_xCoO_2 led to doubling the magnitude of the *PF* [12].

1.1.2.3. Charge Carrier Quantum Confinement

An improvement in the *PF* can also be achieved by utilizing low dimensional materials. This can mainly be attributed to successfully decoupling *S* and σ. Introducing nanoscale

components brings upon quantum confinement effects, which is observed when the material size becomes almost comparable to the electron wavelength, which reveals unique electronic and optical properties compared to the bulk materials [13-14]. Furthermore, the high internal interfacial density exhibited by low dimensional materials can be advantageous to lowering the κ. Low dimensional materials include quantum dots, nanostructures (nanoparticles, nanowires, nanorods, nanotubes, among others), and two-dimensional quantum well systems (superlattice and two-dimensional electron gas) [13]. The *zT* of silicon nanowires was observed to increase by 100-fold compared to bulk Si, as published by Boukai, et. al [15]. Theoretical calculations predicted that a $zT = 14$ can be reached by Bi_2Te_3 nanowires with thicknesses of around 5Å [16]. Bi_2Te_3/Sb_2Te_3 superlattice films were able to display a *zT* of 2.4, as revealed in a study by Venkatasubramanian, et al [17]. Ohta, et. al also reported a giant enhancement in *S* arising from an electric field-induced two-dimensional electron gas, which is a system wherein the electrons are laterally confined in a sheet-like highly conductive layer. This phenomenon can usually be observed at the interface of a thermoelectric material and a dielectric. They were able to observe this phenomenon in several material systems, such as in AlGaN/GaN, calcium aluminum nanoporous glass/$SrTiO_3$, and $SrTi_{1-x}Nb_xO_3$/SrTiO3 superlattices [18-20]. It has also been demonstrated by Shimizu, et. al that an increase by about two orders of magnitude is possible with ZnO single crystals when contacted with an ionic liquid [21].

1.2. Thermoelectric Materials

1.2.1. State-of-the-art Thermoelectric Materials

One of the pioneer materials in thermoelectric applications is Bismuth [1]. Since it is characterized with a negative Seebeck coefficient, bismuth is often paired with antimony, which has a positive Seebeck coefficient. Nowadays, the most conventionally used

thermoelectric material is Bi_2Te_3, which possesses a PF reaching up to 18 mW/mK^2 and a zT of more than 2 [22-23]. Other chalcogenide materials are also utilized for thermoelectric purposes, such as PbTe, SiGe, Sb_2Te_3 and SnSe. Compounds classified as skutterudites, which exhibit a small lattice conductivity embodying the phonon-glass electron-crystal concept, are also well-known thermoelectric materials. Clathrates are another type of compounds with low lattice conductivity and containing open structures where loosely bound guest atoms can be incorporated [1, 4, 24]. Oxides are also being explored because they are stable and chemically inert, while organic materials such as have the advantage of ease of processing and superb flexibility [1].

Fig. 1.2 shows the S vs σ relationship of several thermoelectric materials. The dashed lines represent the power factor values by increasing order of magnitude. Bi-Te-related materials dominate with superior *PF*, while oxides and organic materials needs improvement.

1.2.2. Oxides

Among potential thermoelectric materials, oxides are currently being intensively studied owing to their good chemical and thermal stability, low toxicity and high abundance [1]. Their superior stability makes them good candidates even for high thermal harvesting. Oxides were initially not regarded as potential thermoelectric materials owing to their low zT values, until the observation of competitive performance by the p-type oxide $NaCo_2O_4$ [25]. Recently, other cobaltites such as $Ca_3Co_4O_9$, $Co_3Co_4O_9$, $LaCoO_3$ and $Ca_3Co_4O_9$ are also seriously considered as p-type thermoelectric oxides [26]. On the other hand, one of the best n-type oxides is $SrTiO_3$, owing to its high effective mass and room temperature *PF* at par with Bi_2Te_3. Other promising n-type thermoelectric oxides involve $CaMnO_3$ and ZnO [26].

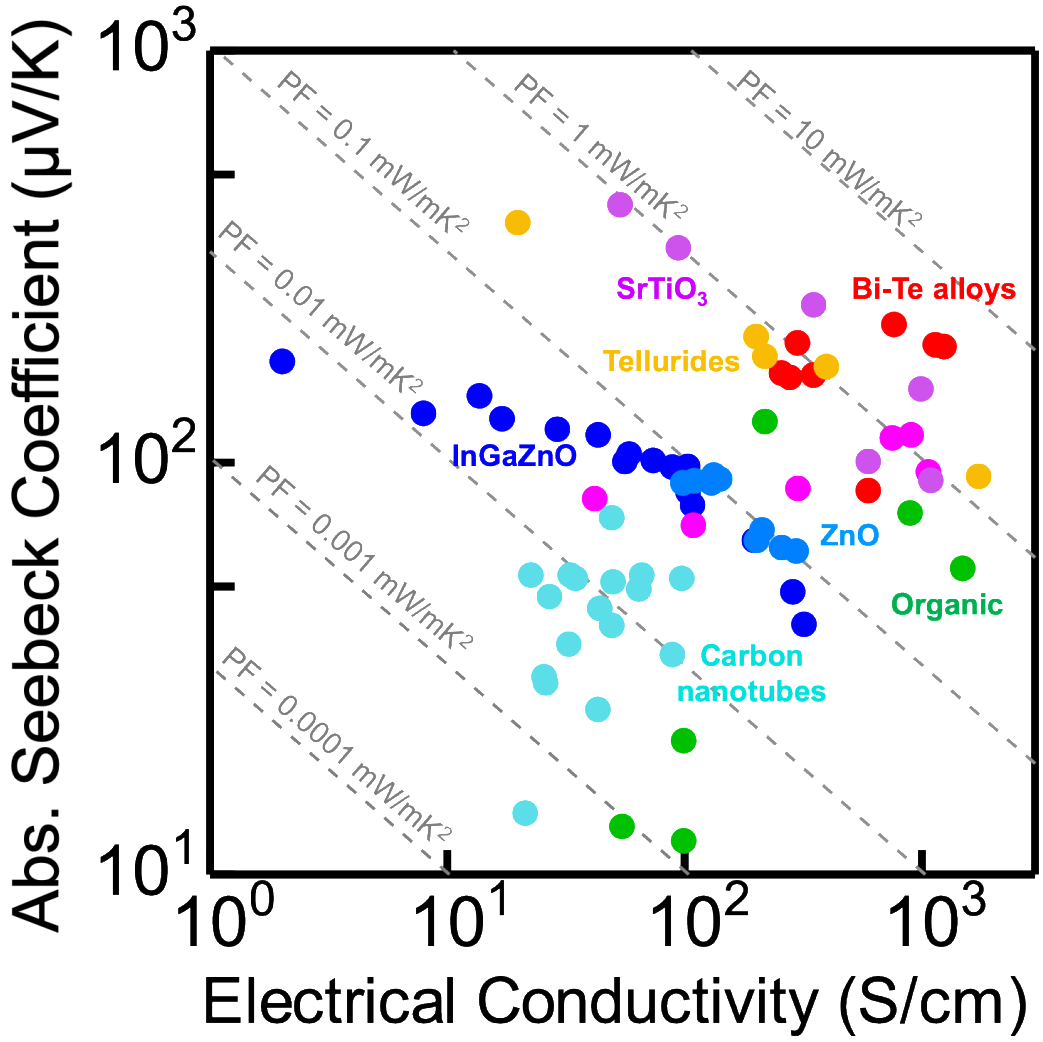

Fig. 1.2. Thermoelectric properties of several types of thermoelectric materials.

1.3. ZnO-related Thermoelectric Thin Films

1.3.1. ZnO Thin Films

Zinc oxide (ZnO) is one of the most studied n-type transparent thermoelectric oxides. First, it is non-toxic, highly abundant and cheap, which makes it a good candidate material for large scale fabrication. Second, its good chemical and thermal stability allows ZnO to be used not only in low temperature thermoelectric applications, but also at the higher temperature

range. Third, its good transparency and flexibility enables its applicability in transparent thermoelectric devices. Lastly, its electrical properties are readily tunable by defect engineering [27-30]. ZnO thin film fabrication exist in a number of several techniques, such as atomic layer deposition [29], pulsed laser deposition [30], sputtering [31] and solution-based processes [32-33]. It has been utilized in many electronic applications including solar cells [34], gas sensors [35], thin film transistors [36], light emitting diodes [37], transparent conductive electrodes [38], and thermoelectric devices [39-42], among others.

The thermoelectric properties of ZnO has been reported in several previous papers. Kim, et. al. reported a significant improvement in the thermoelectric properties of atomic layer deposited ZnO thin films by changing the oxidant from the commonly used deionized H_2O to ozone [39]. According to Liu, et. al, the power factor of ZnO thin films can be significantly enhanced when incorporated with ZnO nanowires, and that the properties depend on the nanowire content [40]. Ab-initio calculations by Wang, et. al also predicted that single-walled ZnO nanotubes exhibit improved zT compared to ZnO nanowires likely owing to a significantly smaller thermal conductivity [41]. Baghdadi, et. al compared the thermoelectric properties of ZnO nanoparticles and nanorods, and reported that nanorods exhibit better performance owing to the reduced interface barriers and increased electron mean free path [42].

Doping the ZnO thin films greatly impacted its thermoelectric properties. Ruoho, et. al. doped pure ZnO with Al using atomic layer deposition, which resulted in an increase in the power factor at a certain optimum amount. They also found that changing the cluster distribution of Al within the ZnO can further improve the thermoelectric properties as a result of optimizing the trade-off between crystal growth interruption and enhanced carrier density [29]. In the study by Barasheed, et. al, Ga-doped ZnO prepared by sol-gel method exhibited a 17% increase in power factor compared to pure ZnO films at the high temperature range (>600 K). Ga doping induced an almost metallic behavior on the ZnO thin films, which cannot be

achieved by pure ZnO even when subjected to high temperature annealing under a reducing atmosphere [43]. Thermoelectric nanogenerators have also been fabricated based on Sb-doped ZnO nanobelts [44]. However, only a few dopant elements have been considered for ZnO for thermoelectric device applications.

1.3.2. InGaZnO Thin Films

InGaZnO has recently been gaining traction as a next generation material for transparent and flexible electronic devices. This multicomponent oxide sports a distinctive layered structure of In_2O_3, Ga_2O_3 and ZnO, which are arranged differently depending on the crystallinity, as depicted in Fig. 1.3 [45]. InGaZnO has been fabricated using a wide array of vacuum and solution-process techniques such as pulse laser deposition [47], sputtering [48], atomic layer deposition [49], sol-gel coating [50], inkjet printing [51] and spray pyrolysis [52].

The impressive electrical properties of InGaZnO accounts for its popularity as an electronic device material. It displays superior carrier mobility, low leakage current and easily controllable carrier concentration [53-57]. In addition, its excellent optical transparency and low temperature deposition and processing makes InGaZnO highly desirable for transparent flexible devices. It has long been a well-established candidate for thin film transistor applications since its first use in 2004 by Nomura, et. al [53]. It also served as a promising semiconductor material for resistive switching memory devices [58]. Additionally, its energy applications such as in solar cells and thermoelectric generators have also been previously studied [48, 59].

InGaZnO has been regarded as having low thermal conductivity compared to other ZnO-related materials, which makes it a promising thermoelectric material [45-46]. While the values differ depending on the crystallinity and porosity as demonstrates in Fig. 1.4, the thermal conductivity of InGaZnO thin films range from 1-4 W/mK^2 [45]. The structural randomness

from having three constituent cations could be responsible for this. However, its thermoelectric power factor remains well below 0.1 mW/mK^2, which needs to be improved in order to fully utilize InGaZnO as a thermoelectric material.

Several past literatures have been dedicated to structural and defect engineering of InGaZnO improve its thermoelectric power factor, whether in amorphous, crystalline or nanostructured form [48, 60]. Fujimoto, et. al optimized the thermoelectric power factor of amorphous InGaZnO thin films by controlling the amount of O_2 in the deposition atmosphere during RF magnetron sputtering. This allowed great control over the carrier concentration, which led to optimizing the power factor up to 0.088 mW/mK^2 [48]. Ohta, et. al demonstrated a significant enhancement in the Seebeck coefficient of superlattice a-InZnO/a-InGaZnO thin films owing to quantum confinement effects [61]. Seo, et. al. saw drastic improvements in the thermoelectric properties of single crystalline InGaZnO thin films with a ZnO buffer layer by thermal and plasma treatments [62]. The improvement in Seebeck coefficient was attributed to the formation of a perfect crystalline superlattice structure during deposition and thermal treatment, which remained undisturbed when plasma treatment was utilized to increase the electrical conductivity. A study by Nguyen, et. al. reported a five-fold enhancement in the thermoelectric figure of merit by reducing the In and Ga amounts in an InGaZnO thin film to achieve optimum doping effects. They established that excess amounts of In and Ga leads to the formation of unwanted secondary phases, which could deteriorate the carrier transport properties [63]. However, despite these past efforts, the thermoelectric performance of InGaZnO remained low, driving the search for other techniques to improve its power factor.

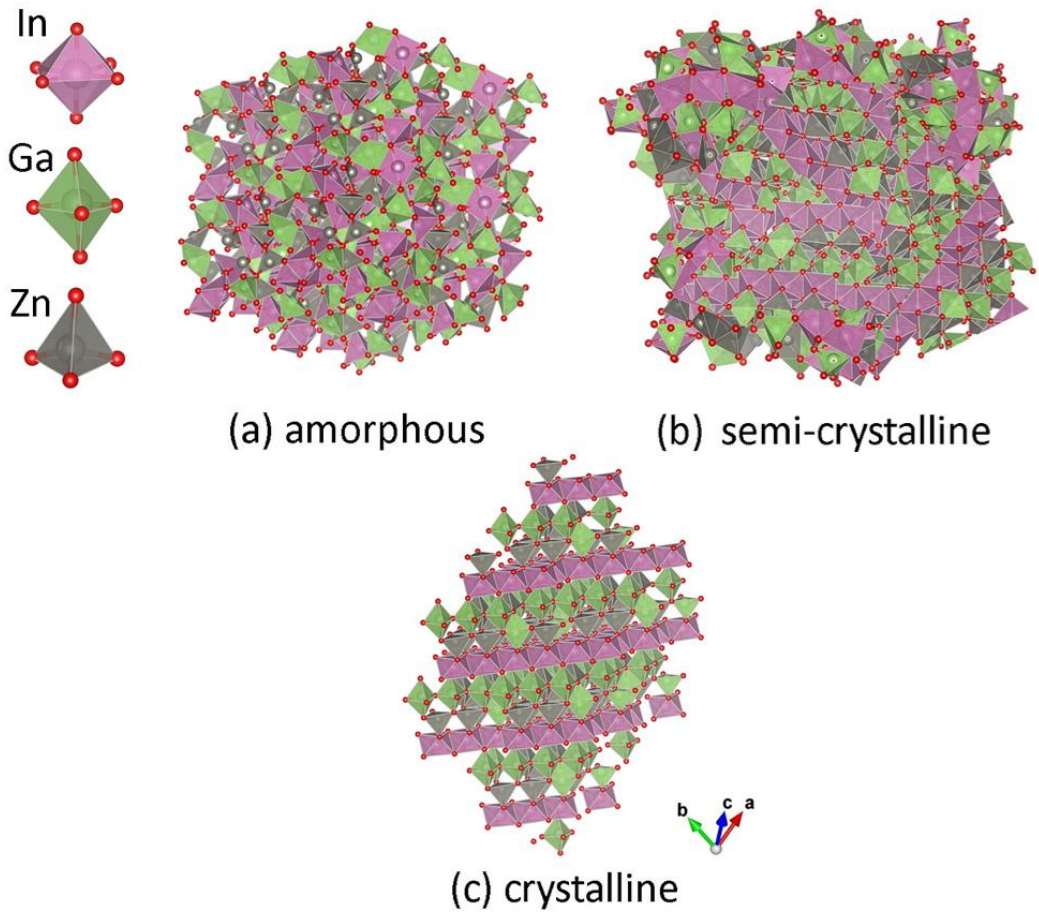

Fig. 1.3. Crystal structure of (a) amorphous, (c) semi-crystalline and (c) crystalline InGaZnO. Reproduced with permission from ref 45. Copyright 2016 American Chemical Society.

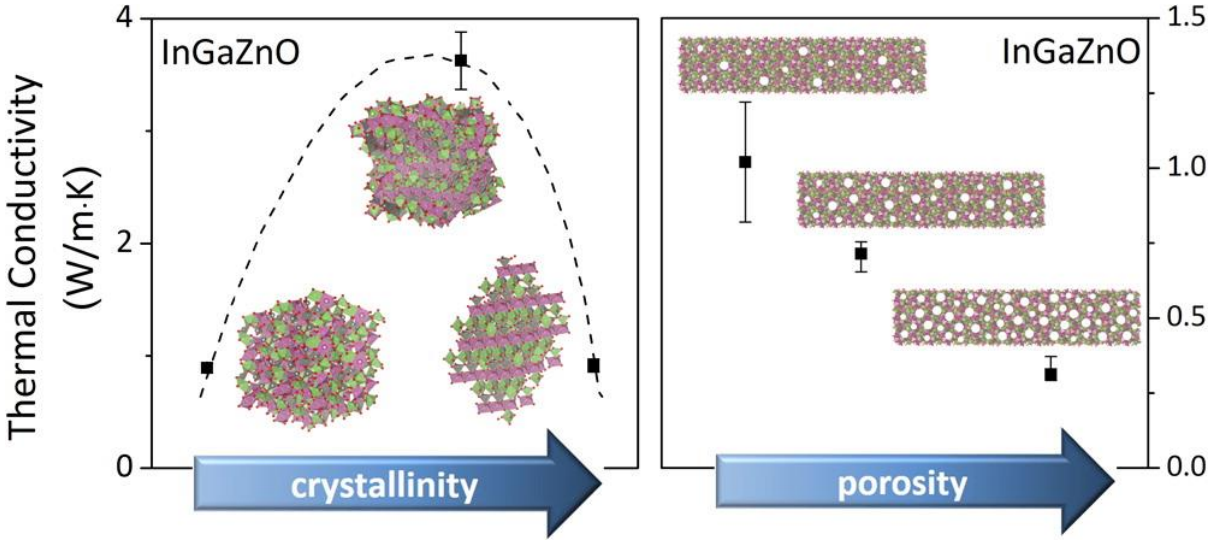

Fig. 1.4. Thermal conductivity of InGaZnO depending on thin film crystallinity and porosity. Reproduced with permission from ref 45. Copyright 2016 American Chemical Society.

1.4. Objectives and Research Outline

Thermoelectric generation in ZnO-related thin films is of significant interest in developing environment-friendly, transparent and wearable energy devices. However, their thermoelectric device performance remains inferior to other state of the art materials. To improve their properties, focusing on the thermoelectric power factor ($PF = S^2\sigma$) is a vital but challenging task owing to the coupled but inverse relationship of σ and S with carrier concentration. Thus, the main objective of this research is to enhance the thermoelectric power factor of ZnO-related thin films.

This research proposes three techniques to improve the thermoelectric power factor of ZnO-related thin films. The first method is by introducing relatively less-explored dopant layers such as TiO_2 and HfO_2 within a ZnO thin film by atomic layer deposition. By using this technique, there is a high control over the dopant concentration and distribution. The second method is by incorporating hydrogen in the post-deposition annealing atmosphere of InGaZnO thin films. This solution can be easily integrated at the end of device production workflow without compromising the standard frontend deposition process for other electronic applications. The last method is by modulating the carrier concentration in the InGaZnO thin film incorporated in a thin film transistor as an effect of gate voltage application. In this technique, the gate voltage creates an electron confinement region near the InGaZnO/gate insulator interface, causing an upsurge in the electrical conductivity without a severe decrease in Seebeck coefficient. As a result, the Seebeck coefficient and electrical conductivity are successfully decoupled.

The general outline of this research is as follows:

Chapter 1 provides a brief introduction about thermoelectric devices and materials. The general principle of thermoelectric generation is discussed. The importance and techniques for improving the thermoelectric power factor are presented in detail. Oxide materials and their

thermoelectric properties are introduced.

Chapter 2 explored the use of atomic layer deposition to synthesize multilayered TiO_2/ZnO and HfO_2/ZnO thin films. It was determined that both doped ZnO thin films outperformed the pure ZnO in terms of power factor and cyclic thermal stability. The amount of dopant concentration was also optimized to reach peak thermoelectric power factor.

Chapter 3 aims to determine the effect of post-deposition annealing conditions on the thermoelectric power factor of amorphous, c-axis aligned crystalline and crystal-embedded c-axis aligned crystalline InGaZnO thin films. Depending on the crystallinity of the thin films, the annealing atmosphere composition affects the power factor differently. Pure nitrogen annealing was established to be best for amorphous InGaZnO, while incorporating a small amount of hydrogen leads to the highest power factor for crystalline InGaZnO.

Chapter 4 investigates the thermoelectric generation in an InGaZnO thin film transistor. The InGaZnO/SiO_2 thin film transistor in its ON state exhibited significantly higher power factor compared to pristine InGaZnO thin films owing to the formation of a charge accumulation layer in the InGaZnO/SiO_2. This charge accumulation layer suppressed the strong coupling between the Seebeck coefficient and electrical conductivity, which is a phenomenon commonly observed in pristine InGaZnO thin films.

Chapter 5 provides an overall summary of the research and lays out recommendations for future studies.

References

1) H. Goldsmid, Introduction to Thermoelectricity, 2nd Ed., Springer-Verlag Berlin Heidelberg, 2010.

2) F. DiSalvo, Science, 285, 5428, 703-706, 1999.

3) W. Zhu, Y. Deng, M. Gao, Y. Wang, J. Cui and H. Gao, Energy 89, 106-117, 2015.

4) Z. Soleimani, S. Zoras, B. Ceranic, S. Shahzad, and Y. Cui, Sustainable Energy Technologies and Assessments 37, 100604, 2020.

5) M. Uenuma, K. Umeda, J. Felizco, D. Senaha, and Y. Uraoka, J. Elec. Mater. 48, 1971–1975, 2019.

6) Ruoho, M.; Juntunen, T.; Alasaarela, T.; Pudas, M.; Tittonen, I. Transparent, Flexible, and Passive Thermal Touch Panel Adv. Mater. Technol. 1, 1600204, 2016.

7) S. Kim, J. We and B. Cho, Energy Environ. Sci., 7, 1959–1965, 2014.

8) G. Jiang, J. He, T. Zhu, C. Fu, Z. Liu, L. Hu and X. Zhao, Adv. Funct. Mater. 24, 24, 2014.

9) Y. Pei, A. LaLonde, N. Heinz, X. Shi, S. Iwanaga, H. Wang, L. Chen and G. Snyder, Adv. Mater 23, 47, 2011.

10) A. Abutaha, S. Kumar and H. Alshareef, Appl. Phys. Lett. 102, 053507, 2013.

11) S. Shen, W. Zhu, Y. Deng, H. Zhao, Y. Peng and C. Wang, Appl. Surf. Sci 414, 197-204, 2017.

12) P. Brinks, B. Kuiper, E. Breckenfeld, G. Koster, L. Martin, G. Rijnders, and M. Hujiben, Adv. Energy Mater. 4, 8, 2014.

13) M. Dresselhaus, G. Chen, M. Tang, R. Yang, H. Lee, D. Wang, D. Z. Ren, J. Fleurial and P. Gogna, Adv. Mater 19, 8, 2007.

14) O. Neikov, S. Naboychenko and N. Yefimov, Handbook of Non-Ferrous Metal Powders, 2nd Ed., Elsevier, 2019.

15) A. Boukai, Y. Bunimovich, J. Tahir-Kheli, W. Goddard and J. Heath, Nature 451, 168–171, 2008.

16) L. Hicks, M. Dresselhaus Phys. Rev. B Condens. Matter 47, 24, 16631–16634, 1993.

17) R. Venkatasubramanian, E. Siivola, T. Colpitts and B. O'Quinn, Nature 413, 597–602, 2001.

18) H. Ohta, T. Mizuno, S. Zheng, T. Kato, Y. Ikuhara, K. Abe, H. Kumomi, K. Nomura and H. Hosono, Adv. Mater. 24, 740-744, 2012.

19) H. Ohta, S. Kim, S. Kaneki, A. Yamamoto, and T. Hashizume, Adv. Sci. 5, 1700696, 2018.

20) H. Ohta, S. Kim, Y. Mune, T. Mizoguchi, K. Nomura, S. Ohta, T. Nomura, Y. Nakanishi, Y. Ikuhara, M. Hirano, H. Hosono and K. Koumoto, Nature Materials 6, 129–134, 2007.

21) S. Shimizu, M. Bahramy, T. Iizuka, S. Ono, K. Miwa, Y. Tokura and Y. Iwasa, PNAS 113, 23, 2016.

22) M. Ahmad, K. Agarwal and B. Mehta, J. Appl. Phys. 128, 035108, 2020.

23) H. Lv, H. Liu, J. Shi, X. Tang and C. Uher, J. Mater. Chem. A 1, 6831-6838, 2013.

24) S. Twaha, j. Zhu, Y. Yan and B. Li, Renewable and Sustainable Energy Reviews 65, 698–726, 2016.

25) H. Yakabe, K. Kikuchi, I. Terasaki, Y. Sasago and K. Uchinokura, 16th International Conference on Thermoelectrics, Dresden, IEEE, New York, 523, 1997.

26) J. Fergus, J. Eur. Ceram. Soc. 32, 3, 525-540, 2012.

27) Z. Zhou, G. Ren, X. Tan, R. Liu, C. Liu, Y. Lin, C. Nan, J. Mater. Chem. A 6, 24128-24135, 2018.

28) P. Jood, R. Mehta, Y. Zhang, G. Peleckis, X. Wang, R. Siegel, T. Borca-Tasciuc, S. Dou,

G. Ramanath, Nano Lett. 11, 4337-4342, 2011.

29) M. Ruoho, V. Pale, M. Erdmanis, and I. Tittonen, Appl. Phys. Lett. 103, 203903, 2013.

30) Y. Kang, K. Jang, C. Lee, S. Cho, ACS Appl. Mater. Interfaces 8, 5216−5223, 2016.

31) P. Fan, Y. Li, Z. Zheng, Q. Lin, J. Luo, G. Liang, M. Zhang, M. Chen, Appl. Surf. Sci. 284, 145–149, 2013.

32) S. Saini, P. Mele, P.; H. Honda, K. Matsumoto, K. Miyazaki, L. Molina Luna, P. Hopkins, J. Electron. Mater. 44, 6, 1547-1553, 2015.

33) D. Lee, K. Kim, S. Kim, J. Kwon, J. Xu, K. Kim, J. Mater. Chem. C 1, 4761-4769, 2013.

34) C. Pelicano and H. Yanagi, J. Mater. Chem. C, 5, 8059-8070, 2017.

35) P. Mitra, A. Chatterjee and H. Maiti, Mater. Lett. 35, 1-2, 33-38, 1998.

36) P. Carcia, R. McLean and M. Reilly, J. SID 13, 7, 2005.

37) A. Tsukazaki, A. Ohtomo, T. Onuma, M. Ohtani, T. Makino, M. Sumiya, K. Ohtani, S. Chichibu, S. Fuke, Y. Segawa, H. Ohno, H. Koinuma and M. Kawasaki, Nature Mater. 4, 42-46, 2005.

38) J. Lee, K. Ko and B. Park, J. Crys. Growth 247, 1-2, 119-125, 2003.

39) H. Kim, Z. Wang, M. Hedhili, N. Wehbe, H. Alshareef, Chem. Mater. 29, 2794−2802, 2017.

40) S. Liu, G. Li, L. Xiao, B. Jia, Y. Gao and Q. Wang, Appl. Surf. Sci 436, 354-361, 2018.

41) C. Wang, Y. Wang, G. Zhang and C. Peng, J. Phys. Chem. C 117, 41, 21037–21042, 2013.

42) N. Baghdadi, N. Salah, A. ALshahrie, A. Ansari and K. Koumoto, Ceram. Int. 2020.

43) A. Barasheed, S. Kumara, H. Alshareef, J. Mater. Chem. C 2013, 1, 4122-4127.

44) Y. Yang, K. Pradel, Q. Jing, J. Wu, F. Zhang, Y. Zhou, Y. hang and Z. Wang, ACS Nano 6, 8, 6984–6989, 2012.

45) B. Cui, L. Zheng, D. Keane, M. Bedzyk, D. Buchholz, R. Chang, X. Yu, J. Smith, T.

Marks, Y. Xia, A. Facchetti, J. Medvedeva and M. Grayson, J. Phys. Chem. C 120, 14, 7467–7475, 2016.

46) T. Yoshikawa, T. Yagi, N. Oka, J. Jia, Y. Yamashita, K. Hattori, Y. Seino, N. Taketoshi, T. Baba and Y. Shigesato, Appl. Phys. Express 6, 021101, 2013.

47) M. Orita, H. Ohta, M. Hirano, S. narushima and H. Hosono, Philosophical Magazine B 81, 501-515, 2001.

48) Y. Fujimoto, M. Uenuma, Y. Ishikawa, and Y. Uraoka, AIP Adv. 5, 097209, 2015.

49) A. Illiberi, B. Cobb, A. Sharma, T. Grehl, H. Brongersma, F. Roozeboom, G. Gelinck and P. Poodt, ACS Appl. Mater. Interfaces, 7, 3671–3675, 2015.

50) J. Kim, D. Seo, C. Ahn, S. Shin, H. Cho and H. Cho, J. Mater. Chem. 32, 2012.

51) G. Kim, H. Kim, H. Shin, B. Ahn, K. Kim and H. Kim, Thin Solid Films 517, 14, 4007-4010, 2009.

52) H. Liu, C. Hung and W. Hsu, IEEE Electron Device Lett. 39, 10, 2018.

53) K. Nomura, H. Ohta, A. Takagi, T. Kamiya, M. Hirano and H. Hosono, Nature, 432, 488–492 (2004).

54) H. Hosono, Nature Electronics, 1, 428, (2018).

55) Y. Zhao, Z. Wang, G. Xu, L. Cai, T. Han, A. Zhang, Q. Wu, R. Wang, T. Huang, P. Cheng, S. Chang, D. Bao, Z. Zhao, M. Wang, Y. Huang, and Y. Yang, Adv. Funct. Mater. 30, 2003285, 2020.

56) H. Zan, C. Yeh, H. Meng, C. Tsai and L. Chen, Adv. Mater. 24, 3509-3514, 2012.

57) Y. Rim, H. Chen, X. Kou, H. Duan, H. Zhou, M. Cai, H. Kim and Y. Yang, Adv. Mater. 26, 4273-4278, 2014.

58) K. Kado, M Uenuma, K. Sharma, H. Yamazaki, S. Urakawa, Y. Ishikawa and Y. Uraoka, Appl. Phys. Lett. 105, 123506, 2014.

59) J. Hou, S. Chang, C. Wu, H. Hong, and T. Hsueh, ECS J. Solid State Sci. Technol. 6,

Q120–Q122, 2017.

60) J. C. Felizco, M. Uenuma, D. Senaha, Y. Ishikawa, and Y. Uraoka, Appl. Phys. Lett. 111, 033104 (2017).

61) H. Ohta, R. Huang and Y. Ikuhara, Phys. Stat. Sol. (RRL) 3, 105-107, 2008.

62) D. Seo, S. Shin, H. Cho, B. Kong, D. Whang, H. Cho, Acta Materialia 59, 6743–6750, 2011.

63) N. Nguyen, T. Nguyen, Y. Liu, M. Aminzare, A. Pham, S. Cho, D. Wong, K. Chen, T. Seetawan, N. Pham, H. Ta, V. Tran, and T. Phan, ACS Appl. Mater. Inter. 8, 49, 33916–33923, 2016.

Chapter 2. Enhanced Thermoelectric Transport and Stability in Atomic Layer Deposited HfO_2/ZnO and TiO_2/ZnO Sandwiched Multilayer Thin Films

2.1. Introduction

Zinc oxide (ZnO) is one of the most studied n-type transparent semiconductor oxides, as its electronic properties can easily be tuned by controlling the defect densities [1-7]. ZnO thin films can be deposited by a wide variety of fabrication techniques, such as atomic layer deposition [8-13], pulsed laser deposition [14], sputtering [15] and solution-based processes [16-17]. However, when doped ZnO thin films are desired, it would be best to conduct both the deposition and doping in a single step to minimize cost, exposure to contamination, processing time and effort. Considering these, atomic layer deposition (ALD) is the ideal technique, as deposition and doping can be conducted simultaneously by simply varying the precursors being pulsed. It is a type of chemical vapor deposition that occurs via sequential, self-limiting surface reactions, precisely growing the materials layer by layer [8-12]. ALD has been gaining interest owing to its excellent control over film thickness and uniformity down to the Ångstrom scale. In addition, ALD allows high controllability over the amount and distribution of dopants. One disadvantage of pure ALD ZnO, though, is its low electrical stability at high temperatures [18-19]. While this could be overcome by the incorporation of other elements, thermoelectric devices based on doped ALD ZnO thin films have been mainly limited to Al and Ga [5, 9, 20-22]. Although Al has been a well-established dopant, ALD Al-doped ZnO (AZO) has been reported to exhibit low doping efficiency of only about 13 % [17]. Additionally, group III elements have relatively low stability when doped in ZnO owing to the

low electronegativity difference with O [23]. Therefore, alternative dopants should be explored which can simultaneously improve thermoelectric properties and thermal stability.

Group IV elements (Ti, Hf, Zr, etc.) are expected to cause electrical stability when doped to ZnO due to their high affinity for O [15]. However, these still remain rarely explored as dopants for thermoelectric applications of ZnO. Among the group IV elements, Hf has the highest bond dissociation energy with oxygen (~800 kJ/mol), which can potentially form a stronger structure when Hf substitutes with Zn [24]. Moreover, Hf was previously reported to suppress the formation of oxygen vacancies consequently increasing electrical stability [25-27]. Ti, on the other hand, was described to have a higher doping efficiency compared to the more commonly used Al [19]. Several reports have established significant improvements in the electrical properties of both Ti and Hf-doped ZnO, but very few are focused on discussions about its thermoelectric properties. In these few reports, the power factors are still rather low ($<10^{-3}$ mW/mK) [28-30]. Moreover, none of these reports on thermoelectric Ti-doped ZnO explored atomic layer deposition.

In this work, the thermoelectric properties of ZnO thin films deposited by atomic layer deposition are tailored by incorporating HfO_2 and TiO_2 layers during deposition. The effect of dopant selection, whether Hf or Ti, in terms of thermal transport and stability of ALD ZnO is also discussed in detail. In addition, the amounts of dopant concentration were optimized to achieve the most desirable thermoelectric power factor.

2.2 Experimental Section

2.2.1 Thin Film Deposition and Sample Preparation

The sample preparation procedure is shown in Fig. 2.1. Atomic layer deposition of pure ZnO, Hf-ZnO (HZO) and Ti-ZnO (TZO) was performed on pre-cleaned glass and Si (100) substrates using BENEQ TFS-500 ALD reactor. Growth of ZnO was performed at 170ºC by sequential pulsing of diethylzinc (DEZn) and H_2O, while in the case of the HZO and TZO, the precursors used were tetrakis(dimethylamido)hafnium(IV) (TDMAHf) or $TiCl_4$ and H_2O. The TDMAHf solid source was heated to 50ºC prior to deposition. Nitrogen was used as the carrier gas, and the deposition pressure was 6.4 Pa. The precursor pulse times are as follows. For ZnO layers, the pulsing sequence used was DeZn (300 ms) - N_2 purge (1s) - H_2O (300 ms) - N_2 purge (1s). The HfO_2 pulsing sequence was TDMAHf (1000 ms) - N_2 purge (1 s) - H_2O (250 ms) – N_2 purge (1 s), while that of the TiO_2 layer was $TiCl_4$ (200 ms) – N_2 purge (1s) - H_2O (150 ms) – N_2 purge (1 s). Three ZnO-HfO_2/TiO_2 supercycles were deposited, wherein one supercycle contains about 0, 1, 2, 3 or 4% Hf or Ti relative to the intended thin film thickness as shown in Fig. 2.2. This nomenclature, which pertains to the nominal dopant amount in terms of number of cycles instead of the actual atomic composition, will be used to refer to the samples hereafter.

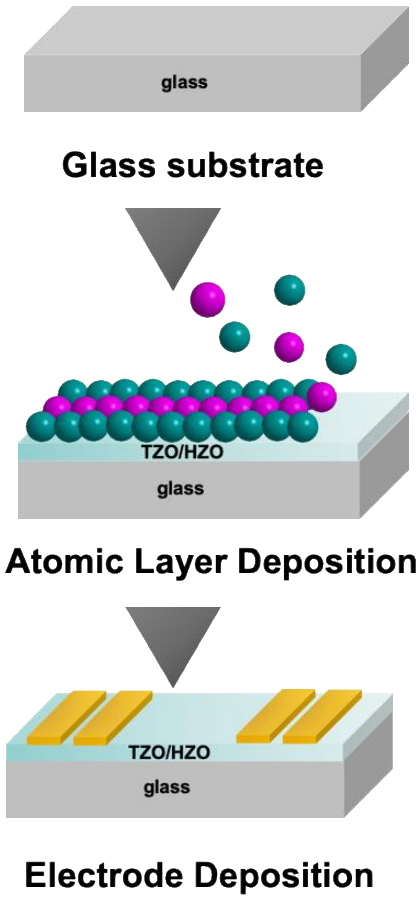

Fig. 2.1. Sample preparation procedure.

2.2.2 Thermal Transport Properties

The samples were diced into 2 cm × 0.4 cm rectangles. Electrode contacts (30-nm-thick Ti/ 40-nm-thick Au) were deposited using electron beam evaporation following the typical four-point probe configuration. Electrical conductivity and Seebeck coefficient measurements were performed for one cycle, from 300 to 450 K (heating stage) and back (cooling stage) using Linseis LSR-3 under He environment. Thermoelectric properties at low temperature were also obtained using a physical properties measurement system (PPMS, Quantum Evercool II) from 100–300 K under vacuum (~1Pa). Carrier concentration and hall mobility were measured at RT using Ecopia HMS-5300 Hall-effect measurement system following the van der Pauw technique [31].

2.2.3 Characterization

The structural properties of the pure and doped ZnO samples were characterized by asymmetric grazing incidence X-ray diffraction (GIXRD, 0.35 deg. omega angle of incidence) and symmetric X-ray diffraction as well as X-ray reflectivity (XRR) using a Rigaku SmartLab diffractometer equipped with a 9 kW rotating Cu anode (0.154 nm), HyPix-3000 single photon counting detector and Kα_1 monochromator. X-ray photoelectron spectroscopy (XPS, PHI5000 VersaProbeII, ULVAC-PHI) spectra were measured at RT with Al-Kα radiation (1486.6 eV) to analyze the chemical properties and bonding states of the thin films. The raw XPS data were analyzed using a commercial software (CasaXPS), wherein the O1s core levels were fitted using GL30 function (70% Gaussian, 30% Lorentzian) after Shirley background subtraction, and full width at half maximum (FWHM) value was 1.4 eV. All XPS spectra were calibrated with respect to the C1s peak (284.8 eV) to account for charging effects. Secondary ion mass spectroscopy (SIMS) analysis was also conducted to observe the Hf/Ti distribution within the ZnO. The cross-sectional thin film morphologies were then imaged using transmission electron microscopy (TEM, JEOL JEM-3100FEF at 300 kV), while top-view planar images were obtained using scanning electron microscopy (SEM, Hitachi SU6600) and atomic force microscopy (Shimadzu SPM-9600). The thin film thicknesses were measured via ellipsometry (Plasmos SD 2300).

2.3. Results and Discussion

2.3.1. Thin Film Properties

The ALD doping scheme of the thin film samples as shown in Fig. 2.2 was intentionally designed in a multilayer fashion. The HfO_2 and TiO_2 layers were inserted in between three layers of ZnO, such that about a total of 615 cycles of oxide material was achieved. Additional 5 cycles were deposited for each ZnO layer to promote ZnO renucleation, which may have been disrupted by the insertion of the HfO_2/TiO_2 layers. Ruoho et al. have previously confirmed that this stacking design is more effective in preserving the crystallinity and mobility of the pure ZnO, compared to a more distributed insertion of dopant layers [5].

The distribution of the Hf and Ti on the HZO and TZO films were investigated by measuring the SIMS depth profile, as shown in Fig. 2.3. The formation of both HfO_2 and TiO_2 layers sandwiched in between ZnO layers can be confirmed from the 180Hf + 16O and 48Ti peaks located at almost every third of the film thickness. The presence of alternately stacked multilayers is also supported by XRR presented in Fig. 2.4. Fitting parameters used in the XRR analysis are indicated in Table 2.1.

Thin film properties such as thickness and surface roughness of the samples containing different percentage of dopant concentrations are summarized in Table 2.2. The film thicknesses were measured by ellipsometry. Also indicated are the expected thickness of a single dopant layer, which was derived from the number of cycles and the total film thickness from ellipsometry. The actual thickness of each dopant layer is challenging to confirm using XRR due to high film roughness (~3–5 nm), as well as the fact that the growth rate per cycle (GPC) of pure TiO_2 and HfO_2 changes when co-deposited. The surface roughness of the thin films obtained from the AFM analysis are also presented. The doped samples revealed significantly lower surface roughness values compared to the pure ZnO thin film. The AFM

images for all samples are displayed in Fig. 2.5. This is advantageous since smoother surfaces are generally more favorable for better charge transport.

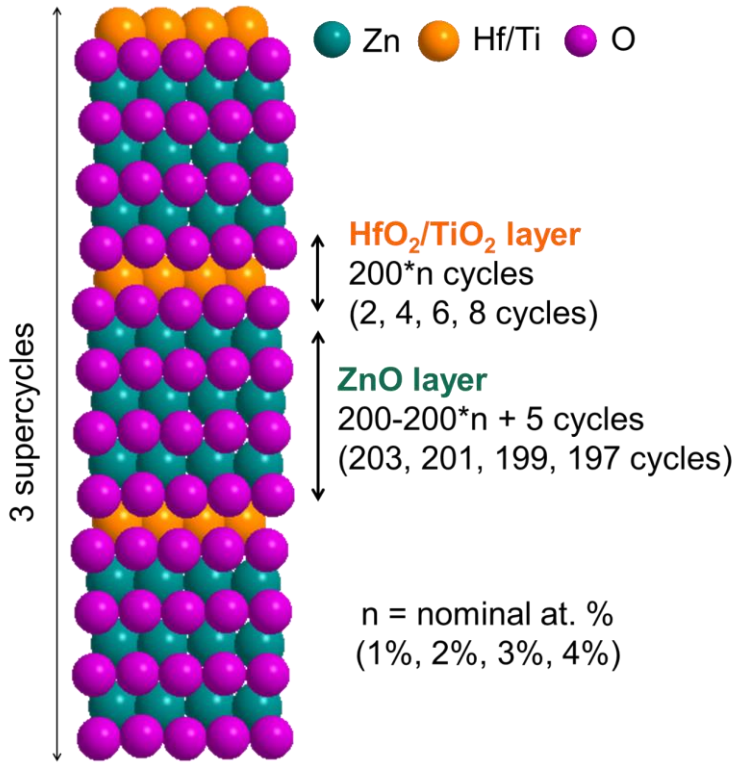

Fig. 2.2. Doping scheme indicating the position and thicknesses of the HfO_2/TiO_2 layers.

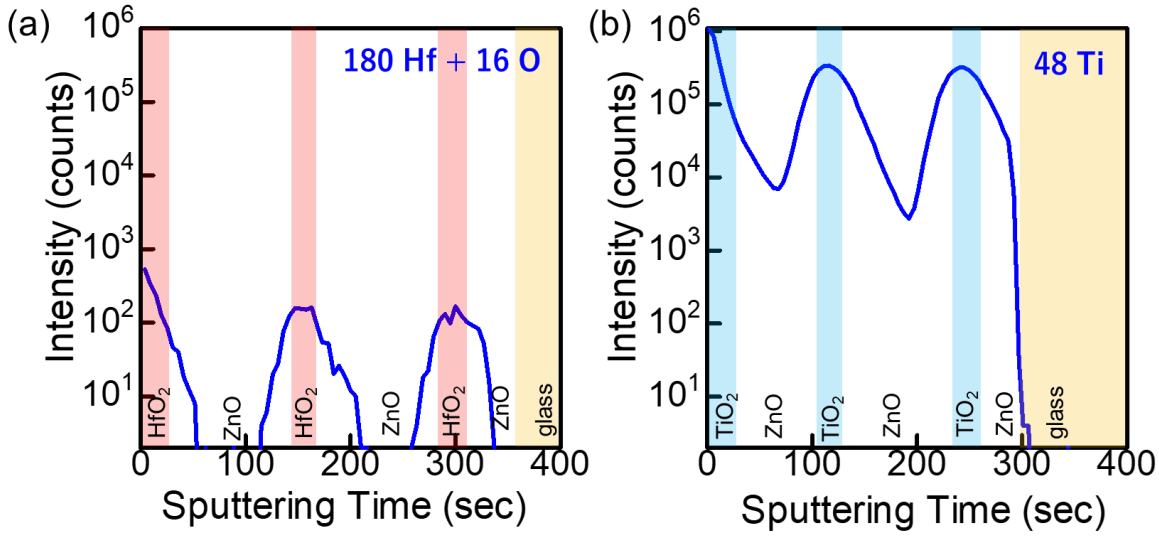

Fig. 2.3. SIMS profile of (a) 3%HZO samples ascribed to 180 Hf + 16 O, and (b) 3%TZO samples ascribed to 48 Ti.

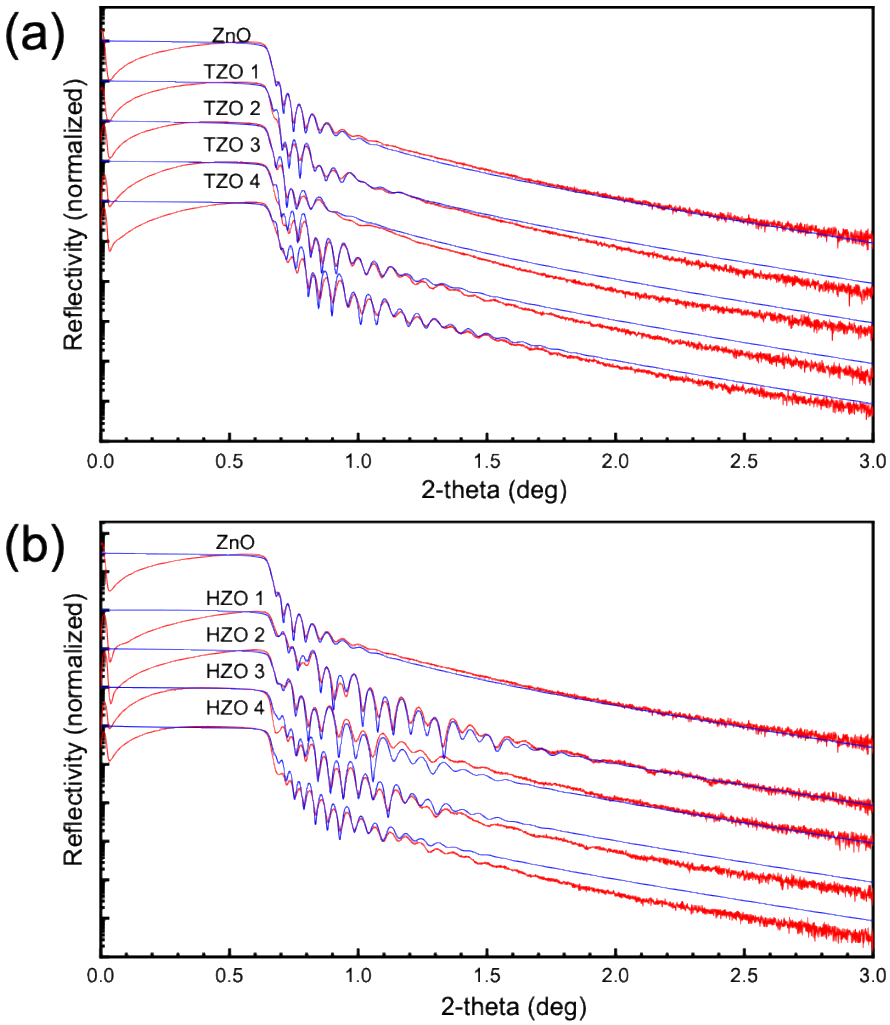

Fig. 2.4. XRR analysis showing experimental (red) and fitted (blue) spectra for all samples.

Table 2.1. Fitting parameters used in XRR analysis. Fixed parameters denoted by [--].

4% TZO				
No.	Layer name	Density(g/cm^3)	Roughness(nm)	# of periods
2	TiO_2	3.7[--]	4	3
1	ZnO	5.7[--]	4.5	3
0	SiO_2	2.05[--]	0.6[--]	--
3% TZO				
No.	Layer name	Density(g/cm^3)	Roughness(nm)	# of periods
2	TiO_2	3.7[--]	5	3
1	ZnO	5.7[--]	5	3
0	SiO_2	2.05[--]	0.6[--]	--
2% TZO				

No.	Layer name	Density(g/cm^3)	Roughness(nm)	# of periods
2	TiO_2	3.7[--]	3.5	3
1	ZnO	5.7[--]	4	3
0	SiO_2	2.05[--]	0.6[--]	--
1% TZO				
No.	Layer name	Density(g/cm^3)	Roughness(nm)	# of periods
2	TiO_2	3.7[--]	3	3
1	ZnO	5.7[--]	3.5	3
0	SiO_2	2.05[--]	0.6[--]	--
4% HZO				
No.	Layer name	Density(g/cm^3)	Roughness(nm)	# of periods
2	HfO_2	9.7[--]	2.5	3
1	ZnO	5.7[--]	3.5	3
0	SiO_2	2.05[--]	0.6[--]	--
3% HZO				
No.	Layer name	Density(g/cm^3)	Roughness(nm)	# of periods
2	HfO_2	9.7[--]	3	3
1	ZnO	5.7[--]	3.5	3
0	SiO_2	2.05[--]	0.6[--]	--
2% HZO				
No.	Layer name	Density(g/cm^3)	Roughness(nm)	# of periods
2	HfO_2	9.7[--]	3	3
1	ZnO	5.7[--]	3.5	3
0	SiO_2	2.05[--]	0.6[--]	--
1% HZO				
No.	Layer name	Density(g/cm^3)	Roughness(nm)	# of periods
2	HfO_2	9.7[--]	3.3	3
1	ZnO	5.7[--]	3.5	3
0	SiO_2	2.05[--]	0.6[--]	--
ZnO				
No.	Layer name	Density(g/cm^3)	Roughness(nm)	# of periods
1	ZnO	5.7[--]	4.5	--
0	SiO_2	2.05[--]	0.6[--]	--

Table 2.2. Thin film properties of all samples. Thickness (nm) was measured by ellipsometry, whereas root mean square surface roughness RMS (nm) is determined by AFM.

Sample	ZnO	HZO				TZO			
		1% Hf	2% Hf	3% Hf	4% Hf	1% Ti	2% Ti	3% Ti	4% Ti
Thickness	114.8 ± 0.1	121.1 ± 0.2	120.6 ± 0.5	118.3 ± 0.4	117.1 ± 0.6	116.6 ± 0.2	114.7 ± 0.3	111.6 ± 0.6	114.9 ± 0.2
Expected Single Dopant Layer Thickness	-	0.39	0.78	1.15	1.52	0.38	0.75	1.09	1.49
Ave. Rms	1.55	1.06	1.38	1.04	0.80	1.08	1.26	1.06	1.16
GPC (Å/cycle)	1.87	1.97	1.96	1.92	1.90	1.90	1.86	1.81	1.87

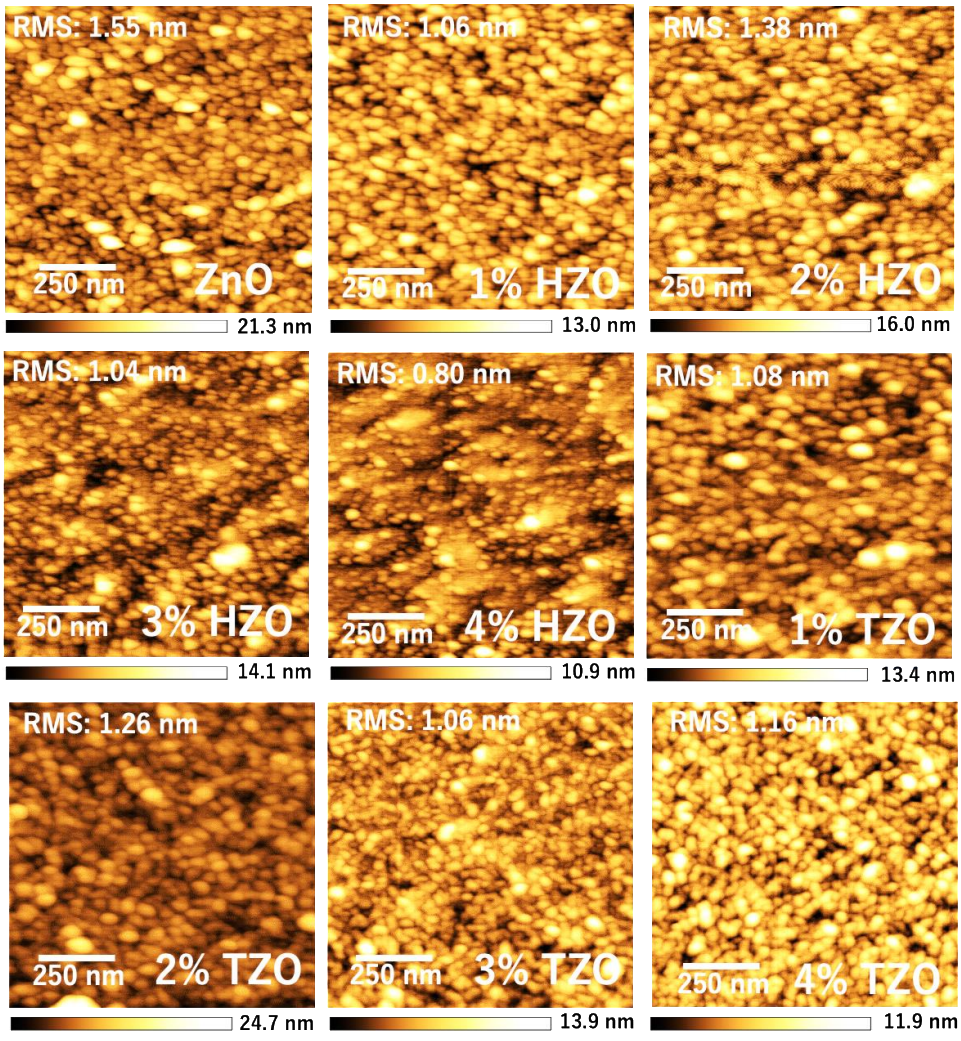

Fig. 2.5. AFM images of HZO and TZO samples with their corresponding RMS values.

Table 2.2 also shows the growth per cycle (GPC) trends of the samples with respect to the dopant concentration. The GPC values of the doped ZnO do not deviate largely from that of pure ZnO thin films. However, there is a general decreasing trend of the GPC relative to the doping amount in both HZO and TZO. This suggests that a thicker dopant layer causes a greater nucleation delay for a new ZnO layer. Moreover, it can be observed that HZO samples generally have higher GPC compared to TZO and ZnO. This can be due to the difference in the ligand exchange kinetics caused by the difference in the ligands present in the dopant precursors – chloride for TZO and dimethyl amine for HZO [32].

Fig. 2.6 present the cross-sectional high resolution TEM (HRTEM) images of the pure ZnO, 3%TZO and 3%HZO samples. A polycrystalline nature can clearly be observed from the HRTEM images and the corresponding nanobeam diffraction (NBD) images (inset). Distinct lattice fringes with thicknesses of 0.28 nm and 0.26 nm are also visible, which can be attributed to the interplanar distances between the (100) planes and the (002) planes of wurtzite ZnO, respectively. The NBD image of the ZnO sample as shown in Fig. 2.6a reveals bright spots corresponding to both (002) and (100). For the TZO sample, the dominance of the bright ring ascribed to (100) can be noted, while that of (002) is more pronounced for the HZO sample. The surface morphologies of the thin films were also examined using SEM. The pure ZnO sample in Fig. 2.6d showed granular structures, which became finer and more elongated in the case of TZO (Fig. 2.6e). Even finer grains were revealed in the case of the HZO sample, as shown in Fig. 2.6f. These morphological evolutions could be attributed to the presence of the dopant layers. The more pronounced contrast along the grain boundaries for the TZO sample in Fig. 2.6e likely physically represents the co-existence of TiO_2 and ZnO in the thin film. On the other hand, the HZO sample revealed even finer grains, which could indicate a shift in grain orientation. This would more clearly be understood in the XRD analysis.

The structural properties of the thin films were evaluated using asymmetric GIXRD

and symmetric XRD. Crystalline phases were identified using asymmetric surface sensitive GIXRD scans as shown in Fig. 2.7. The grown films revealed a polycrystalline nature with a ZnO hexagonal wurtzite structure, which corroborated with the TEM-NBD analysis. All visible peaks can be attributed to the standard diffraction pattern of wurtzite ZnO (JCPDS 043-002), which suggests that only minimal Hf or Ti oxide formation occurred compared to ZnO. The peaks correspond to the (100), (002), (101), (102), (110), (103), and (112) planes of wurtzite ZnO. For the TZO samples, all films revealed a dominant (100) orientation, as also seen in symmetric theta/2theta scans (Fig. 2.8), which is sensitive to planes parallel to substrate. The dominance of the (100) plane is expected for the current deposition temperature of 170°C, as similarly observed in a previous literature [33]. No further peak changes can be observed by varying the percentage of Ti dopant concentration. On the other hand, Hf doping showed a more complex effect on the ZnO lattice. At 1% doping, (002) orientation is slightly degraded but otherwise comparable crystallinity is observed compared to pure ZnO. Similarly, in symmetric scans (Fig. 2.8), this 1% Hf doping increases the (100) orientation parallel to surface. However, when 2% and more dopants are introduced, the dominance of the (100) is suppressed, preferring the (002) orientation instead. Overall preferred orientation is decreased resulting in comparable intensities of (100), (002) and (101). This is expected since doping often disrupts ZnO crystallinity. Further increasing to 3% led to shifting the dominance to the (002) peak, which corresponds to the ZnO c-axis orientation. The c-axis orientation was sustained even when a 4% doping amount was reached. The preferential (100) orientation is typical for pure ZnO deposited by ALD likely owing to the charge neutrality of the (100) plane, as opposed to the positively-charged polar (002) planes which attract broken ethyl group fragments [26]. The shift in orientation from (100) to (002) in the presence of a minimum of 3% Hf possibly arises from the disturbance of the (100) charge neutrality by the Hf^{4+} ions. This leads to favoring the growth orientation towards the plane of least surface energy, which is the

(002) plane [26]. This phenomenon could not be observed with TZO possibly since Ti^{4+} ions are significantly smaller than Hf^{4+}, so they could not have been affecting the growth orientation as much.

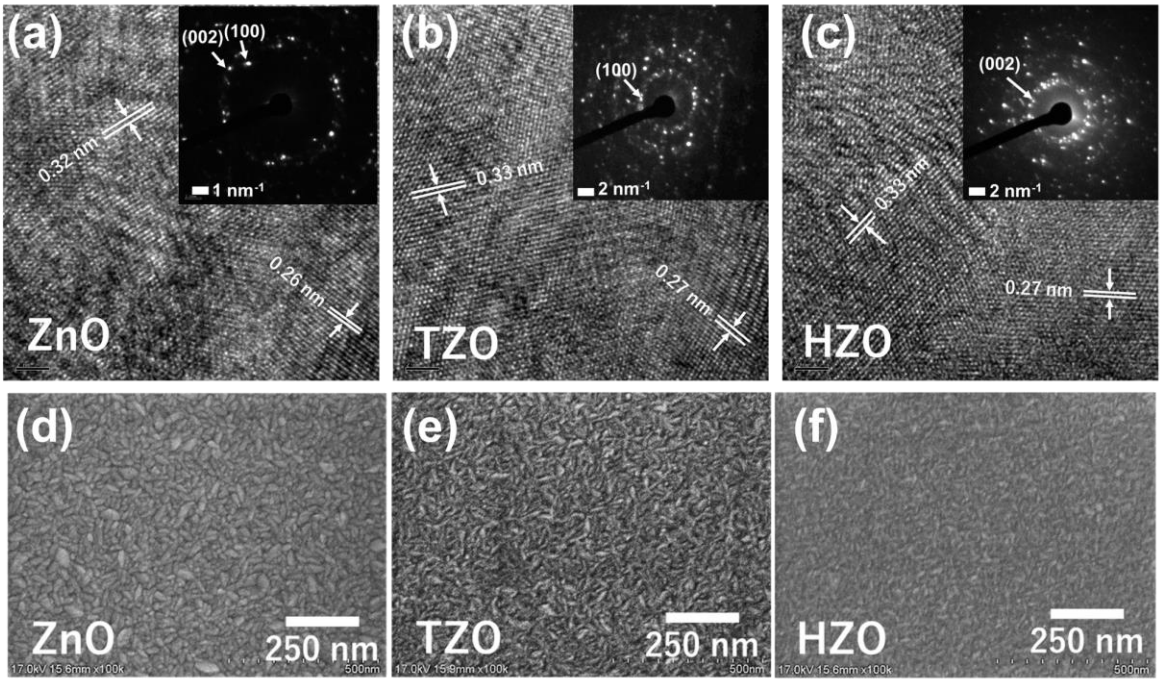

Fig. 2.6. Cross-sectional TEM image of (a) ZnO, (b) 3% TZO and (c) 3% HZO samples and their corresponding nanobeam diffraction patterns (inset), top-view SEM images of (d) ZnO, (e) 3% TZO and (f) 3% HZO samples.

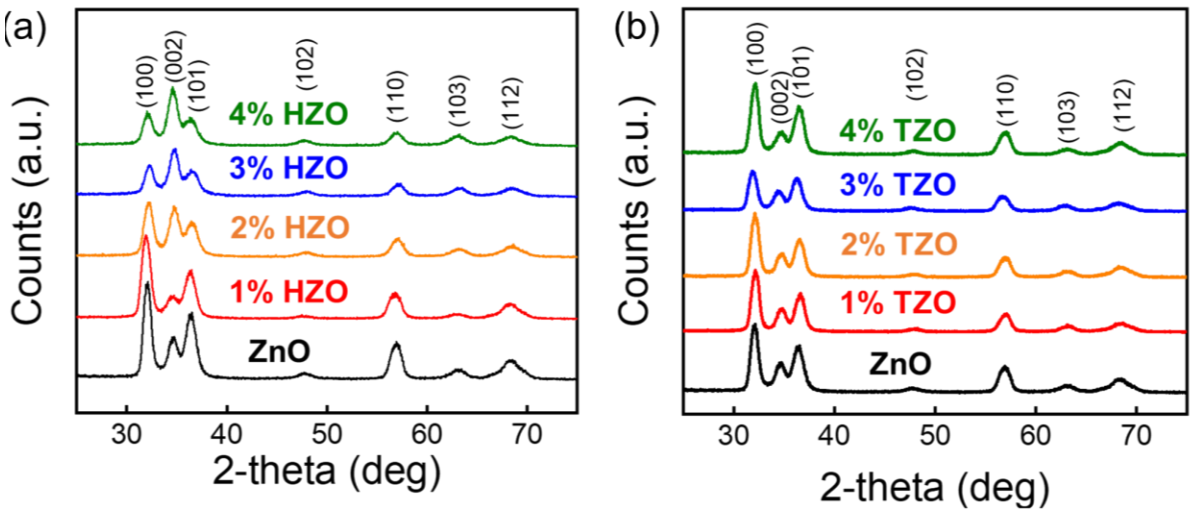

Fig. 2.7. XRD spectra of (a) HZO samples and (b) TZO samples of varying the percentage of dopant concentrations.

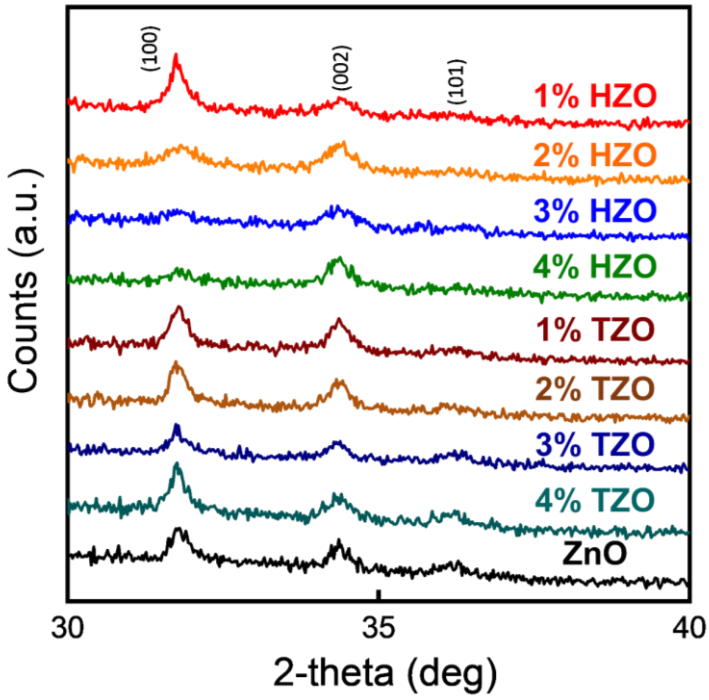

Fig. 2.8. Symmetric theta/2theta XRD patterns for all samples.

2.3.2 Effect of Doping Element on TE Properties

The effect of doping element on the thermoelectric properties (σ, S and PF) was investigated within the range of 300 and 450 K and presented in Fig. 2.9. The properties are shown for one thermal cycle, comprising a heating stage (300 K to 450 K) and a cooling stage (450 K to 300 K). The doping level for both TZO and HZO used in the measurement were both 3%. For both electrical conductivity and Seebeck coefficient, all samples exhibited instability between the heating and the cooling stage properties. This phenomenon has also been previously observed in ALD ZnO [8]. It was said that ZnO thin films typically need to undergo a first thermal cycle in order to stabilize. Heat exposure likely causes instability in the ZnO via formation of acceptor defects, leading to significantly degraded thermoelectric properties after an initial heating measurement run [8]. Fig. 2.9a reveals the largest deviation in electrical conductivity for TZO, while the one that exhibited the least instability is HZO. Despite this, the TZO still emerged as the most conductive throughout the temperature range during cooling, followed by the HZO. Pure ZnO evidently suffered from a severe degradation in σ. The instability in Seebeck coefficient was similarly largest with ZnO, while both TZO and HZO exhibited only modest changes. In effect, ZnO displayed the largest decrease in power factor. The PF of the TZO sample showed a small instability, which can mostly be attributed to the large decrease in electrical conductivity. However, almost no instability in PF is observed for HZO, implying that the small deviations in both electrical conductivity and Seebeck coefficient likely compensate each other. Nevertheless, both doped samples outperformed the pure ZnO thin film for all temperatures during the cooling stage. Highest PF values were consistently exhibited by HZO throughout the temperature range, with a maximum PF of 0.143 mW/mK^2 at about 450 K. The highest PF values achieved for TZO and ZnO are 0.123 mW/mK^2 and 0.104 mW/mK^2, respectively, also at 450 K.

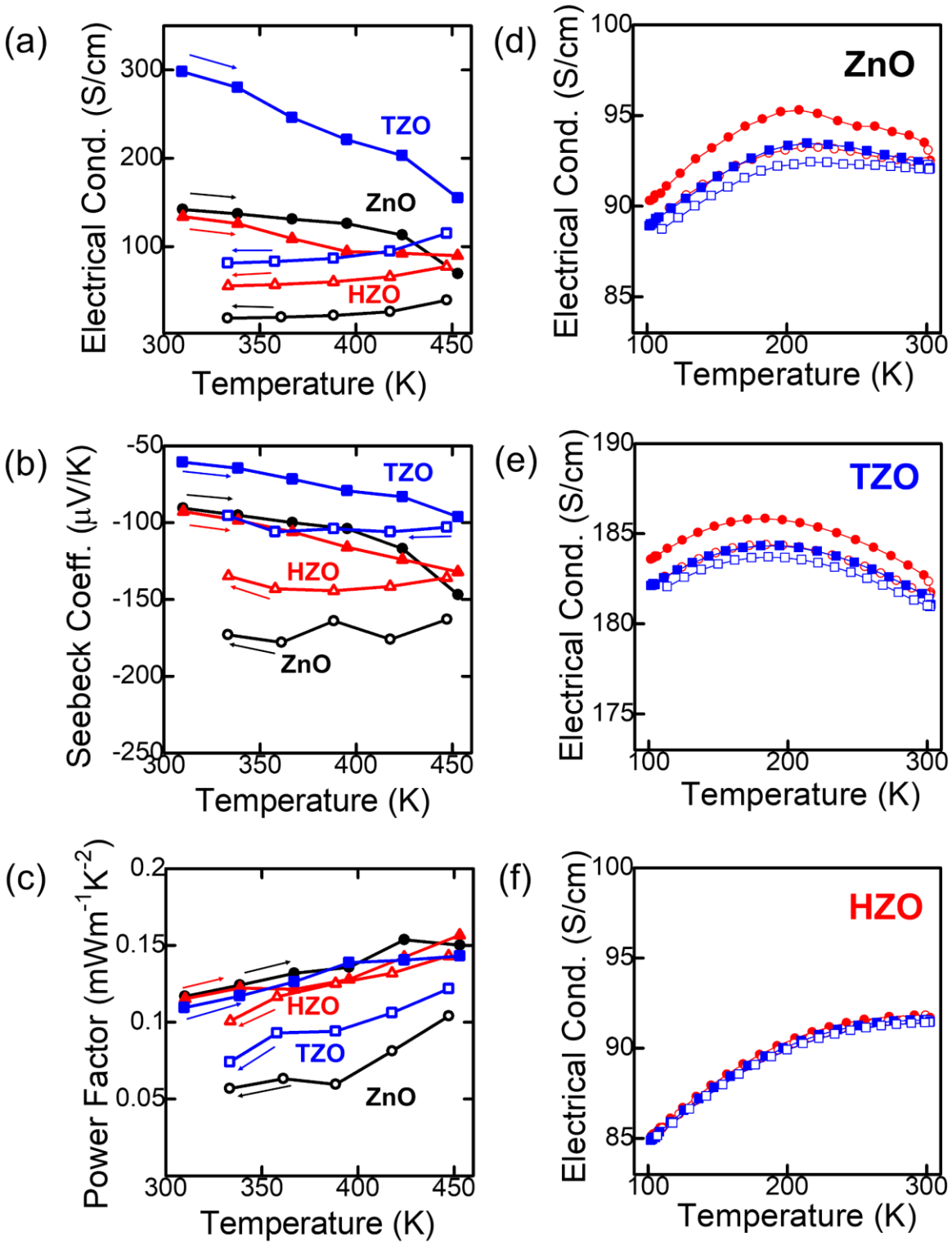

Fig. 2.9. High *T* thermoelectric properties showing (a) electrical conductivity, (b) Seebeck coefficient, and (c) power factor for HZO, TZO and ZnO from 300 to 450 K, and Low *T* cyclic electrical conductivity measurements for (d) ZnO, (e) TZO and (f) HZO from 100 to 300 K.

In order to further understand the nature and extent of the instability, low temperature cyclic thermoelectric performance was evaluated from 100 to 300 K. This was conducted to isolate the effect of heat on the instability. It can be observed from the plot of electrical conductivities in Fig. 2.10a that even at very low temperature conditions, instability is still imminent in the pure ZnO sample. In the case of TZO, this instability is somehow reduced especially during the second thermal cycle. However, in the presence of Hf, the instability is completely eliminated. Although this has rarely been observed in relation to thermoelectricity, Hf has been previously reported to improve electrical stability of ZnO. According to previous literature, this high electrical stability was attributed to the suppression of oxygen-related defects caused by Hf [25-27]. Oxygen-bond breaking can lead to the formation of interstitial oxygen, an acceptor defect that likely reduces free electron concentration. However, the reason behind the defect suppression has not been sufficiently elaborated in these reports. This can likely be explained by the significantly stronger chemical bonding of Hf–O compared to Zn–O. Table 2.3 summarizes the bond dissociation energies and electronegativity differences of the bonds under study. The electronegativity difference between Hf and O is significantly higher in comparison to both Ti–O and Zn–O, which probably results in stronger Hf–O bonds. In addition, the bond dissociation energy of Zn–O is only about a fourth that of Hf–O, and about a third that of Ti–O. This implies that once the Hf or Ti substitutes onto Zn vacancy sites to bond with oxygen during deposition, they would require high energy to break. Zn vacancies are regarded as acceptor defects as well, so Hf/Ti substitution can also likely improve free electron concentration. However, the high bond dissociation energy can also suggest that Hf–O bonds are more difficult to form and are likely of lower concentration compared to Ti–O. In any case, the layer-by-layer self-limiting growth by ALD could likely have helped in forming Hf–O bonds even at a relatively low temperature (170°C) compared to other techniques [34-35]. The cyclic measurements for Seebeck coefficients at low temperature, on the other hand,

remained constant for all samples throughout the temperature range, as shown in Fig. 2.11.

Table 2.3. Bond dissociation energies and ionic radii of Zn, Hf and Ti with O [24].

	Bond Dissociation Energy (kJ/mol)		Ionic Radius (pm)
Zn–O	<250.0	Zn	74
Hf–O	801.0	Hf	72
Ti–O	666.5	Ti	56

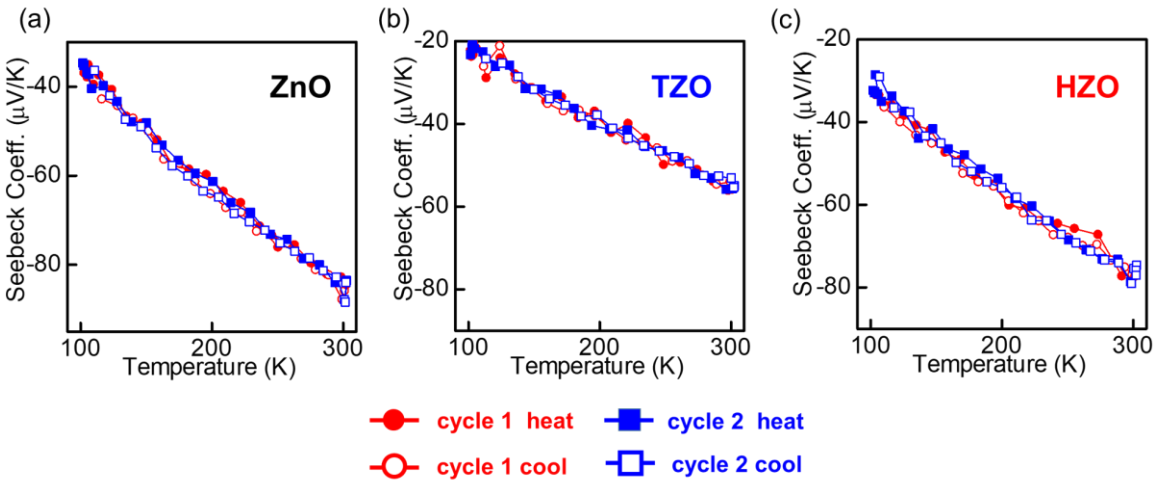

Fig. 2.11. Cyclic Seebeck coefficient values for (a) ZnO, (b) 3%TZO and (c) 3%HZO.

To experimentally confirm the relationship between oxygen-related deficiencies and thermoelectric stability, high resolution surface XPS spectra were obtained before and after the high temperature TE properties measurement. The spectra were calibrated with respect to the C1s peak (284.8 eV), representing adventitious carbon. These spectra likely represent both HfO_2/TiO_2 and ZnO layers. XPS surface sensitivity is about a few nanometers (~ 2 nm), while the thickness of the HfO_2 and TiO_2 layers are expected to be about 1.1 nm from the surface, assuming totally no interlayer mixing occurred. Presented in Fig. 2.12 are the XPS O1s core

level peaks of the samples, deconvoluted into three components: $M–O_I$, $M–O_{II}$ and $M–O_{III}$, centered at 529.9 ± 0.1 eV, 531.2 ± 0.1 eV and 532.0 ± 0.1 eV, respectively. The $M–O_I$ peak corresponds to the metal-oxygen lattice bond, which means the O^{2-} ions are attached to three metal atoms. The $M–O_{II}$ peak represents the O^{2-} ions in the oxygen-deficient regions, which can be related to oxygen vacancies. Finally, the surface adsorbed oxygen such as hydroxyl (–OH) and carbonyl (–COOH) are characterized by the $M–O_{III}$ peak [8, 36-38]. Prior to the thermal cycle, ZnO showed the highest $M–O_I$ among the samples (Fig 2.12a), which is expected as Zn–O bonding requires the least amount of energy to form compared to Ti–O and Hf–O [36]. In effect, ZnO displayed the lowest $M–O_{II}$ peak percentage. The high probability to form Zn–O bonds due to low bond formation energy likely leads to fewer oxygen-deficient defects. In the case of TZO and HZO, stronger $M–O_{II}$ peaks are observed. Extrinsic Ti^{4+} and Hf^{4+} ions from the precursors tend to attract oxygen from the ZnO matrix during the free competitive growth of Ti–O/Hf–O and Zn–O, and simultaneously form oxygen vacancies during the process [17, 39]. After the thermal cycle, significant changes in the $M–O_{II}$ peaks can be observed. For the pure ZnO thin film in Fig. 2.12d, the amount of $M–O_{II}$ spiked from 4.7% to 26.0%, which is expected as heating may easily cause Zn–O bond-breaking. Oxygen atoms tend to be diffused out in the low pressure, oxygen-deficient He environment during the thermal cycle [40]. TZO, on the other hand, showed only a slight increase in $M–O_{II}$, from 15.1% to 20.9%. With this, it could be said that the strength of Ti-O bonds could somehow be slightly suppressing the formation of oxygen vacancies. This could arise from the almost twice the bond dissociation energy of Ti–O compared to Zn–O. However, when Hf is added, the amount of $M–O_{II}$ decreased slightly. While a huge amount of bond-breaking could have occurred in pure ZnO during the thermal cycle, HZO seemed to have withstood this, similarly owing to the high bond dissociation energy of Hf–O. This supports the previous hypothesis

that the oxygen-related defects are being suppressed when ZnO is doped with Hf. Thus, HZO appears to be more electrically stable than both TZO and pure ZnO.

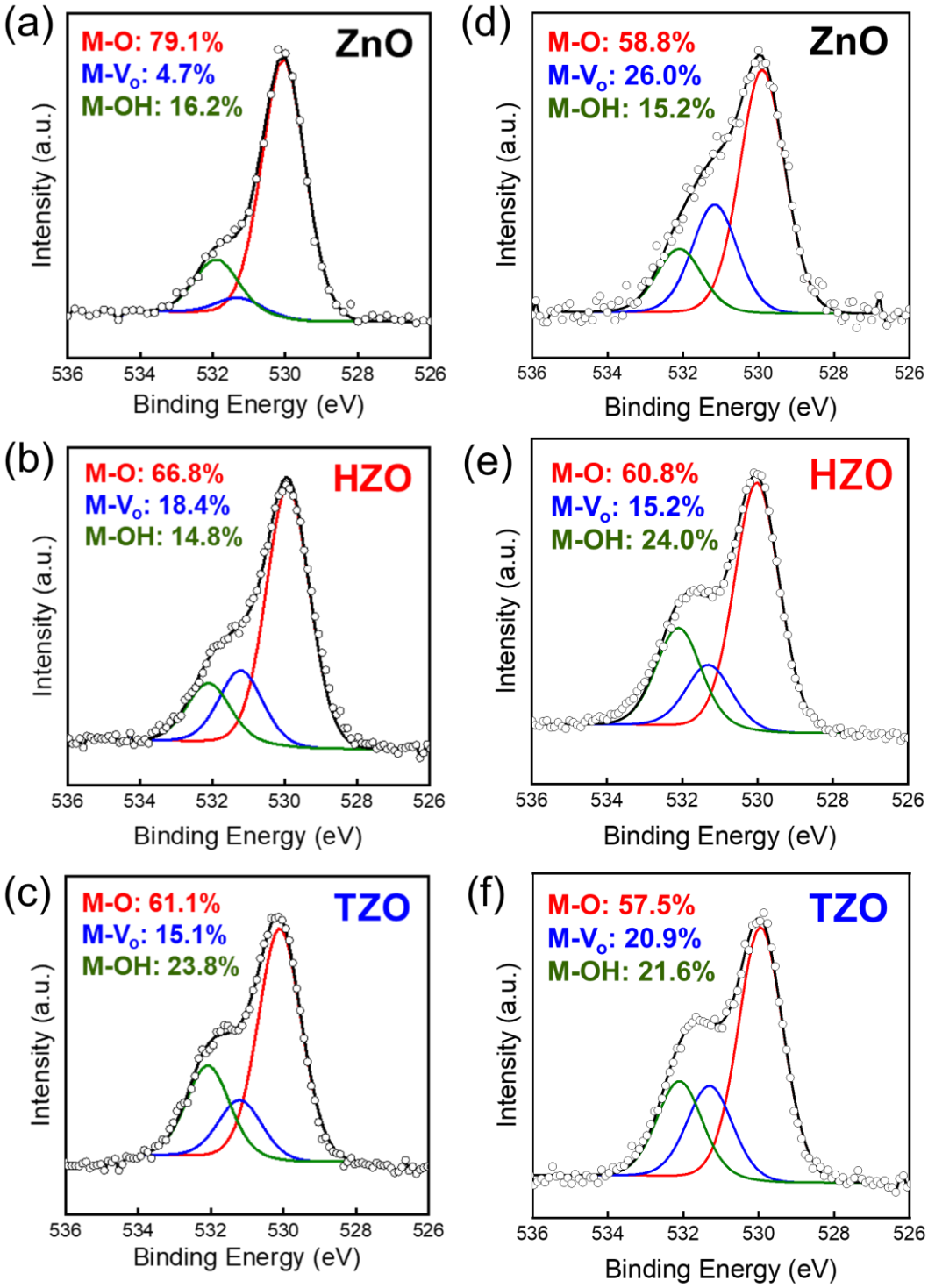

Fig. 2.12. XPS O1s deconvoluted peaks before the thermal cycle for (a) ZnO, (b) HZO and (c) TZO, and after the thermal cycle for (d) ZnO, (e) TZO (3%) and (f) HZO (3%).

2.3.3 Effect of Nominal Percentage of Dopant Concentration

To confirm the effect of dopant concentration on the charge transport properties, Hall effect measurements were performed at room temperature on the as-deposited samples prior to applying any heat cycle. Shown in Fig. 2.13 are the plots of carrier concentration and Hall mobility (μ) vs. dopant concentration. The carrier concentration (n) initially gave negative values, which indicate typical n-type semiconductor behavior, but are presented here in absolute value for simplicity. Doping with Ti resulted in a significantly higher carrier concentration compared to the pure ZnO thin film, leading to high electrical conductivity even at 1% doping concentration. On the other hand, the addition of Hf did not appear to result in successful doping. Minimal changes in both n and μ were observed regardless of the doping concentration. As the carrier concentration could also be affected by intrinsic defects such as oxygen vacancies, the lower carrier concentration of the HZO samples supports the XPS analysis wherein it was demonstrated that the incorporation of Hf suppresses the formation of such vacancies.

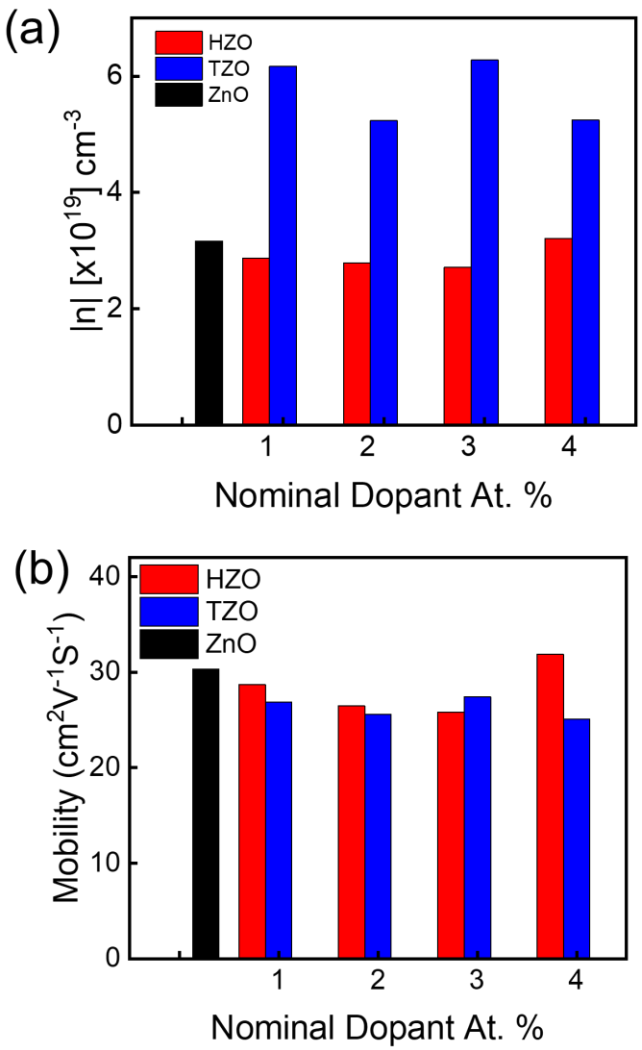

Fig. 2.13. Hall effect showing (a) carrier concentration and (b) mobility of all samples.

As discussed earlier, the cooling stage values represent more reliably the TE properties of the samples. Because of this, the effect of the amount of dopants in the cooling stage thermoelectric properties (from 450 K to 330 K) is examined and the plots are displayed in Fig. 2.14. Among the TZO samples, 1% TZO exhibits the highest electrical conductivity, and there is a decreasing trend for electrical conductivity with amount of Ti. This is in contrast with the Hall measurements, which were taken before any thermal cycle, where the 3% TZO exhibited the highest mobility and carrier concentration. This means that excess Ti^{4+} could have reduced

the electrical conductivity upon stabilizing after a thermal cycle. Nevertheless, even only a small amount of Ti could lead to an almost five-fold increase in electrical conductivity. On the other hand, the Seebeck coefficients of TZO were evidently lower than pure ZnO and display only small changes with dopant % concentration. This implies that the Ti is more likely to cause minor structural changes to ZnO, as seen by the direct effect on the electrical conductivity but minimal influence on Seebeck coefficient. Highest PF, therefore, was observed for 1% TZO with a value of 0.136 mW/mK^2. Adding Hf, on the other hand, results in a slightly different behavior. Improvement in electrical conductivity was observed only from 3% Hf, which incidentally is where the change in thin film crystal orientation was observed to occur, as revealed by the XRD analysis. This suggests that c-axis i.e. (002) aligned HZO leads to improved electrical conductivity, probably owing to the shorter electron path length along the c-plane, as well as diminished grain boundary scattering between grains similarly aligned along the c-axis, as previously reported for c-axis aligned ZnO thin films [38, 40-43]. Also, this could have arisen from free electron generation caused by substitution of Hf^{4+} onto Zn^{2+} sites. The value for 2% Hf was not included as the resistivity was higher than the equipment limit probably due to misfabrication. Seebeck coefficients, on the other hand, were slightly smaller for HZO compared to ZnO throughout the temperature range, but were not as low as those of TZO. Unlike in TZO, the non-drastic electrical conductivity improvement for HZO naturally led to minimal decrease in Seebeck coefficient. The combination of a relatively high Seebeck coefficient and decent electrical conductivity led to an almost two-fold improvement in PF for 3% and 4% HZO compared to ZnO. The highest PF was obtained at 450 K for 3 % HZO at 0.157 mW/mK^2. Nonetheless, incorporation of Ti or Hf dopants both enhanced the thermoelectric PF of ZnO during the cooling stage. In the case of TZO, even only 1% doping can significantly enhance the *PF* of ZnO, while 3% HZO resulted to highest *PF* for all doped samples.

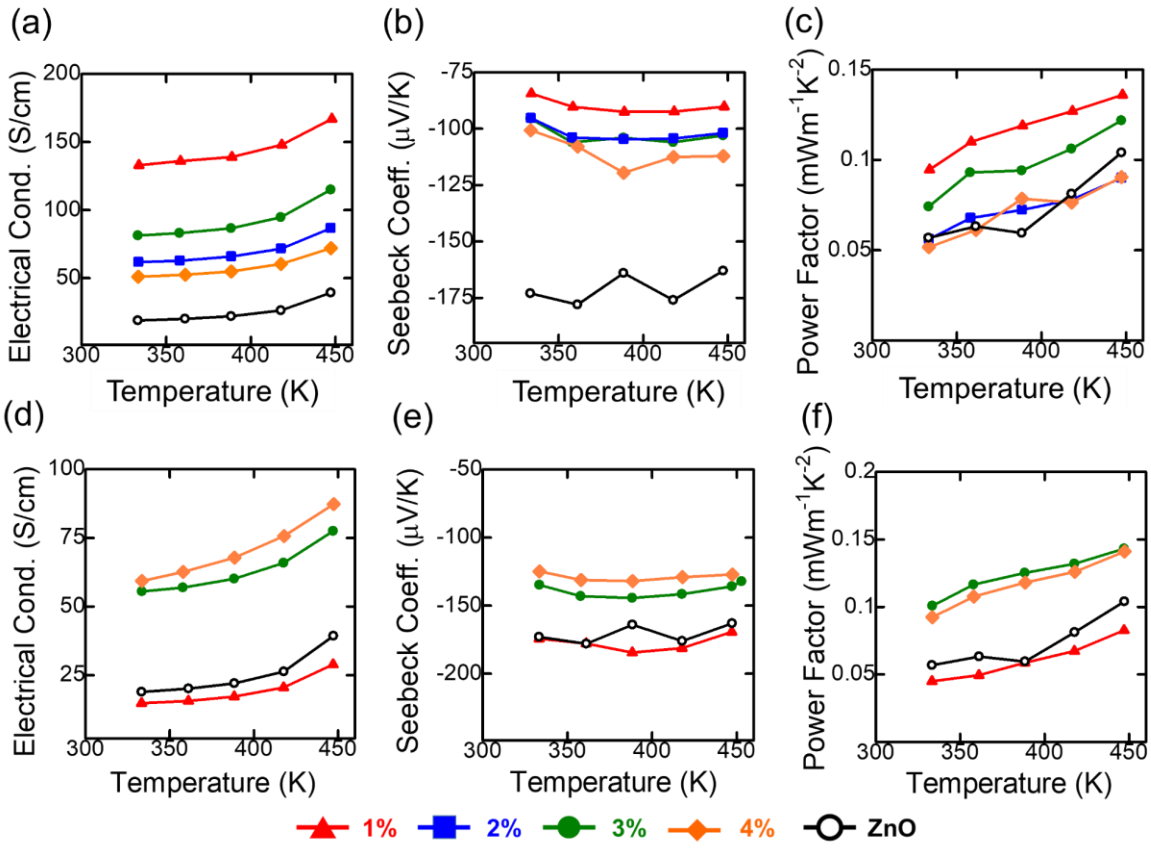

Fig. 2.14. High T thermoelectric properties at cooling stage showing (a) electrical conductivity, (b) Seebeck coefficient, and (c) power factor for TZO, and (d) electrical conductivity, (e) Seebeck coefficient and (f) power factor for HZO, from 450 to 300 K.

2.4. Summary

HfO_2 and TiO_2 layers were infused into ALD ZnO thin films to enhance their thermoelectric performance. Sandwiching TiO_2 layers in between ZnO layers during ALD doubles the carrier concentration compared to pure ZnO, leading to an enhanced thermoelectric power factor. Meanwhile, incorporating HfO_2 to form HZO thin films led to a significant improvement in thermal stability owing to the film orientation shifting and strong Hf-O bonding. The Seebeck coefficients of HZO samples were also almost retained to similar values with ZnO, which led to achieving the highest thermoelectric power factor among all samples. Optimizing the nominal percentage of dopant concentration for all samples resulted in obtaining the highest power factor at 1% for TZO and 3% for HZO, with values of 0.136 mW/mK^2 and 0.143 mW/mK^2, respectively.

Overall, both Hf and Ti exhibited their individual merits as dopants for ALD ZnO thermoelectric thin films. It is therefore possible that both stability and improved thermoelectric power factor can be achieved when Hf and Ti are co-doped in ZnO. In addition, since Hf is a relatively rare element, using this in conjunction with a high doping efficiency element such as Ti may lead to cheaper, high performance thermoelectric devices.

References

1) Zhou, Z.; Ren, G.K.; Tan, X.; Liu, R.; Liu, C.; Lin, Y.H.; Nan, C.W. Enhancing the Thermoelectric Performance of ZnO Epitaxial Films by Ga Doping and Thermal Tuning J. Mater. Chem. A 2018, 6, 24128-24135.

2) Jood, P.; Mehta, R.J.; Zhang, Y.; Peleckis, G.; Wang, X.; Siegel, R.W.; Borca-Tasciuc, T.; Dou, S.X.; Ramanath, G. Al-doped Zinc Oxide Nanocomposites with Enhanced Thermoelectric Properties Nano Lett. 2011, 11, 4337-4342.

3) Fujimoto, Y.; Uenuma, M.; Ishikawa, Y.; Uraoka, Y. Analysis of Thermoelectric Properties of Amorphous InGaZnO Thin Film by Controlling Carrier Concentration AIP Advances 2015, 5, 097209.

4) Umeda, K.; Uenuma, M.; Senaha, D.; Felizco, J.C.; Uraoka, Y.; Adachi, H. Amorphous Thin Film for Thermoelectric Application IOP Conf. Series: Journal of Physics: Conf. Series 2018, 1052, 012016.

5) Ruoho, M.; Pale, V.; Erdmanis, M.; Tittonen, I. Influence of Aluminium Doping on Thermoelectric Performance of Atomic Layer Deposited ZnO Thin Films Appl. Phys. Lett. 2013, 103, 203903.

6) Ruoho, M.; Juntunen, T.; Tittonen, I. Large-area Thermoelectric High-Aspect-Ratio Nanostructures by Atomic Layer Deposition Nanotechnology 2016, 27, 355403.

7) Ruoho, M.; Juntunen, T.; Alasaarela, T.; Pudas, M.; Tittonen, I. Transparent, Flexible, and Passive Thermal Touch Panel Adv. Mater. Technol. 2016, 1, 1600204.

8) Kim, H.; Wang, Z.; Hedhili, M.N.; Wehbe, N.; Alshareef, H.N. Oxidant-Dependent Thermoelectric Properties of Undoped ZnO Films by Atomic Layer Deposition Chem. Mater. 2017, 29, 2794−2802.

9) Lee, S.; Lee, J.; Choi, S.; Park, J. Studies of Thermoelectric Transport Properties of Atomic Layer Deposited Gallium-doped ZnO Ceramics International 2017, 43, 7784-7788.

10) Tynell, T.; Terasaki, I.; Yamauchi, H.; Karppinen, M. Thermoelectric Characteristics of (Zn,Al)O/hydroquinone Superlattices J. Mater. Chem. A 2013, 1, 13619.

11) Lee, D.; Kim, H.; Kwon, J.; Choi, H.; Kim, S.; Kim, K. Structural and Electrical Properties of Atomic Layer Deposited Al-Doped ZnO Films Adv. Funct. Mater. 2011, 21, 448-455.

12) Zhu, S.; Geng, Y.; Lu, H.; Zhang, Y.; Sun, Q.; Ding, S.; Zhang, D. W. Effects of Rapid Thermal Annealing on Hf-doped ZnO Films Grown by Atomic Layer Deposition J. Alloys Compd 2013 577, 340-344.

13) Barasheed, A.Z.; Kumara, S. R. S.; Alshareef, H. N. Temperature Dependent Thermoelectric Properties of Chemically Derived Gallium Zinc Oxide Thin Films J. Mater. Chem. C 2013, 1, 4122-4127.

14) Kang, Y.H.; Jang, K.; Lee, C.; Cho, S. Y. Facile Preparation of Highly Conductive Metal Oxides by Self-Combustion for Solution-Processed Thermoelectric Generators ACS Appl. Mater. Interfaces 2016, 8, 5216−5223.

15) Fan, P.; Li, Y.; Zheng, Z.; Lin, Q.; Luo, J.; Liang, G.; Zhang, M.; Chen, M. Thermoelectric Properties Optimization of Al-doped ZnO Thin Films Prepared by Reactive Sputtering Zn–Al Alloy Target Appl. Surf. Sci. 2013, 284, 145–149.

16) Saini, S., Mele, P.; Honda, H.; Matsumoto, K.; Miyazaki, K.; Molina Luna, L.; Hopkins, P. E. Influence of Postdeposition Cooling Atmosphere on Thermoelectric Properties of 2% Al-Doped ZnO Thin Films Grown by Pulsed Laser Deposition J. Electron. Mater. 2015, 44, 6, 1547-1553.

17) Lee, D.; Kim, K.; Kim, S.; Kwon, J.; Xu, J.; Kim, K. Atomic Layer Deposition of Ti-

doped ZnO Films with Enhanced Electron Mobility J. Mater. Chem. C 2013, 1, 4761-4769.

18) Minami, T.; Nanto, H.; Takata, S. Highly Conductive and Transparent Aluminum Doped Zinc Oxide Thin Films Prepared by RF Magnetron Sputtering Jap. J. Appl. Phys. 1984, 23, 5A, L280.

19) Singh, A.; Mehra, R.; Buthrath, N.; Wakahara, A.; Yoshida, A. Highly Conductive and Transparent Aluminum-doped Zinc Oxide Thin Films Prepared by Pulsed Laser Deposition in Oxygen Ambient Journal of Applied Physics 2001, 90, 11, 5661-5665.

20) Lee, W.; Park, N.; Kang, S.; Kim, G.; Koh, J.; Saitoh, E.; Lee, S.; Enhanced Cross-Plane Thermoelectric Figure of Merit Observed in an Al2O3/ZnO Superlattice Film by Hole Carrier Blocking and Phonon Scattering J. Phys. Chem. C 2019, 123, 23, 14187–14194.

21) Park, N.; Lee, W.; Yoon, Y.; Ahn, J.; Lee, J.; Kim, G.; Kim, T.; Choi, C.; Park, J.; Saitoh, E.; Lee, S. Direct Probing of Cross-Plane Thermal Properties of Atomic Layer Deposition Al2O3/ZnO Superlattice Films with an Improved Figure of Merit and Their Cross-Plane Thermoelectric Generating Performance ACS Appl. Mater. Interfaces 2018, 10, 44472−44482.

22) Tappuraa, K.; Juntunen, T.; Jaakkola, K.; Ruoho, M.; Tittonen, I.; Ritasalo, R.; Pudas, M. Large-area Implementation and Critical Evaluation of the Material and Fabrication Aspects of a Thin-film Thermoelectric Generator based on Aluminum-doped Zinc Oxide Renew. Energy 2020, 147, 1292-1298.

23) Sato, H.; Minami, T.; Takata, S.. Highly Transparent and Conductive Group IV Impurity-Doped ZnO Thin Films Prepared by Radio Frequency Magnetron Sputtering J. Vac. Sci. & Technol. A: Vacuum, Surfaces, and Films 11 1993, 6, 2975-2979.

24) Luo, Y.R. Bond Dissociation Energies. In CRC Handbook of Chemistry and Physics, 89th ed.; Lide, D. R., Ed.; CRC Press/Taylor and Francis: Boca Raton, FL, 2009.

25) Ahn, C.H.; Kim, J. H.; Cho, H. K. Tunable Electrical and Optical Properties in Composition Controlled Hf:ZnO Thin Films Grown by Atomic Layer Deposition J. Electrochem. Soc. 2012, 159, 4, H384-H387.

26) Geng, Y.; Xie, Z.; Yang, W.; Xu, S.; Sun, Q.; Ding, S.; Lu, H.; Zhang, D. W. Structural, Optical, and Electrical Properties of Hf-doped ZnO Films Deposited by Atomic Layer Deposition Surf. Coat. Tech. 2013, 232, 41-45.

27) Ding, X.; Qin, C.; Song, J.; Zhang, J.; Jiang, X.; Zhang, Z. The Influence of Hafnium Doping on Density of States in Zinc Oxide Thin-Film Transistors Deposited via Atomic Layer Deposition Nanoscale Res. Lett. 2017, 12, 63.

28) Hong, M.H.; Choi, H.; Kim, Y.; Kim, T.; Cho, H.; Driss, Z.; Driss, D.; Bouabidi, A.; Euchy, S.; Park, H. Ti Doping Effects on the Seebeck Coefficient and Electrical Conductivity of Mesoporous ZnO Thin Film Mater. Chem. Phys. 2019, 235, 121757.

29) Park, K.; Ko, K. Effect of TiO2 on high-temperature thermoelectric properties of ZnO J. Alloys. Compd 2007, 430, 200-204.

30) Shih, B.; Hsieh, W.; Shyue, J.; Tsai, F. Enhanced thermoelectric properties of atomic-layer-deposited Hf:Zn16O/18O superlattice films by interface-engineering Ceramics International 2020, 46, 7122-7130.

31) Chwang, R.; Smith, B.; Crowell, C. Contact Size Effects on the Van der Pauw Method for Resistivity and Hall Coefficient Measurement Solid-State Electronics 1974, 17, 1217-1227.

32) Y. Wu, S. Potts, P. Hermkens, H. Knoops, F. Roozeboom and W. Kessels, Chem. Mater. 2013, 25, 22, 4619–4622

33) Pung, S.; Choy, K.; Hou, X.; Shan, C. Nanotechnology 2008, 19, 435609.

34) Wang, F.; Zhao, X.; Duan, L.; Wang, Y.; Niu, H.; Ali, A. Structural, Optical and Electrical Properties of Hf-doped ZnO Transparent Conducting Films Prepared by Sol–

gel Method J. Alloys. Compd 2015, 623, 290-297.

35) Kumar, M.; Jeong, H.; Lee, D. Nonvolatile Memory Devices Based on Undoped and Hf- and NaF-doped ZnO Thin Film Transistors with Ag Nanowires Inserted between ZnO and Gate Insulator Interface RSC Adv. 2017, 7, 27699-27706.

36) Chang, F.; Brahma, S.; Huang, J.; Wu, Z.; Lo, K. Strong Correlation between Optical Properties and Mechanism in Deficiency of Normalized Self-assembly ZnO Nanorods Sci. Rep. 2019, 9, 905.

37) Fan, J.C.C.; Goodenough, J. B. X-ray Photoemission Spectroscopy Studies of Sn-doped Indium-oxide Films J. Appl. Phys. 1977, 48, 3524-3531.

38) Felizco, J.C.; Uenuma, M.; Ishikawa, Y.; Uraoka, Y. Optimizing the Thermoelectric Performance of InGaZnO Thin Films Depending on Crystallinity via Hydrogen Incorporation Appl. Surf. Sci. 2020, 527, 146791.

39) Mondal, P.; Das, D. Transparent and Conducting Intrinsic ZnO Thin Films Prepared at High Growth-rate with C-axis Orientation and Pyramidal Surface Texture Appl. Surf. Sci 2013, 286, 397-404.

40) Suehiro, S.; Kimura, T.; Yokoe, D.; Takahashi, S. Synthesis of Highly C-axis-oriented ZnO Thin Films using Novel Laser-enhanced Electrospray CVD under Atmospheric Pressure CrystEngComm 2017, 19, 5995-6001.

41) Vai, A.; Kuznetsov, V.; Dilworth, J.; Edwards, P. UV-induced Improvement in ZnO Thin Film Conductivity: A New In Situ Approach J. Mater. Chem. C 2014, 2, 45, 9643–9652.

42) Dasgupta, N.; Neubert, S.; Lee, W.; Trejo, O.; Lee, J.; Prinz, F.; Atomic Layer Deposition of Al-doped ZnO Films: Effect of Grain Orientation on Conductivity Chem. Mater. 2010, 22, 16, 4769-4775.

43) Kim, Y.; Tai, W. Electrical and optical properties of Al-doped ZnO thin films by sol–gel process Appl. Surf. Sci. 2007, 253, 11, 4911-4916.

Chapter 3. Optimizing the Thermoelectric Performance of InGaZnO Thin Films Depending on Crystallinity via Hydrogen Incorporation

3.1. Introduction

InGaZnO (IGZO) has recently been gaining attention as a next generation material for transparent, flexible device electronics owing to its superior carrier mobility and excellent optical transparency [1–5]. A great deal of effort has been dedicated to engineer its structure to improve its electrical properties, whether in amorphous, crystalline or nanostructured form [6–8]. It has been a well-established candidate for thin film transistors as well as memory devices [9–12]. Gearing towards the realization of transparent systems-on-panel, other applications for IGZO are currently being explored. Some of these include energy devices such as solar cells and thermoelectric devices [13–16].

A thermoelectric material is one that can directly convert heat into electrical energy without the need for any moving parts. The measure for good thermoelectricity lies on achieving high thermoelectric figure of merit (ZT) values, as defined by the following equation: $ZT = S^2\sigma/\kappa$, where S is the Seebeck coefficient, σ is the electrical conductivity, and κ is the thermal conductivity. The numerator value $S^2\sigma$ is also known as the thermoelectric power factor (PF), and is known to be difficult to maximize due to the conflicting relationships of S and σ with carrier concentration. There are previous reports on the viability of IGZO as a thermoelectric material due to the following reasons. First, its σ is easily tunable by varying the carrier concentration [14]. Our group has previously reported on the PF and thermal conductivity of amorphous InGaZnO, as well as its applicability in flexible TEGs, but the study

has been limited to optimizing the oxygen vacancies (Vo) by varying the oxygen partial pressure during deposition [14–15]. Second, its natural superlattice structure could reduce κ due to enhanced interface phonon scattering [16].

In a study by Cui et. al, the cross-plane κ of amorphous, semi-crystalline and crystalline IGZO were discussed. In their report, both amorphous and crystalline IGZO were regarded as those with low κ [16]. Similar κ values have been reported in other literature for amorphous and crystalline IGZO, ranging from 1.0-1.4 W/mK [17-19]. The low κ of amorphous IGZO is said to be likely due to strong scattering vibration modes due to the structural randomness, while that of crystalline IGZO is probably caused by the perfect superlattice structure, inducing regular changes in acoustic impedances [16]. However, although the effect of crystallinity has been discussed in relation to κ, there are currently no literature comparing the amorphous and crystalline IGZO thin films from the viewpoint of the thermoelectric *PF*. Determining how to control the *PF* of IGZO of differing crystalline properties would provide a higher impact as it affects two of the three important thermoelectric properties. Moreover, electrical conductivity improvement via post-deposition treatments, such as hydrogen annealing, plasma treatment or passivation, has been well reported for both amorphous and c-axis aligned crystalline IGZO, but their effects on the Seebeck coefficient has been left unexplored. Optimizing the post-deposition treatments can possibly enable easy functionality switching of IGZO from thin film transistor or memory device to thermoelectric generator, which can lead to the realization of future all-IGZO systems-on-panel.

A special type of c-axis aligned crystalline IGZO was developed by Yamazaki et. al in 2009 [20–28]. This material became an attractive alternative to both amorphous and single crystalline IGZO for thin film transistor applications owing to its relatively lower processing temperature but high reliability and low off-state leakage current [20-28]. Its unique structure cannot be classified as single crystalline, polycrystalline or nanocrystalline. Good crystallinity

is observed along the c-axis, but individual crystals connected with hexagonal lattice distortions compose the a-b plane. The structure therefore possesses continuous crystal morphology without visible grain boundaries [20]. However, its thermoelectric properties have not been reported up to now.

In this work, the thermoelectric properties of commercial grade amorphous (a-IGZO), c-axis aligned crystalline (c-IGZO) and crystal-embedded c-axis aligned crystalline IGZO (cc-IGZO) are reported. This study also confirms which annealing conditions favor the highest thermoelectric power factor depending on the crystallinity. Specifically, the role of hydrogen incorporation on the crystal structure in relation to their thermal transport is discussed. Although electrical conductivity improvement via hydrogen on both amorphous and crystalline IGZO has already been reported elsewhere, its role on the Seebeck coefficient as well as the overall thermoelectric performance and stability has not yet been established.

3.2. Experimental methods

3.2.1 Sample Description

Three types of IGZO thin films deposited by RF sputtering on glass substrates were used in this study – amorphous (a-IGZO), c-axis aligned crystalline (c-IGZO) and crystal-embedded c-axis aligned crystalline (cc-IGZO). All samples were provided by Sharp Corporation [27-28]. The thickness of each sample was 200 nm. The c-IGZO sample is composed almost purely of c-axis aligned crystalline IGZO throughout the film, while the cc-IGZO is likewise mainly c-axis aligned crystalline but is embedded with crystals oriented differently. The a-IGZO, on the other hand, is uniformly amorphous. The samples were 75 cm × 62 cm in size, highly transparent and with initial sheet resistances of 0.15 MΩ/sq, 0.62 MΩ/sq and 11.1 TΩ/sq, respectively.

3.2.1 Annealing

The annealing step was performed at 673 K for 2 h at a tubular furnace. To determine the effect of hydrogen incorporation on the thermoelectric performance, three annealing conditions were used – pure nitrogen, 98% N_2/2% H_2, and 96% N_2/4% H_2. The amount of hydrogen in the annealing atmosphere was controlled using an automated gas flow meter, and the hydrogen supply was stopped immediately after the 2h annealing time. Pure nitrogen was used during the furnace cool down.

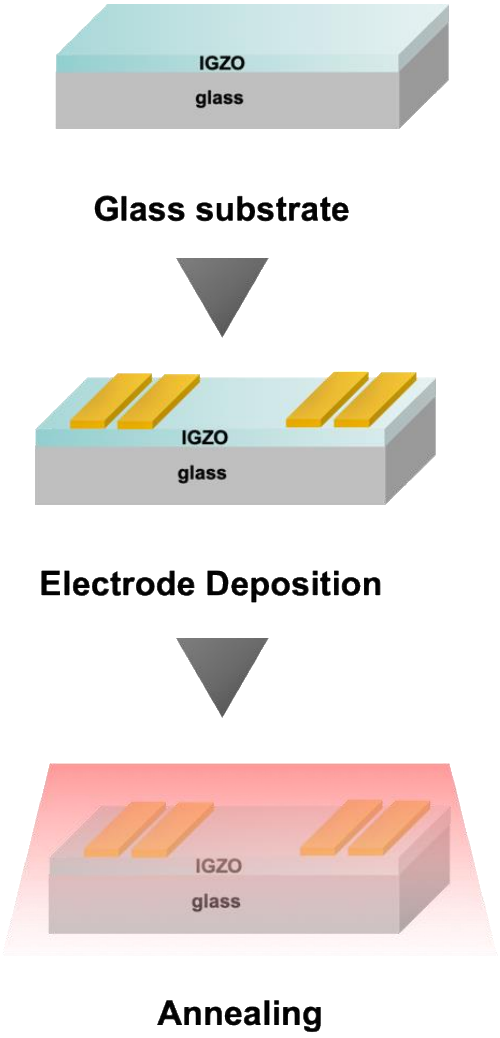

Fig. 3.1. Sample preparation procedure.

3.2.2 Characterization

To characterize the material and thermoelectric properties, samples having dimensions of 2 cm × 0.5 cm were cut from the panel-sized samples. The sample preparation procedure is detailed in Fig. 3.1. Four electrodes were deposited via electron beam evaporation of Mo (50 nm) and Au (50 nm) thin films strips following a typical four-point probe configuration. Thermoelectric measurements were then performed using a physical properties measurement system (PPMS, Quantum Design EverCool II) from 100 to 400 K under vacuum conditions. X-ray diffraction was also conducted using Rigaku X-ray diffractometer (RINT-TTR III) from $2\theta = 25–35^{o}$ under Cu Kα radiation. Secondary ion mass spectroscopy (SIMS, ULVAC-PHI, Inc. ADEPT-1010) was then conducted using Cs^{+} ion source (1 keV, 100 nA) to observe the relative amounts of oxygen and hydrogen on the samples. X-ray Photoelectron Spectroscopy (XPS, PHI5000 VersaProbeII, ULVAC-PHI) spectra were also measured at room temperature with Al-Kα radiation (1486.6 eV) to analyze the surface chemistry of the samples. Charging effects on the binding energies were calibrated with respect to the C 1s peak (284.8 eV). Transmission electron microscopy (TEM) image was obtained from JEOL JEM-3100FEF with operating voltage of 300 kV.

3.3. Results and Discussion

The TEM images of the unannealed c-IGZO and cc-IGZO samples are shown in Fig. 3.2a and b, respectively. C-axis aligned crystals are arranged in columnar structures as seen in Fig. 3.2a, with the columns connected along the a-b plane via lattice distortions instead of actual grain boundaries. As previously discussed by the Yamazaki group, continuous crystallinity is maintained along the a-b plane owing to these lattice distortions, but does not impede charge transport as in the case of grain boundaries [20]. On the other hand, the cc-IGZO sample shows mainly c-axis oriented columnar crystals, but the presence of crystals revealing a different orientation can also be observed (boxed in Fig. 3.2b). Such crystal structures likely arose from some remaining amorphous portions in the film which crystallized at a later stage in the crystallization phase compared to its neighboring crystals. The structural properties of the unannealed samples were also examined using X-ray diffraction (XRD). Figure 3.2c shows the normalized out-of-plane XRD spectra of the unannealed a-IGZO, c-IGZO and cc-IGZO samples. The a-IGZO samples simply revealed a broad amorphous IGZO peak at around 33º, and a wide 24º peak attributable to the silica glass substrate [18]. The c-IGZO and cc-IGZO samples, on the other hand, revealed a crystalline peak at about $2\theta = 31º$, which represents the (009) IGZO plane [20, 22-26]. This signifies the presence of c-axis aligned crystalline IGZO.

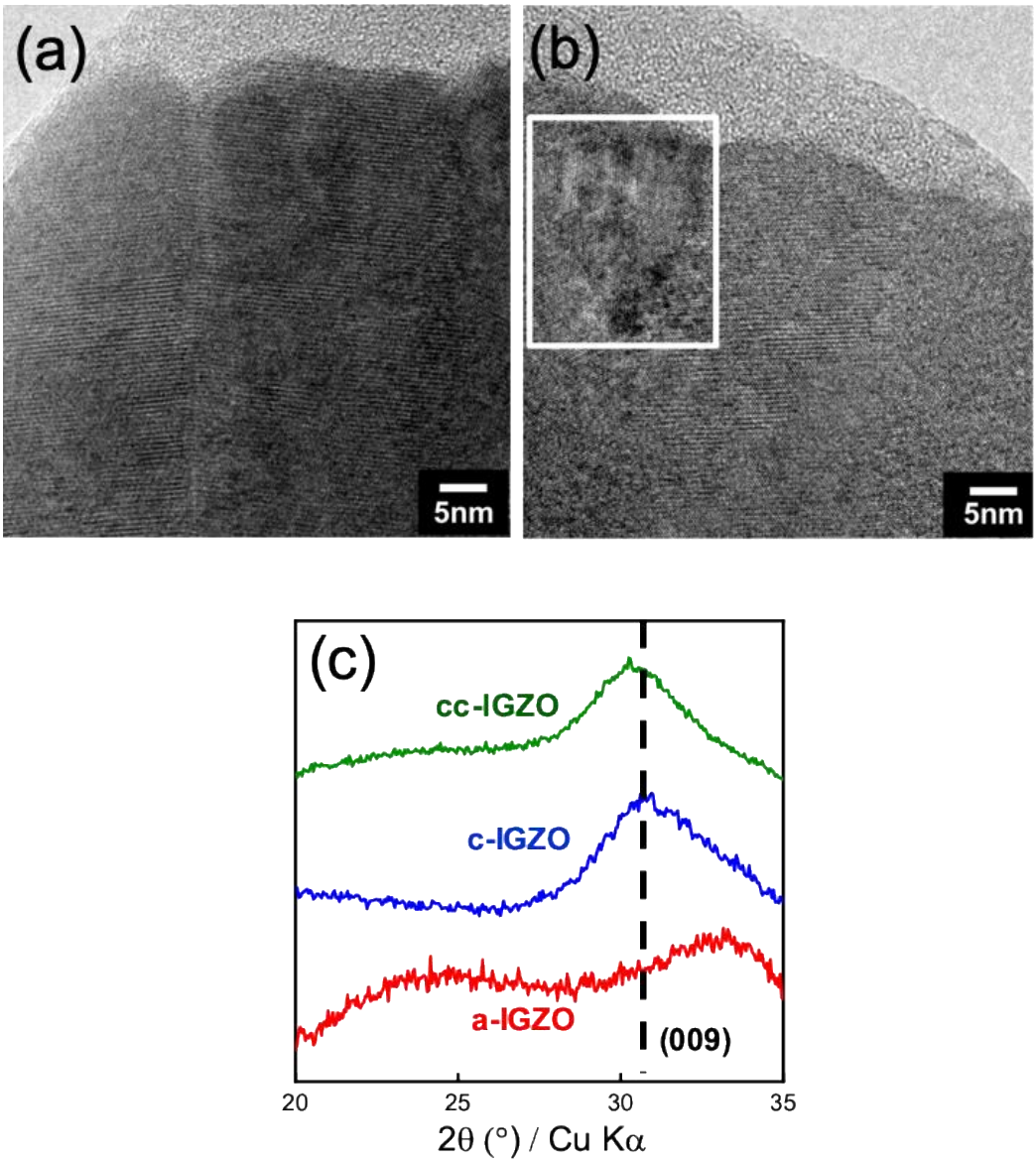

Fig. 3.2. TEM images of (a) c-IGZO and (b) cc-IGZO samples. (c) XRD spectra showing the (009) peak all unannealed IGZO thin film samples.

The thermoelectric performance of the annealed samples was then evaluated from 100 to 400 K and the properties are shown in Fig. 3.3. The N_2-annealed samples are referred to as a-N_2, c-N_2, and cc-N_2, while the samples annealed under N_2 with 4% H_2 are named a-H_2, c-H_2 and cc-H_2. The properties of the unannealed (UA) samples were not included as they exhibited resistance values way above the measurement system limit (< 2 MΩ). The electrical conductivities of all the samples in Fig. 3.3a displayed little temperature dependence, except

for the cc-N_2 sample. The samples with the highest σ are the a-H_2 and the c-H_2 samples, with values of 463 S/cm and 327 S/cm at 100 K, respectively. Their N_2-annealed counterparts displayed lower electrical conductivities, suggesting that hydrogen incorporation is effective in increasing σ regardless of crystallinity, consistent with previous reports [20, 29–31]. The c-IGZO samples showed a similar trend, but remained at low σ values. The Seebeck coefficients, on the other hand, showed obvious temperature dependence. Also, an exact inverse trend with σ is observed for the a-IGZO and c-IGZO, wherein a-H_2 and c-N_2, which displayed the highest and the lowest σ, showed the lowest and the highest S. This is expected since the carrier concentration, which is known to be directly proportional to σ, has an inverse effect on *S*. Finally, the *PF* of the samples showed a similar temperature dependence as with *S*. As shown in Fig. 1c, the highest *PF* value achieved is for the a-N_2 sample at 390 K, which is 0.093 mW/mK^2. For the crystalline samples, the highest *PF* is that of c-H_2, with 0.081 mW/mK^2, and 0.031 mW/mK^2 for cc-H_2 at 390 K.

To aid in understanding the effect of temperature on the electronic properties of the samples, a percolation conduction model is applied, as it has sufficiently explained the conduction behavior in previous ZnO-based thin films [32-33]. This conduction model suggests that the long-range electrical conduction is inhibited by energy barriers caused by structural randomness, which likely originates from the random distribution of Ga^{3+} and Zn^{2+} ions in the IGZO lattice. The temperature dependence of the percolation model states that the log σ generally shows a linear behavior with $T^{-1/4}$ following the equation: $\log \sigma = A - BT^{-1/4}$, where 1/B corresponds to the correlation radius of the conducting networks [32]. Shown in Fig. 3.3d is the graph of log σ vs $T^{-1/4}$ for all samples. Samples a-N_2 and c-H_2 showed a very weak decrease in log σ as $T^{-1/4}$ decreases. This suggests an almost metallic behavior, and such a decrease in σ as a function of *T* is likely induced by slight phonon scattering. On the other hand, the rest of the samples showed a direct linear proportionality with *T*, with the cc-N_2 exhibiting

the largest slope. This perfectly resembles the thermal dependence behavior of the percolation conduction model. A higher negative slope indicates a greater tendency for thermal excitation to increase the number of electrons. This could probably explain the highest Seebeck coefficients observed for the cc-N_2 sample at any temperature, followed by c-N_2 and a-N_2.

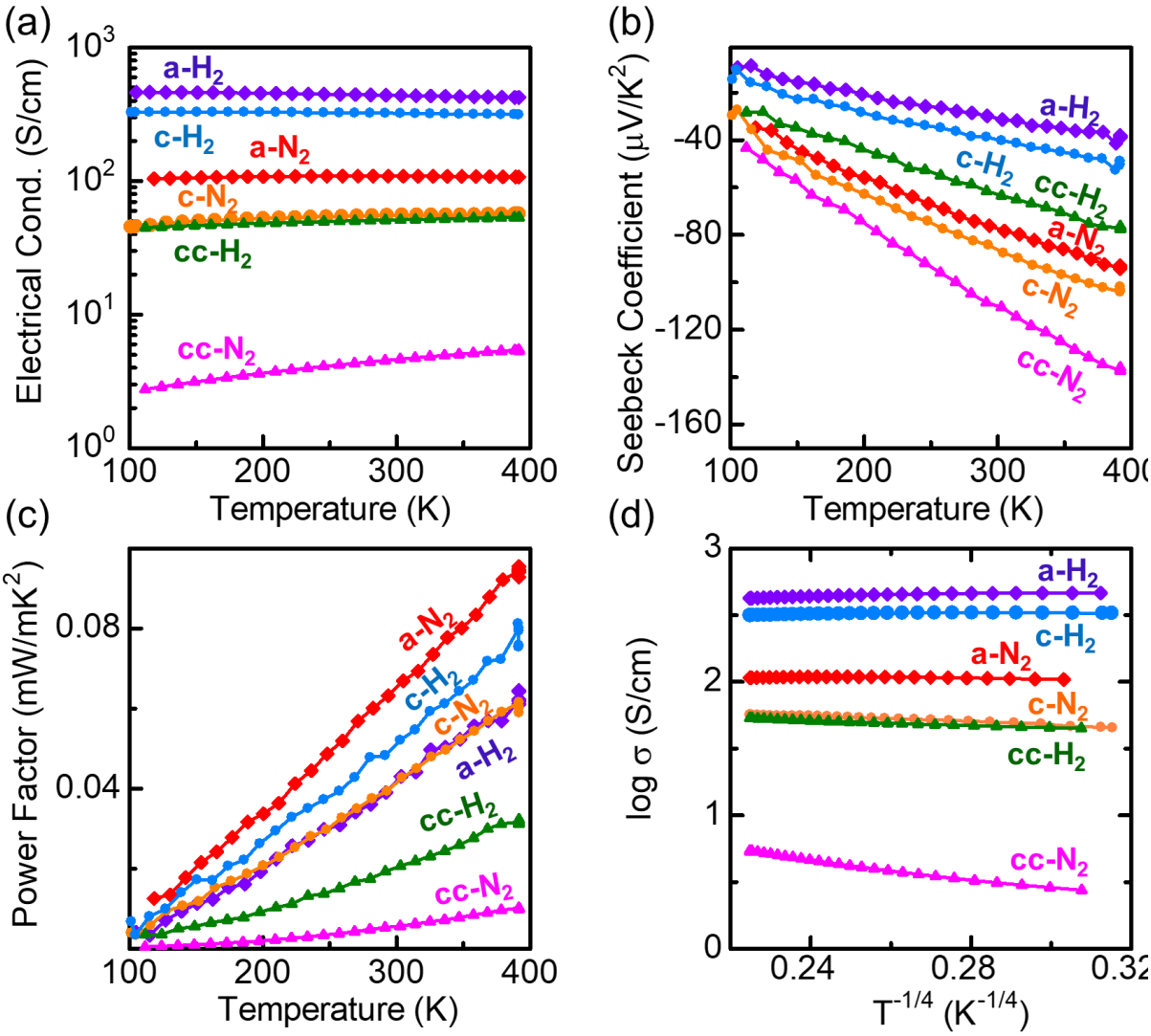

Fig. 3.3. (a) Electrical conductivity, (b) Seebeck coefficient and (c) power factor values of all IGZO samples from 100 to 400 K, and (d) plot of log σ vs $T^{-1/4}$.

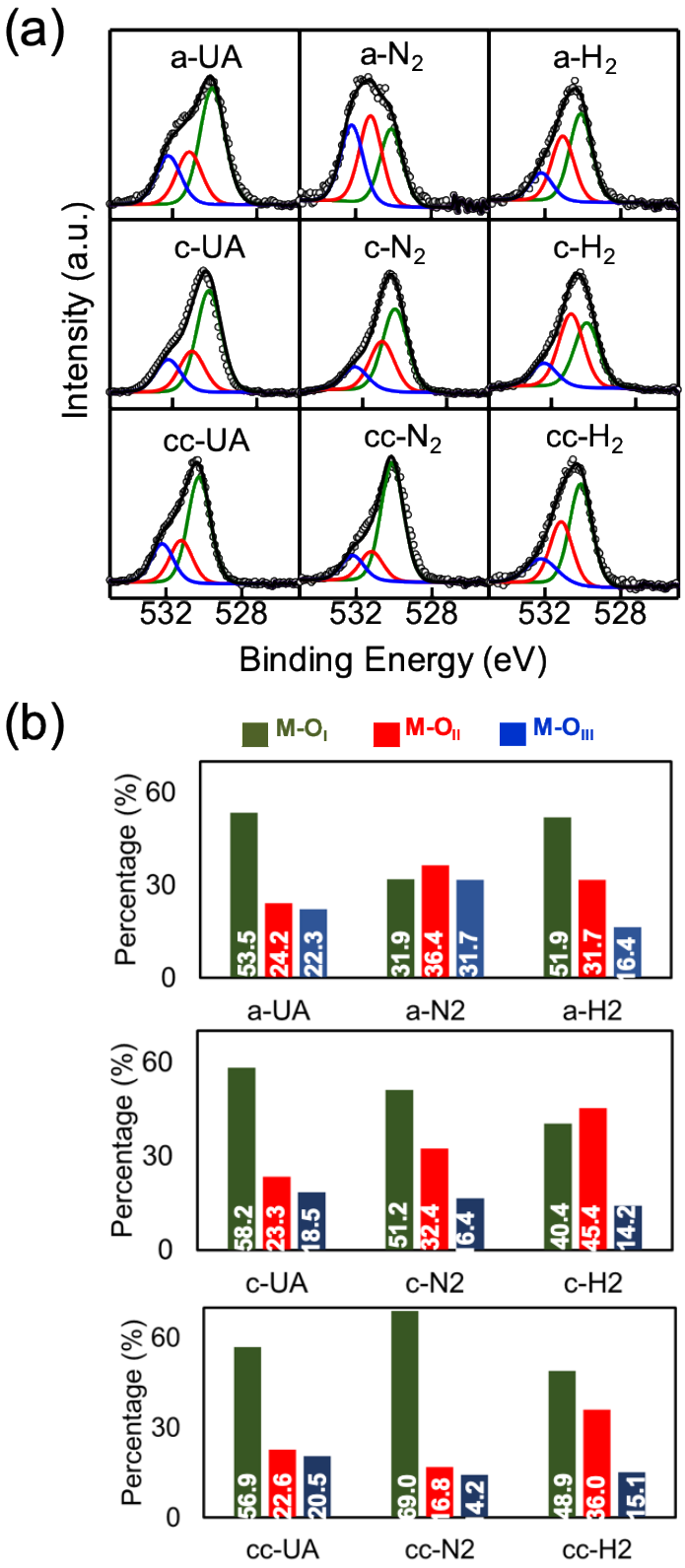

Fig. 3.4. (a) High-resolution XPS O1s peaks of the unannealed (UA), pure N_2-annealed and N_2 with 4% H_2-annealed samples, and (b) the corresponding peak area percentages of the O1s deconvoluted peaks.

In order to provide a deeper insight regarding the oxygen-related defects, which usually plays a major role in the electrical properties of IGZO, the O1s core level XPS spectra of all the samples were investigated and displayed in Fig. 3.4. The peaks were calibrated with respect to the C1s peak (284.8 eV) to account for the effects of charging. The O1s can be deconvoluted into three peaks located at 530.2 ± 0.1 eV, 531.1 ± 0.1 eV and 532.4 ± 0.2 eV, which can typically be attributed to oxygen in metal oxide lattice (M-O_I), oxygen in the IGZO lattice with oxygen vacancies (M-O_{II}), and hydroxyl and other carbon-related impurities (M-OH), respectively [34]. The relative percentages of the deconvoluted peaks in each sample are quantified in Fig. 3.4b. Among the unannealed samples, the a-IGZO sample revealed the least amount of M-O and the highest amount of M-O_{II}. This is likely due to the highly ordered structure of both the crystalline samples, wherein M-O bonds are more intact. In contrast, M-O_{II} formation is most likely to occur in a-IGZO owing to the short-range order. Annealing with N_2 revealed varying effects depending on the crystallinity. In a-IGZO, the M-O_{II} greatly increased as expected, since the Vo formation is enhanced by heating paired with exposure to an O_2-poor environment. A similar effect was observed on c-IGZO, although the M-O maintained its dominance over the M-O_{II}. However, for the cc-IGZO sample, annealing with pure N_2 did not increase the M-O_{II}. Instead, it greatly enhanced the M-O bonds. This suggests that the structure is highly stable, such that oxygen-related defects are very difficult to form, as has been previously reported [35]. Introducing H_2 in the annealing environment also affected the samples differently. The c-H_2 revealed a great increase in M-O_{II} compared to the unannealed c-IGZO, which is in fact the highest of all the samples. A similar effect was observed with cc-H_2, although the M-O_{II} area percentage remained at a lower level. This suggests that the incorporation of H_2 in the annealing atmosphere for crystalline IGZO results to a concurrent increase in oxygen vacancies, as has been previously observed in CAAC-IGZO fabricated by the Yamazaki group [20]. However, the lower amount of M-O_{II} in a-H_2 compared

to a-N_2 suggests that the H atoms could have been simultaneously passivating some of the Vo as they form. This can also explain the lower amount of M-OH in the H_2-annealed samples compared to the N_2-annealed samples for the a-IGZO and c-IGZO, since the H^+ could have been bonding with the metallic dangling bonds or existing as interstitial defects. It should be noted, however, that the trend exhibited by the samples in terms of amount of M-O_{II} does not exactly coincide with that of σ. For example, the a-H_2 sample exhibited the highest σ, but possessed one of the lowest amounts of M-O_{II}. This greatly implies that the Vo is not the only key player in enhancing the σ and the PF. As H^+ is a well-known source of free carriers whether as a substitutional or interstitial defect, it is probably equally responsible for the thermoelectric behavior of the samples.

To prove this, the effect of hydrogen on the samples was further investigated by varying the H_2 concentration in the N_2 annealing atmosphere (0%, 2% and 4%). Displayed in Fig. 3.5 is the effect of hydrogen concentration on the *PF*, σ and *S* of the samples at 300 K. The *PF* of the samples obviously exhibited varying reactions to increasing amount of hydrogen – the a-IGZO being negatively affected, the c-IGZO only slightly changing, and the cc-IGZO greatly increasing. The σ of c-IGZO and cc-IGZO appeared to be increasing with the amount of hydrogen, while the a-IGZO seemed to have peaked at 2%. The positive effect on both the σ and *PF* of the c-IGZO and cc-IGZO samples supports the previous observation that H is effective in improving the electrical properties. In the case of a-H_2, it is likely that there is only an optimum amount of hydrogen that aids in its electron transport, and an excess amount possibly introduces a large amount of interstitial defects [31]. The S displayed a perfectly inverse effect as with σ. Both c-IGZO and cc-IGZO samples exhibited decreasing *S* with % hydrogen, while a-IGZO displayed the lowest S at 2%. This can be related to their electron mobility values. This is known to be inversely proportional with effective mass, which in turn directly relates with S [36]. Introducing hydrogen into the system passivates the defects,

leading to reduced trap sites and improved electron mobility. This decreases the effective mass, which translates to lower *S* values.

It is also important to determine how much of the hydrogen in the annealing environment is being incorporated in the samples, and if it depends on their crystallinity. SIMS analysis was then employed to look into the differences in hydrogen content of the hydrogen-annealed samples. The normalized SIMS spectra are presented in Fig. 3.5d. The amount of hydrogen is the highest with cc-IGZO, followed by the a-IGZO, and then the c-IGZO. It can also be observed that the amount of hydrogen is constantly varying with increasing penetration depths for both cc-IGZO and c-IGZO samples, as opposed to the a-IGZO sample which exhibited an almost uniform amount of hydrogen all throughout the thin film depth. The high H amounts in the cc-IGZO film possibly provide an explanation on the great effect on its TE properties as an effect of % H_2. Increasing the hydrogen content could probably further improve the properties of cc-IGZO, but is not very safe especially for large scale fabrication processes. In the case of c-IGZO and a-IGZO, although their H contents are about the same level, a-H_2 still possesses much greater σ than c-H_2. This implies that the combined effect of Vo and H is important in maximizing the thermoelectric *PF*, and that the mechanisms are different depending on the crystallinity.

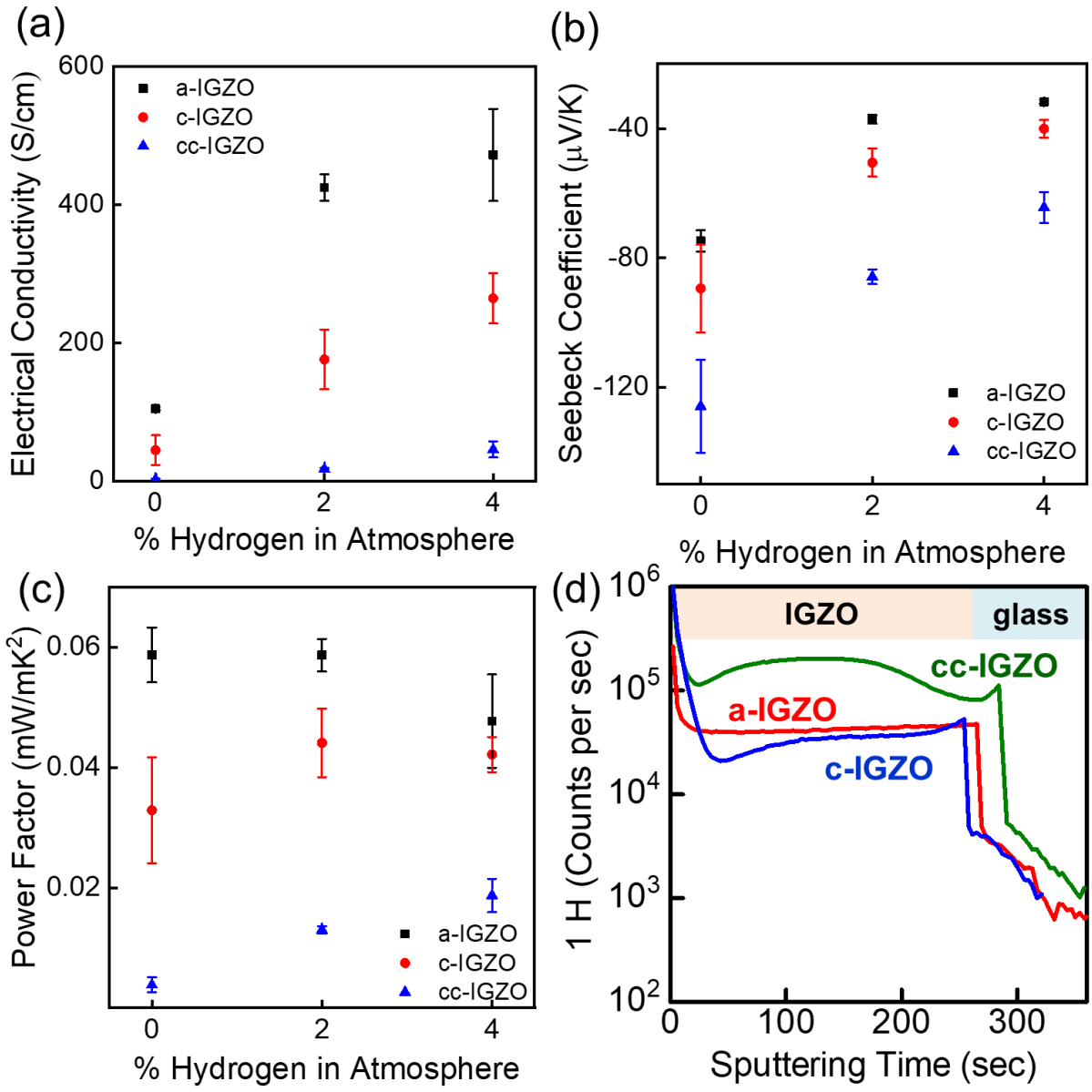

Fig. 3.5. (a) Power factor, (b) electrical conductivity and (c) Seebeck coefficient values of IGZO samples as an effect of increasing % hydrogen in the N_2 annealing atmosphere. (d) SIMS 1H spectrum of all H_2-annealed IGZO samples.

A Jonker plot was also constructed and shown in Fig. 3.6a to provide an insight on the degeneracy of the IGZO depending on crystallinity as an effect of the % H_2. Jonker plots revealed slopes of 70.9, 60.0 and 54.3 μV/K for the a-IGZO, c-IGZO and cc-IGZO samples, respectively. Positive values indicate typical n-type characteristic. In nondegenerate

semiconductors, the relationship between S and log σ can be expressed by $S = \pm k/e(\ln\sigma - \ln\sigma_0)$ [14]. Therefore, the Jonker slope of a typical nondegenerate semiconductor is a constant value, which is about 198 μV/K [14]. Since the slopes of all samples did not coincide with this value, the samples then do not tend to behave like a typical non-degenerated semiconductor. This could be related to the metallic behavior exhibited by the H_2-annealed samples as explained above. This suggests that the incorporation of hydrogen in the annealing atmosphere may lead to a degenerated behavior for the InGaZnO, which translates to extremely high electrical conductivities, but not necessarily high *PF*.

To more clearly illustrate the effect of hydrogen on the *PF*, the measured *PF* of all samples were plotted against σ in Fig. 3.6b. The UA sample for cc-IGZO was excluded due to its extremely high resistance. A theoretical plot of the relationship between σ and *PF* was also included, which was calculated using the Kamiya-Nomura percolation model in IGZO [14, 37–38]. Standard Boltzmann transport formalism is applied using the percolation conduction model earlier described. The calculation is based on the mathematical approach proposed by Adler, et. al. [39]. The measured properties of the samples fit quite well with the theoretical *PF* values, which suggests that a-IGZO achieved nearly the maximum *PF* at 0% H_2 annealing. Further increasing the σ by introducing H^+ ions would only likely decrease its PF, as predicted by the percolation model. The c-IGZO, however, could probably reach a higher *PF* when the conductivity can be controlled to range from 100–280 S/cm. Finally, cc-IGZO shows potential to reach maximum *PF* when σ can be further enhanced, but as earlier mentioned, increasing the hydrogen amount in the annealing environment is not very safe and practical.

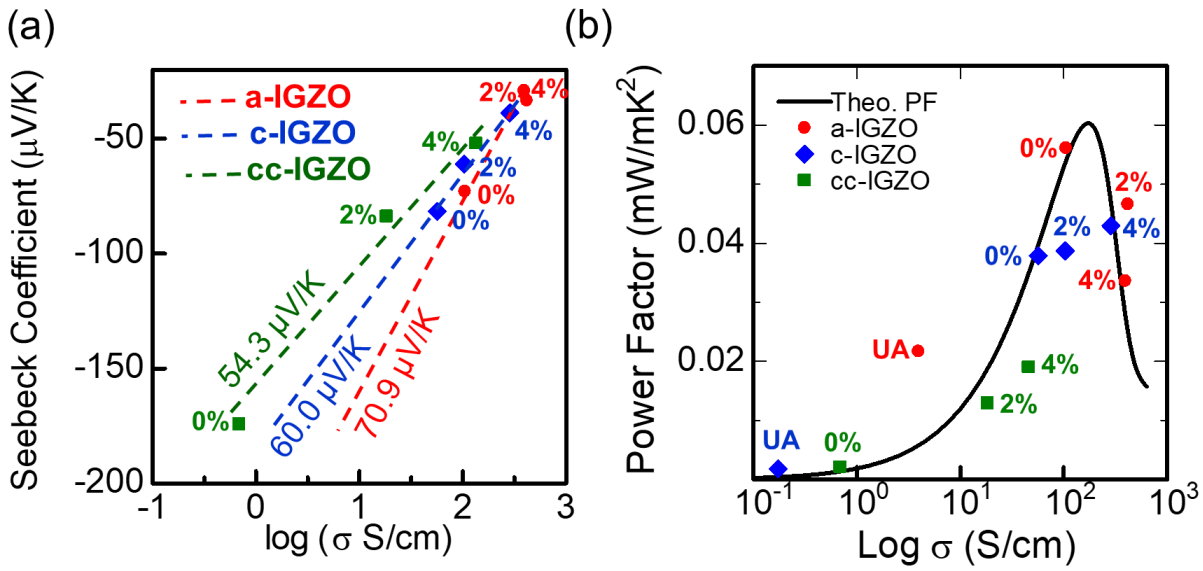

Fig. 3.6. (a) Jonker plot as an effect of % H_2, and (b) Log σ-PF plot of all IGZO samples plotted against theoretical PF.

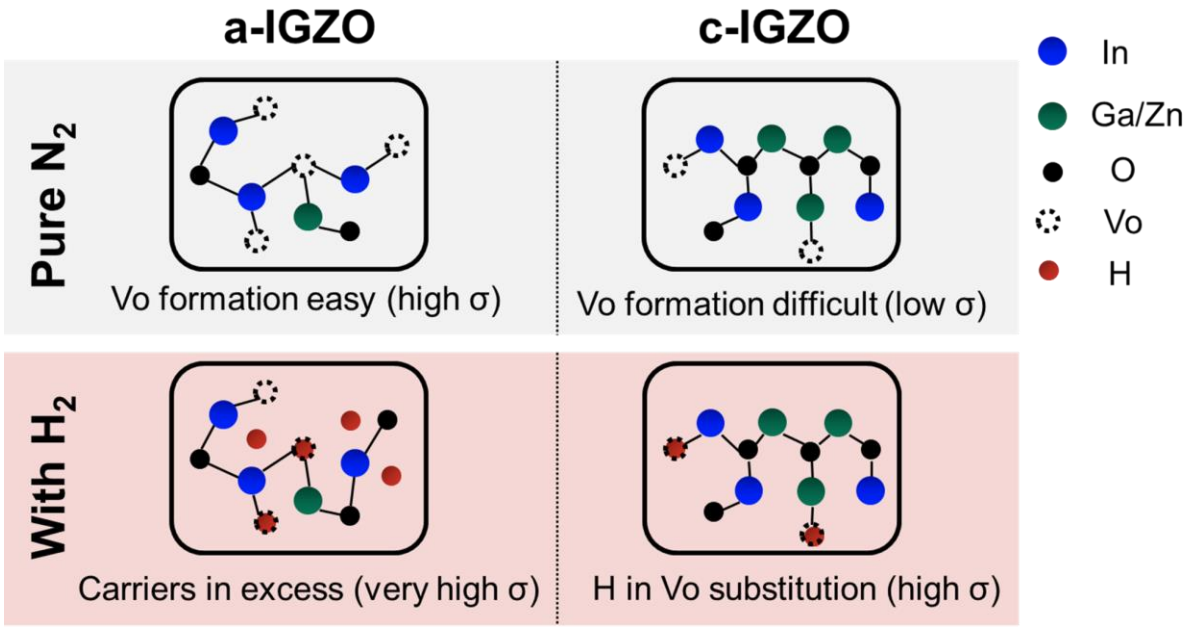

Fig. 3.7. Schematic diagram of the proposed mechanism.

Fig. 3.7 illustrates the proposed mechanism by which the annealing atmosphere affects the electrical conductivity of the InGaZnO thin films. Under pure nitrogen annealing, oxygen vacancies were easily formed in a-IGZO owing to the short-range order. It has been previously reported that Vo acts as a deep donor, which is likely responsible for the increase in σ [40-41]. Combined with the moderate *S* values of a-IGZO, which probably originated from the high effective mass due to the high density of defects that traps the electrons, an almost maximum *PF* is achieved. In the case of c-IGZO, Vo formation could be more difficult due to the highly stable and orderly structure, so the carriers from oxygen vacancies are probably insufficient to increase the σ. On the other hand, incorporating hydrogen in the annealing atmosphere possibly led to an excessive amount of carriers for a-IGZO, which was good for achieving high σ but significantly decreased the *S*. Hydrogen annealing appeared to be more effective in the case of c-IGZO, wherein the additional carriers from hydrogen-related defects such as hydrogen substitution onto Vo sites (Ho) or interstitial H^+ are important to achieve the optimum σ values. Both Ho and interstitial H^+, in contrast with the deep donor Vo, are said to act as shallow donor-like states and therefore greatly contribute to improved electron conduction in c-IGZO [40-41]. Also, the unique c-axis aligned crystallinity paired with the superlattice structure likely improves the interfacial phonon scattering, leading to higher *S* compared to a-H_2. However, the embedded crystals in the cc-IGZO thin film could be hindering the electron transport, which is likely the cause for the extremely high initial resistance. However, they contributed greatly to increasing the S, wherein the cc-N_2 achieved the highest S among all the samples. Therefore, in the case of a-IGZO, the best condition to maximize the thermoelectric PF is by the Vo-driven pure N_2 annealing, while for c-IGZO and cc-IGZO, the Ho-driven H_2 annealing is ideal.

Other techniques can be similarly employed in order to introduce charge carriers in the InGaZnO thin films. For example, excimer laser annealing (ELA) can be utilized to chieve a similar effect without elevating the temperature of the substrate. Presented in Fig. 3.8 are the

temperature-dependent thermoelectric properties of a-IGZO thin films subjected to 100, 120 and 140 mJ/cm^2 KrF ELA (λ = 248 nm, pulsewidth = 9 ns). The electrical conductivity was evidently increased by ELA without much change in the Seebeck coefficient, which effectively led to an improvement in the PF. This can be attributed to the formation of oxygen-related defects, which caused an enhancement in the electron mobility [42]. By using Comsol simulation, the maximum temperature applied to the surface of the thin film was determined to be 1550, 1806 and 2031 K for ELA laser fluences of 100, 120 and 140 mJ/cm^2, while the substrate temperature remained at near room temperature for all cases. Although the thermoelectric performance of the thermally annealed IGZO thin films described earlier remained better, ELA treatment can potentially be more suitable when utilizing polymeric substrates for flexible electronics applications.

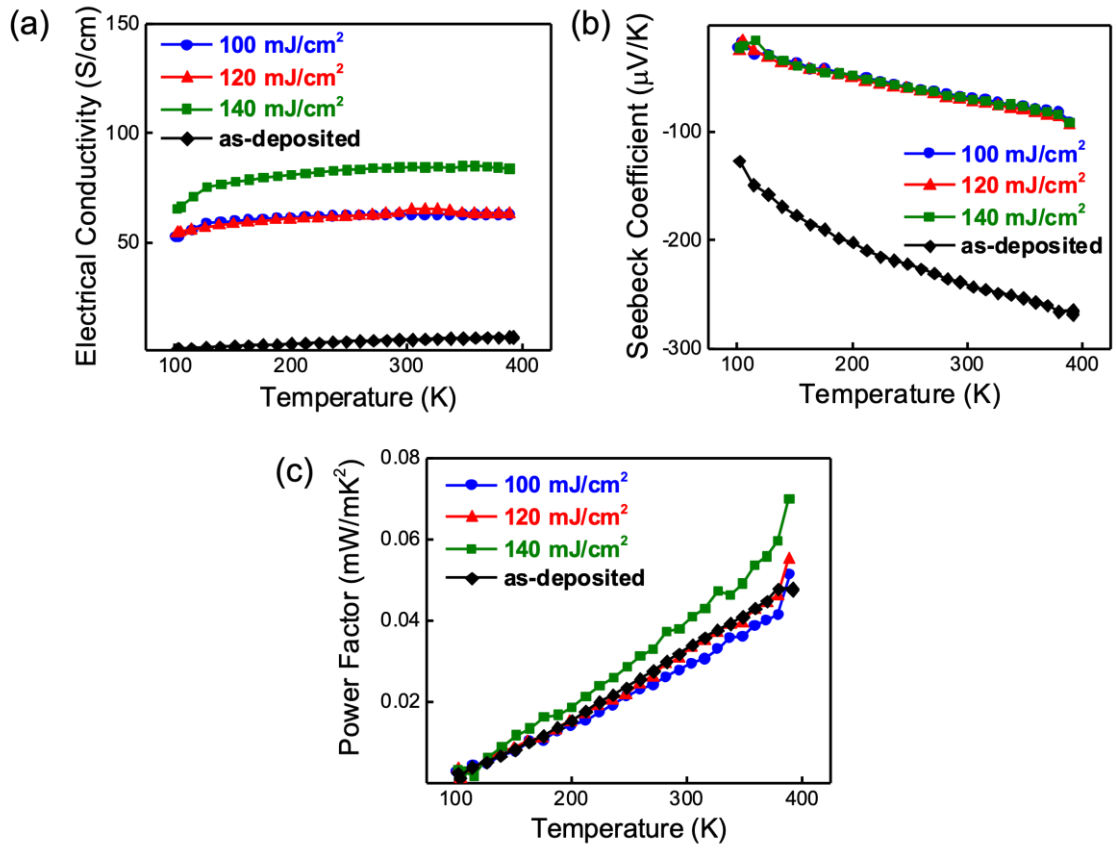

Fig. 3.8. Temperature-dependent (a) electrical conductivity, (b) Seebeck coefficient and (c) power factor of ELA-treated a-IGZO thin films.

3.4. Summary

The thermoelectric properties of amorphous, c-axis aligned crystalline and crystal-embedded c-axis aligned crystalline IGZO were reported in this study. Varying the annealing atmosphere by incorporating hydrogen was also performed to determine the ideal annealing environment depending on the crystalline type, and investigate which driving forces are responsible in enhancing their power factor. The a-N_2 sample displayed the highest power factor, which suggests that the thermoelectric performance remains better when InGaZnO is amorphous rather than crystalline phase. However, adding hydrogen in the annealing atmosphere significantly improved the performance of the c-IGZO sample, while the cc-IGZO retained relatively low power factors even after annealing. XRD analysis revealed that H_2 annealing successfully retained the c-axis alignment for both the c-IGZO and cc-IGZO samples, which was likely responsible for obtaining better properties. The oxygen-related defects as well as the hydrogen contents of the samples were also investigated using XPS and SIMS, respectively, which revealed that for a-IGZO, the formation of a high amount of Vo is responsible for its superior thermoelectric properties, while the combined effect of Vo and Ho is the driving force in the case of both c-IGZO and cc-IGZO.

References

1) K. Nomura, H. Ohta, A. Takagi, T. Kamiya, M. Hirano, and H. Hosono, Nature 432, 488–492 (2004).

2) C. Kulchaisit, J. P. S. Bermundo, M. N. Fujii, Y. Ishikawa, and Y. Uraoka, AIP Adv. **8**, 095001 (2018).

3) S. J. Kim, S. Yoon, and H. J. Kim, Jpn. J. Appl. Phys. 53, 02BA02 (2014).

4) P. Heremans, A. K. Tripathi, A.de Jamblinne de Meux, E. C. P. Smits, B. Hou, G. Pourtois, and G. H. Gelinck, Adv. Mater. 28, 4266–4282 (2016).

5) S. Jeong, J. Lee, S. S. Lee, Y. Seo, S. Kim, J. Park, B. Ryu, W. Yang, J. Moon, and Y. Choi, J. Mater. Chem. C 1, 4236–4243 (2013).

6) J. C. Felizco, M. Uenuma, D. Senaha, Y. Ishikawa, and Y. Uraoka, Appl. Phys. Lett. 111, 033104 (2017).

7) J. C. Felizco, M. Uenuma, D. Senaha, Y. Ishikawa, and Y. Uraoka, IEEE 24th International Workshop on Active-Matrix Flatpanel Displays and Devices (AM-FPD), 283–284 (2017).

8) K. Umeda, M. Uenuma, D. Senaha, J. C. Felizco, Y. Uraoka, and H. Adachi, J. Phys. Conf. Ser. 1052, 012016 (2018).

9) Y. Yamauchi, Y. Kamakura, Y. Isagi, T. Matsuoka, and S. Malotaux, Jpn. J. Appl. Phys. 53, 089201 (2014).

10) T. Hwang, I. Yang, O. Kwon, M. Ryu, C. Byun, C. Hwang, and S. K. Park, Jpn. J. Appl. Phys. 50, 03CB06 (2011).

11) K. Kado, M. Uenuma, K. Sharma, H. Yamazaki, S. Urakawa, Y. Ishikawa, and Y. Uraoka, Appl. Phys. Lett. 105, 123506 (2014).

12) C. Hsu, Y. Fan, and P. Liu, Appl. Phys. Lett. 102, 062905 (2013).

13) J. Hou, S. Chang, C. Wu, H. Hong, and T. Hsueh, ECS J. Solid State Sci. Technol. 6, Q120–Q122 (2017).

14) Y. Fujimoto, M. Uenuma, Y. Ishikawa, and Y. Uraoka, AIP Adv. 5, 097209 (2015).

15) M. Uenuma, K. Umeda, J. Felizco, D. Senaha, and Y. Uraoka, J. Elec. Mater. 48, 1971–1975 (2019).

16) B. Cui, L. Zeng, D. Keane, M. Bedzyk, D. Buchholz, R. Chang, X. Yu, J. Smith, T. Marks, Y. Xia, A. Facchetti, J. Medvedeva and M. Grayson, J. Phys. Chem. C 120, 7467−7475 (2016).

17) M. Uenuma, J. C. Felizco, D. Senaha and Y. Uraoka, IOP Conf. Series: Journal of Physics: Conf. Series 1052, 012011 (2018).

18) T. Yoshikawa, T. Yagi, N. Oka, J. Jia, Y. Yamashita, K. Hattori, Y. Seino, N. Taketoshi, T. Baba, and Y. Shigesato, Appl. Phys. Express, 6, 021101 (2013).

19) D. Seo, S. Shin, H. Cho, B. Kong, D. Whang, and H. Cho, Acta Mater. 59, 17, 6743-6750 (2011).

20) N. Kimizuka and S. Yamazaki, Physics and Technology of Crystalline Oxide Semiconductor CAAC-IGZO: Fundamentals (John Wiley & Sons, Ltd., Chichester, 2016) 2nd ed.

21) M. Lee and J. Dho, J. Kor. Phys. Soc. 58, 3, pp. 492∼497 (2011).

22) S. Yamazaki, S. Ohshita, M. Oota, H. Baba, T. Onuki, H. Kunitake, K. Ohshima, D. Shimada, H. Kimura, T. Murakawa, T. Atsumi, and K. Kato, Int. J. Ceramic Eng. Sci. 1, 6–20 (2019).

23) S. Yamazaki, T. Atsumi, K. Dairiki, K. Okazaki and N. Kimizuka, ECS J. Solid State Sci. Technol. 3, Q3012–Q3022 (2014).

24) S. Yamazaki, ECS Trans. 64, 155–164 (2014).

25) S. Yamazaki, H. Suzawa, K. Inoue, K. Kato, T. Hirohashi, K. Okazaki, and N. Kimizuka,

Jpn. J. Appl. Phys. 53, 04ED18 (2014).

26) M. Kozuma, Y. Okamoto, T. Nakagawa, T. Aoki, M. Ikeda, T. Osada, Y. Kurokawa, T. Ikeda, N. Yamade, Y. Okazaki, H. Miyairi, M. Fujita, J. Koyama, and S. Yamazaki, Jpn. J. Appl. Phys. 53, 04EE12 (2014).

27) S. Yamazaki, J. Koyama, Y. Yamamoto, and K. Okamoto, SID 2012 Digest, 183–186 (2012).

28) Y. Yamada, D. Matsubayashi, S. Matsuda, Y. Sato, M. Ota, D. Ito, M. Tsubuku, Masahiro Takahashi, Takuya Hirohashi, Masayuki Sakakura, and Shunpei Yamazaki, Jap. J. Appl. Phys 53, 091102 (2014).

29) H. Li, Y. Guo, and J. Robertson, Sci. Rep. 7, 16858 (2017).

30) A. Abliz, Q. Gao, D. Wan, X. Liu, L. Xu, C. Liu, C. Jiang, X. Li, H. Chen, T. Guo, J. Li and L. Liao, ACS Appl. Mater. Inter. 9, 10798−10804 (2017).

31) Y. Nam, H. Kim, S. H. Cho, and S. K. Park, RSC Adv. 8, 5622−5628 (2018).

32) H. Sim, S. Choi, J. Park, J. Song, S. Han, C. S. Hwang, and D. Cho, ECS J. Solid State Sci. Technol. 3, P10−P12 (2014).

33) A. Takagi, K. Nomura, H. Ohta, H. Yanagi, T. Kamiya, M. Hirano and H. Hosono, Thin Solid Films 486, 38–41 (2005).

34) J. C. C. Fan and J. B. Goodenough, J. Appl. Phys. 48, 3524−3531 (1977).

35) T. Hiramatsu, M. Nakashima, E. Kikuchi, N. Ishihara, M. Tsubuku, K. Dairiki and S. Yamazaki, Jpn. J. Appl. Phys. 55, 021203 (2016).

36) N. H. T. Nguyen, T. H. Nguyen, Y. Liu, M. Aminzare, A. T. T. Pham, S. Cho, D. P. Wong, K. Chen, T. Seetawan, N. K. Pham, H. K. T. Ta, V. C. Tran, and T. B. Phan, ACS Appl. Mater. Inter. 8, 33916−33923 (2016).

37) T. Kamiya, K. Nomura, and H. Hosono, Appl. Phys. Lett. 96, 122103 (2010).

38) T. Kamiya, K. Nomura, and H. Hosono, J. Display Technol. 5, 462−467 (2009).

39) D. Adler, L. Flora, and S. Senturia, Solid State Commun. 12, 9-12 (1973).

40) A. Janotti, and C. Van de Walle, Nature Materials 6, 44–47 (2007).

41) C. Chen, B. Yang, G. Li, H. Zhou, B. Huang, Q. Wu, R. Zhan, Y. Noh, T. Minari, S. Zhang, S. Deng, H. Sirringhaus, and C. Liu, Adv. Sci. 6, 1801189 (2019).

42) B. Ahn, W. Jeong, H. Shin, D. Kim, H. Kim, J. Jeong, S. Choi and M. Han, Electrochem. Solid-State Lett. 12 H430, 2009.

Chapter 4. Gate-Tunable Thermoelectric Properties Along the Oxide/Insulator Interface in an InGaZnO Thin Film Transistor

4.1. Introduction

Among transparent amorphous oxide semiconductors, indium gallium zinc oxide (InGaZnO) is one of the most well-explored channel layers for thin film transistors (TFT). This is likely owing to its facile large scale and low temperature processability, making it desirable for future flexible electronics [1-5]. More importantly, amorphous InGaZnO exhibits excellent electrical properties, such as superior mobility, high controllability over carrier concentration (n), and low leakage current [1-5]. This makes InGaZnO an ideal semiconductor material not only for TFTs but also for a wide array of transparent, flexible electronic devices.

Among the electronic applications explored for InGaZnO, its thermoelectric properties are relatively less-explored. Thermoelectric materials are those that can directly convert waste heat into usable energy [6]. They are characterized by the thermoelectric figure of merit zT ($zT = S^2\sigma/\kappa$), where S is the Seebeck coefficient, σ is the electrical conductivity and κ is the thermal conductivity. Thermoelectric generation in InGaZnO thin films has been reported in a few previous literature [7-11]. However, the thermoelectric power factor ($PF = S^2\sigma$) which represents the electrical contribution to zT, remains relatively low owing to an apparent limit from the coupling inverse relation between S and σ. This arises from their opposing relationships with n, wherein σ varies linearly while S depends inversely. Therefore, in order to enhance the PF of InGaZnO materials, it is important to devise a technique to

decouple S and σ. A common approach is to confine the electrons in an extremely narrow quantum well. Some ways to achieve this is by creating nanostructures or two-dimensional electron systems [12-14]. Another method is by integrating the thermoelectric material in a TFT structure, wherein the thermoelectric oxide is contacted with a gate insulator. Through the application of voltage via a gate electrode, the charge carriers are confined within a narrow region in the vicinity of the oxide/insulator interface [15-18]. Liang, et. al. has reported the modulation of the Seebeck coefficient of an a-SnO_2 TFT by gate bias modulation, which they used to investigate its gas sensing properties [15]. Shimizu, et. al, on the other hand, saw a remarkable enhancement in the thermoelectric power factor of ZnO when ion-gated in a TFT device structure, owing to the formation of a two-dimensional electron gas at the oxide/channel interface [16]. However, the thermoelectric generation in an InGaZnO thin film transistor has not been reported.

In this study, the thermoelectric properties at the gate insulator (GI)/channel interface in a typical InGaZnO TFT with SiO_2 GI is investigated. With the application of a positive gate voltage (V_G), the thermoelectric *PF* at this area is observed to achieve a significant increase up to three orders of magnitude owing to an accumulation of charge carriers at the GI/channel interface. The S showed a slightly decreasing dependence on V_G, but was minimal enough to maintain a respectable *PF* up to 0.1 mW/mK^2. Negligible thermoelectric *PF* can be obtained without V_G or at negative applied V_G, which corroborates to the off state of the transistor. Lastly, analysis using the Kamiya-Nomura percolation model reveals that the TFT displays superior properties against pristine InGaZnO thin films, and is estimated to yield twice the *PF*. This study demonstrates the feasibility of a thermoelectrically-active TFT that can pave the way for future electronic applications such as in thermal sensors or self-powered displays. More importantly, this research offers a unique solution to break the *PF* limit displayed by pristine InGaZnO thin films.

4.2. Experimental methods

4.2.1 Device Fabrication

The device fabrication process is depicted in Fig. 4.1. Bottom-gate top-contact TFTs were fabricated on p-type Si substrate gate electrode with 85 nm of thermally oxidized SiO_2 layer as the GI. The channel dimensions were L = 0.9 mm and W = 0.4 mm, as shown in the device structure in Fig. 4.2. First, 70 nm channel layer was deposited via radio-frequency magnetron sputtering of InGaZnO (In_2O_3:Ga_2O_3:ZnO = 2:2:1) at room temperature. The RF power and pressure during deposition were 100 W and 0.6 Pa, respectively. The channel layer was then patterned by conventional photolithographic techniques followed by wet etching with 0.02 M HCl solution. Next, a metal thin film layer (80 nm Ti/20 nm Au) was deposited via electron beam evaporation. Source and drain electrodes were subsequently formed by photolithography and lift-off. Finally, the fabricated devices were post-annealed at 300°C for 2h under air atmosphere (N_2:O_2 = 4:1).

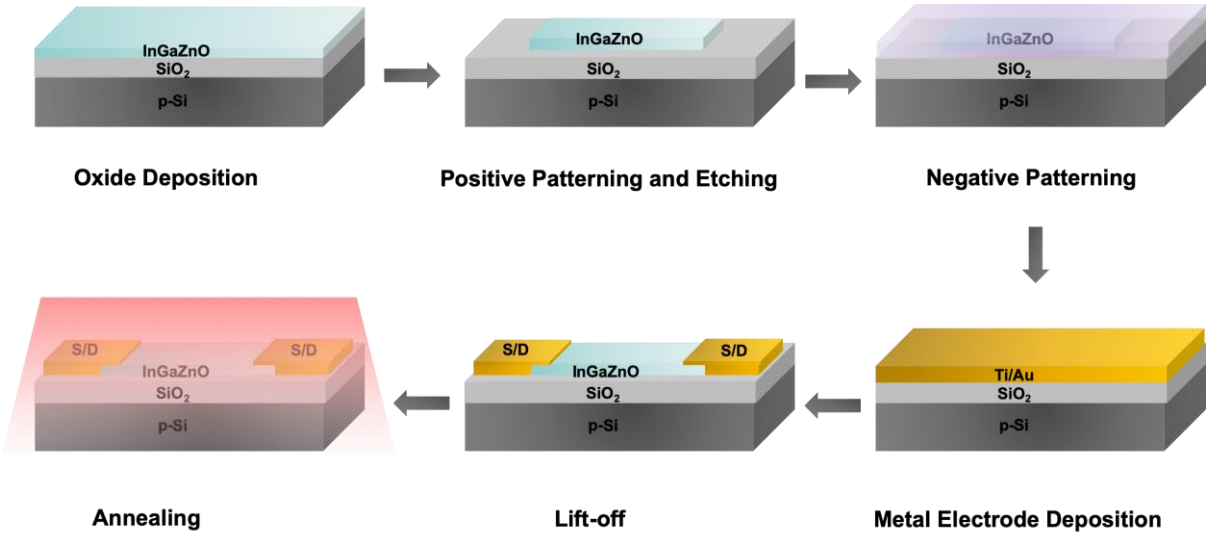

Fig. 4.1. Sample preparation procedure.

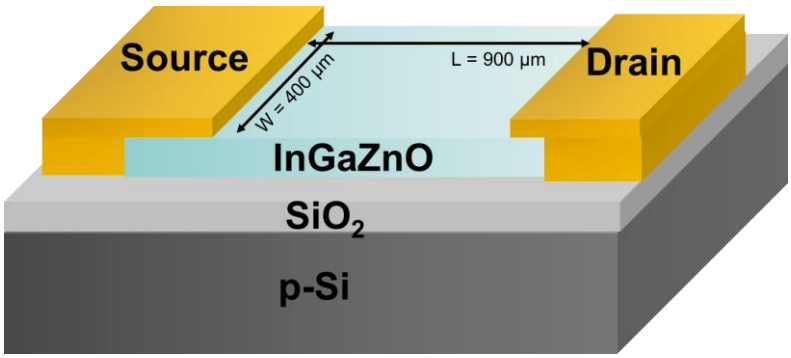

Fig. 4.2. Device structure of the a-InGaZnO TFT.

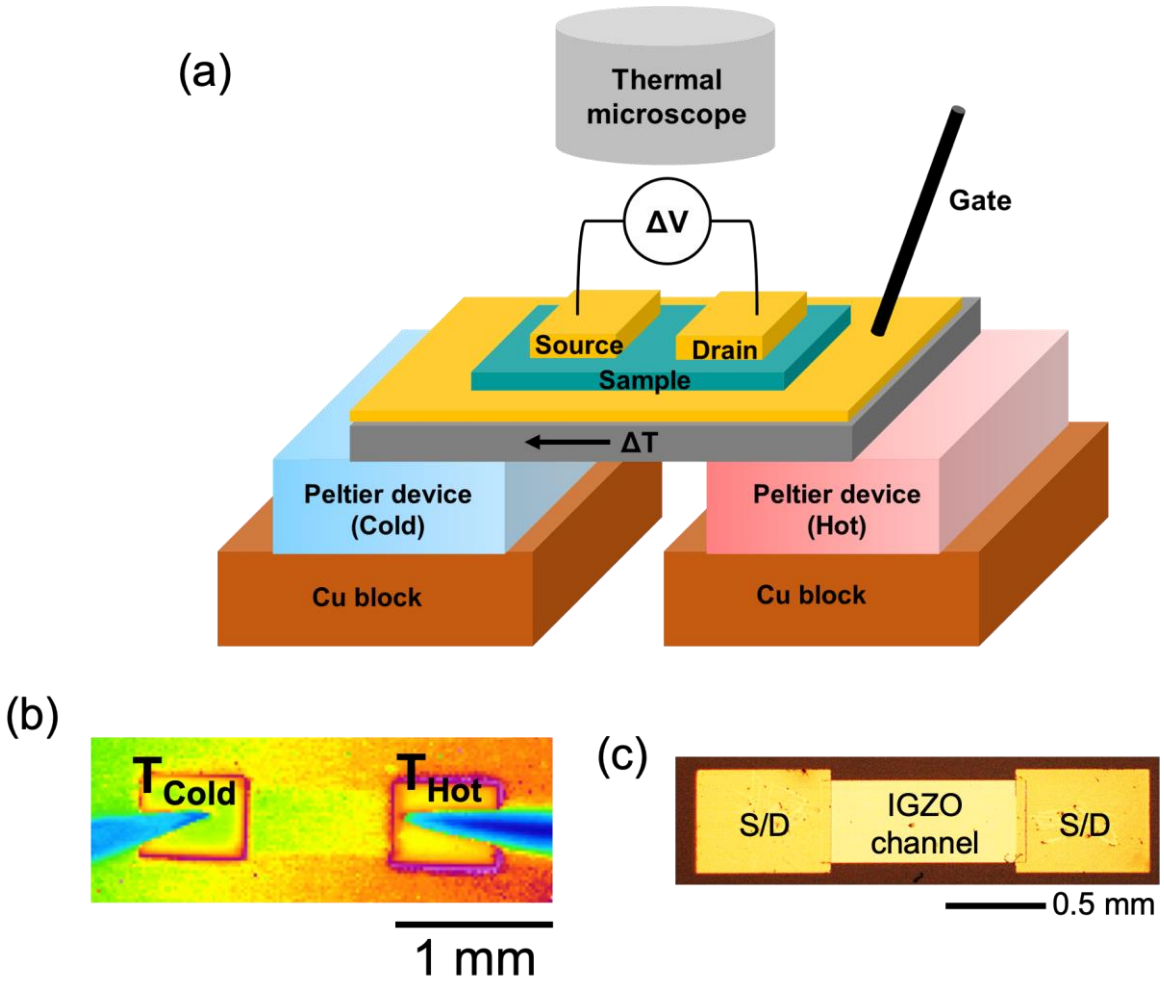

Fig. 4.3. (a) Seebeck measurement setup, (b) thermal map image and (c) optical microscope image of TFT device.

4.2.2 Electrical and Thermoelectric Properties Measurement

The transistor characteristics such as transfer (I_D-V_G) and output (I_D-V_D) curves were obtained using a semiconductor parameter analyzer (Agilent 4156C) at room temperature in dark condition. To determine the Seebeck coefficients, two Peltier devices were placed under the sample distanced 2 mm from each other to induce a temperature gradient between the source and drain electrodes (ΔT = 0-6 K). The ΔT was derived from thermal images obtained using an infrared thermal microscope (QFI) placed on top of the device (Fig. 4.3b). The optical image of the TFT device is shown in Fig. 4.3c. Since the device sample is bottom-gated, a Si substrate coated with Al/Au thin film was placed in between the Peltier devices and the sample to facilitate the V_G application. While varying the V_G, the thermoelectromotive force (ΔV) and ΔT were simultaneously monitored at room temperature. The ΔV is then plotted against ΔT, and the slope yields the Seebeck coefficient values.

4.2.3 Kamiya-Nomura Percolation Model

The Kamiya-Nomura model is based on the standard Boltzmann transport formalism using a percolation model [19]. This model, which has been used to explain the electron transport in both amorphous and crystalline InGaZnO, suggests that charge transport occurs in the conduction band wherein the densities of states (DOS) depends on the square root of energy [19-20]. Moreover, it assumes that a Gaussian distribution of potential barriers exist in the band, which can be ascribed to the structural randomness from the site sharing of Zn^{2+} and Ga^{3+} ions. These potential barriers hinder the electron conduction when the Fermi level (E_F) is situated in the tail-states, and can weaken the contribution of the carriers in low-energy states [8, 20]. A schematic diagram showing the potential barrier distribution as described by the

Kamiya-Nomura percolation model is shown in Fig. 4.4. This model has been numerically described by Adler, et. al [21]. The equations for σ and S are described as follows:

$$\sigma(T) = \int_{-\infty}^{\infty} \sigma_s \; p(E) \left(-\frac{\partial f_{FD}(E,T)}{\partial E} \right) dE \quad \text{(Eq. 1)}$$

$$S(T) = -\frac{1}{e\,T} \frac{\int_{-\infty}^{\infty} (E - E_f) \sigma_s p(E) \left(-\frac{\partial f_{FD}}{\partial \varepsilon} \right) dE}{\int_{-\infty}^{\infty} \sigma_s \, p(E) \left(-\frac{\partial f_{FD}}{\partial E} \right) dE} \quad \text{(Eq. 2)}$$

Meanwhile, the percolation factor *p(E)* accounts the effect of the potential barriers, and is defined as:

$$p(E) = \frac{1}{\pi E_0^2}^{1/2} \int_{E_c}^{E} e^{-(E\prime - \phi_0)^2 / 2\sigma_\phi^2} dE' \quad \text{(Eq. 3)}$$

where *e* is the elementary charge, *m** is the effective mass, E_c is the conduction band onset, τ is the relaxation time, *k* is the Boltzmann constant, v_z is the electron velocity, f_{FD} is the Fermi-Dirac distribution function, and D_c is the conduction band distribution of states (DOS). The relaxation time τ is defined as $\boldsymbol{\tau = \tau_0 exp(-W/kT)}$, while the $\boldsymbol{Dc(E) = Dc0\sqrt{E - E_c}}$. The *m** value used is $0.35m_e$, following the typical value used for InGaZnO [10]. The Φ and σ represent the average and distribution widths of the potential barriers, respectively. The σ and *S* were fitted over varying Φ (0.005 – 0.3 eV) and σ (0.04 – 0.2 eV) values at a fixed τ = 1.39 fs.

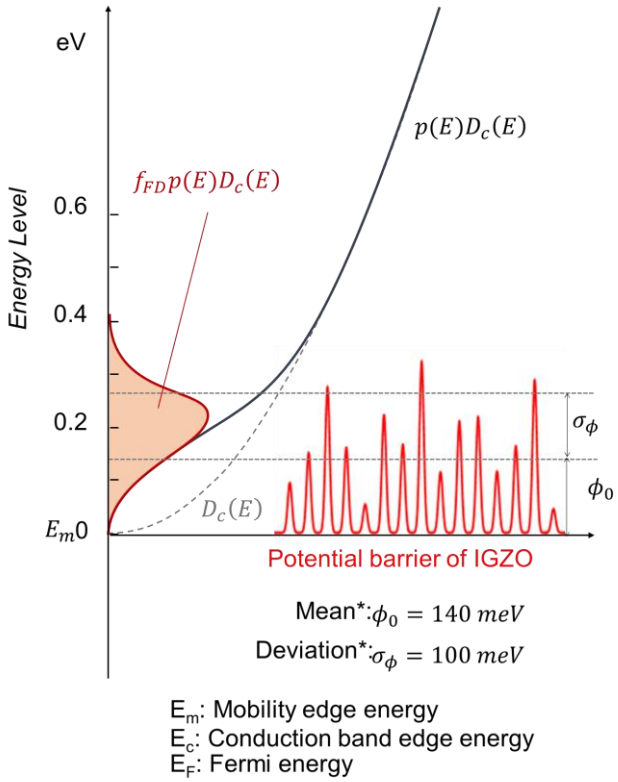

Fig. 4.4. Model of the potential barrier distribution in the IGZO conduction band.

4.3. Results and Discussion

The transistor characteristics of the fabricated InGaZnO TFT are shown in Fig. 4.5. The transfer curve obtained from V_G = -20 to 20 V in Fig. 4.5a exhibit proper switching for all drain voltage (V_D) values applied. This suggests typical transistor behavior, even at a low V_D of 100μV, where the Seebeck voltage is expected to range. Transistor properties such as mobility, threshold voltage, gate current and current on-off ratio are summarized in Table 4.1. The mobility was calculated from the linear region of the V_D = 0.1V plot using the ff. equation:

$$\mu = g_m \frac{L}{WC_{ox}V_{DS}} \quad \text{(Eq. 4)}$$

where g_m is the measured transconductance and C_{ox} is the capacitance of SiO_2. The maximum mobility obtained was 10.4 $cmV^{-1}S^{-1}$, which is in complete agreement with published literature [2]. Although the size of the device used in this study is significantly larger than typical TFTs, the dimensional aspect ratio (L/W) is high enough to compensate for its lower g_m, yielding a similar mobility value. Likewise, the other TFT characteristics lie within a similar range as those previously reported [22-23]. The TFT output curves are graphed in Fig. 4.5b, which reveals a clear pinch-off and saturation behavior, which means the InGaZnO TFT adheres to the standard transistor theory.

Table 4.1. Transistor characteristics of the InGaZnO TFT devices.

Mobility ($cmV^{-1}S^{-1}$)	Threshold Voltage (V)	Gate Current (A)	I_{on}/I_{off} ratio
10.4 ± 0.25	0.53 ± 0.058	~10^{-12}	~10^6

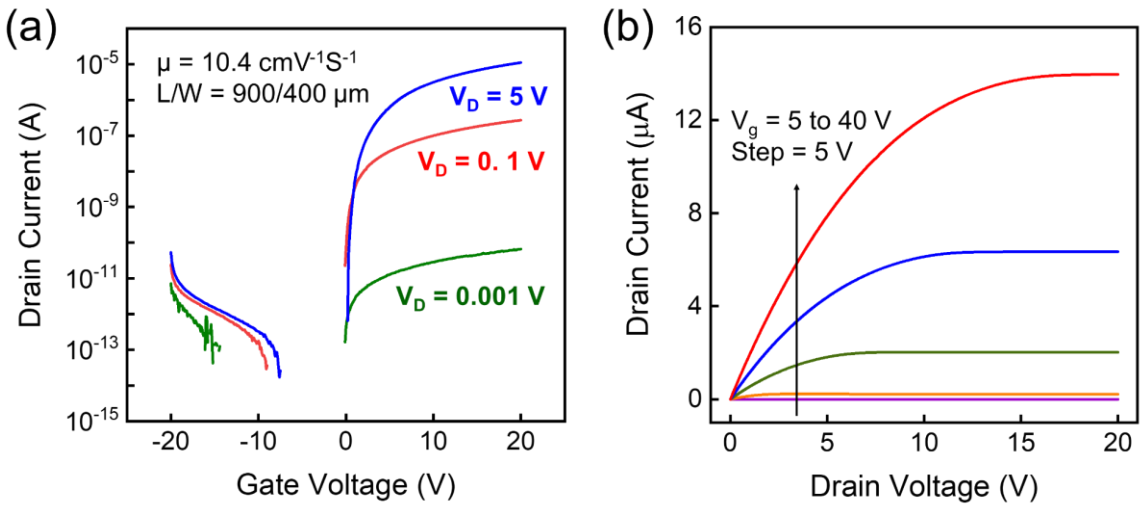

Fig. 4.5. (a) transfer curve and (b) output curve of the bottom-gate InGaZnO TFT.

In order to investigate the thermoelectric properties of the InGaZnO TFT device, the σ was calculated using resistance (R) extracted from the I_D-V_D curves under varying V_G from -20 to 40 V. The thickness dimension to be considered, however, is expected to change depending on the applied V_G. To obtain this, the n was calculated relative to the distance from the GI/channel interface along the InGaZnO depth following the depletion approximation [24]. The equation below is used, as in the study by Kiguchi et. al [25]:

$$n = \frac{\varepsilon_{ox} V_G}{t_{ox} e d} \quad \text{(Eq. 5)}$$

where ε_{ox}, t_{ox}, e and d are the SiO_2 dielectric constant, SiO_2 thickness, and InGaZnO distance from the GI/channel interface, respectively. First, the relationships between n and distance were plotted from 0 to 70 nm under varying V_G from 0 to 40 V (Fig. 4.6a). It is noteworthy that n under negative V_G is difficult to estimate since a carrier accumulation layer is not expected to have formed. It can be observed in Fig. 4.6a that the n generally shows an increasing behavior as V_G changes from 0 to 40 V. As shown in Fig. 4.6a, n appears to saturate at less than 10 nm, which signifies the presence of a highly conductive region where the charge

carriers accumulate. The distance at which $n = n_0/e$, where n_0 is the projected carrier concentration exactly at the interface, was then identified as the accumulation layer thickness (t_{acc}). The extracted t_{acc} was around 1.275 nm. Using the estimated t_{acc}, the σ values were then calculated at the positive V_G range. For the $V_G = 0$ and $V_G < 0$ regions, the thickness used is the film thickness (70 nm), due to the assumption that an accumulation layer is absent. As evidently demonstrated in Fig. 4.6b, σ barely changes at negative V_G, and then exponentially increases when a positive V_G is applied. This can mostly be attributed to a huge decline in R as the applied positive V_G increases, which also represents the turning on of the transistor.

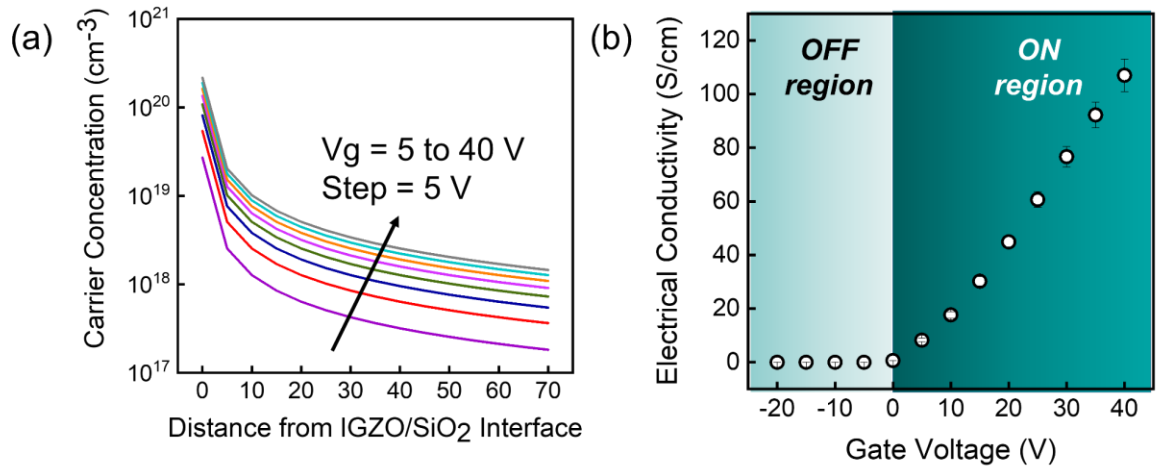

Fig. 4.6. (a) Carrier concentration vs thin film thickness approximation, and (b) electrical conductivity vs gate voltage.

To further explain the conduction mechanism, a schematic diagram of the conduction band following the well-established typical transistor behavior is portrayed in Fig. 4.7 [24]. At $V_G = 0$, the electrons are resting randomly across the bulk InGaZnO depth. When a positive V_G is applied, the conduction band bends downward at the SiO_2 surface, causing the E_F to locate above the conduction band minimum (CBM). As a result, electrons are forced to accumulate at the SiO_2/InGaZnO interface. Further increasing the applied V_G would probably result in a

more severe downward conduction bending, leading to having a higher density of electron accumulation at the GI/channel interface. At V_G < 0, the conduction band bends upward, retaining the E_F below the CBM. Consequently, the electrons are driven away from the interface, forming a depletion layer near the GI/channel interface. Further increasing the negative applied V_G would less likely to have caused a charge accumulation, since the electrons are free to move anywhere in the bulk region, instead of being narrowly confined near the interface as in the case of positive applied V_G.

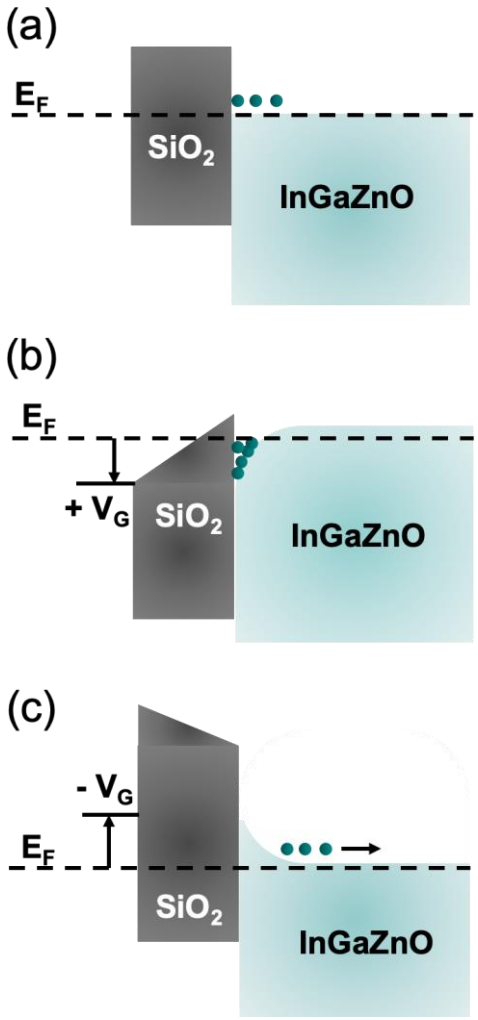

Fig. 4.7. Conduction mechanism for (a) V_G = 0, (b) V_G > 0 and (c) V_G < 0.

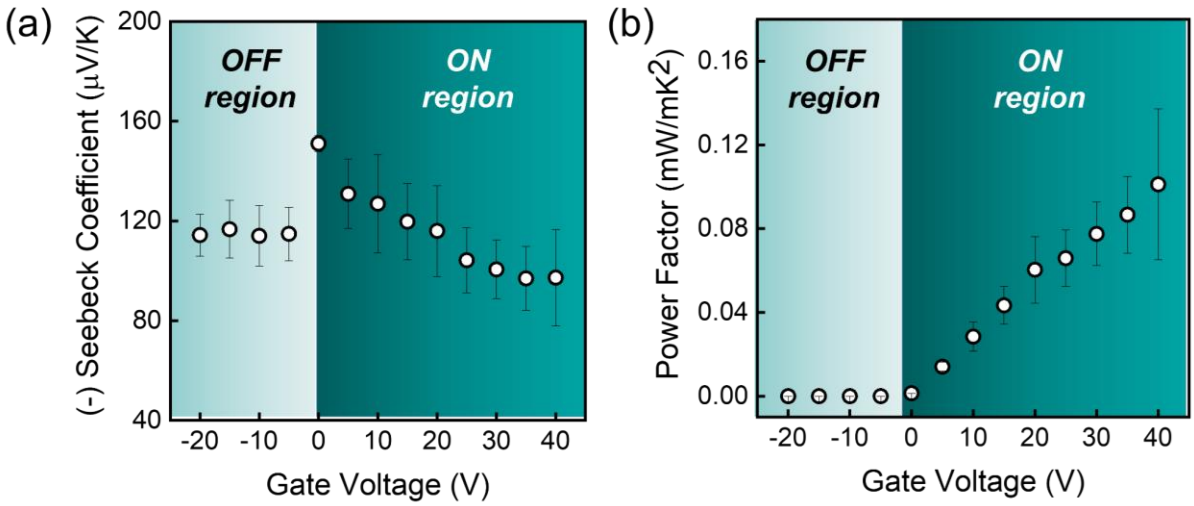

Fig. 4.8. (a) Seebeck coefficient vs gate voltage, and (b) power factor vs gate voltage.

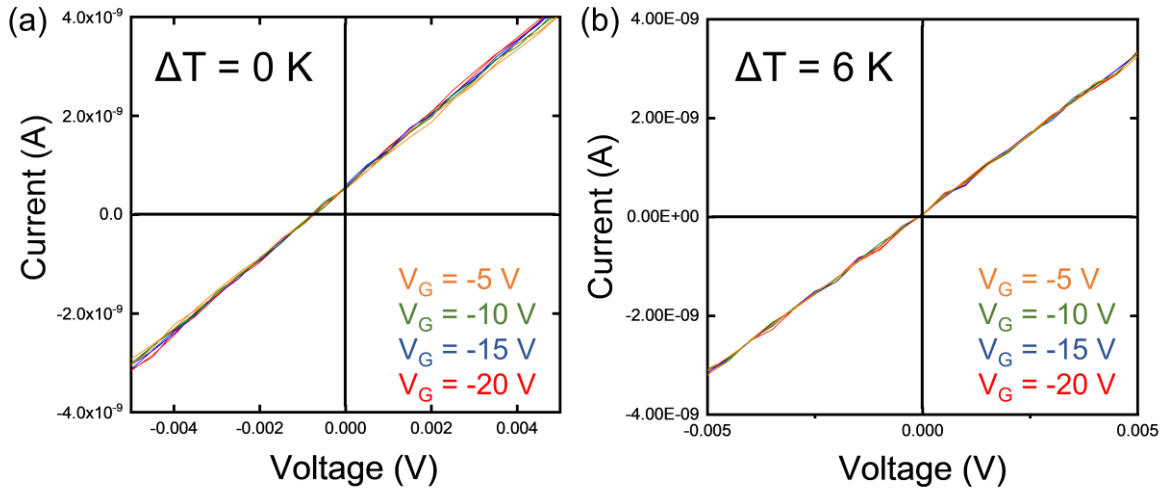

Fig. 4.9. I-V curves of TFT under varying negative VG applied, with source and drain thermal gradients of (a) 0 K, and (b) 6 K.

The Seebeck coefficient values, on the other hand, displayed a different trend when the applied V_G is changed. Fig. 4.8a shows the effect of V_G on the Seebeck coefficient of the InGaZnO TFT device. When the transistor is OFF (V_G < 0), the values appeared generally lower compared to those in V_G = 0 to 20 V. Theoretically, the Seebeck values at negative applied V_G should display higher values compared to those in the positive V_G range because

the *n* is expected to be way lower due to the absence of an accumulation layer. In the case of this study, the values appear lower than expected, which can be attributed to the fact that the ΔT measurement is performed from above the sample, which is much closer to the bulk surface than the GI/channel interface. The increase in *n* at the bulk, caused by the depletion region pushing the electrons deeper into the InGaZnO, could have also been detected, probably causing an overestimation of the ΔT. Nevertheless, the linear behavior of the I-V curves (Fig. 4.9) both with and without a thermal gradient implies that the analyzer can detect the values in the OFF region. In addition, the current lies within the nanoampere range, which is well above the system resolution of ~1 fA. The important point is that a non-dependence of *S* in the V_G at $V_G < 0$ clearly manifests. Although the total *n* is likely similar to those at $V_G > 0$, the thermoelectrically active region to be considered is the entire film thickness (70 nm). At $V_G = 0$, an accumulation layer is still expected to be absent, but an increase in *S* can be observed. This can probably arise from the fact that unlike in the $V_G < 0$ region, a depletion layer does not form, so an overestimation of the ΔT could not have occurred. When the transistor turns on ($V_G > 0$), Seebeck coefficients exhibit a slightly decreasing trend from around 151.06 to 97.9 uV/K when V_G is modulated from 0 to 40 V. This is expected owing to the inverse relationship of *S* with *n*, which increases with a higher applied positive V_G, as previously discussed.

However, it is interesting that the decrease in *S* is not very severe despite the great enhancement in electrical conductivity. In order to explain this, the thermal deBroglie wavelength λ_D is calculated using the ff. equation:

$$\lambda_D = \frac{h}{\sqrt{3m^* k_b T}} \quad \text{(Eq. 6)}$$

where *h* and k_b are the Plank's and Boltzmann's constants, respectively, *T* is the temperature and m^* is the effective mass, which is approximated to be $0.35m_e$ for amorphous InGaZnO [8]. The calculated λ_D is 10.6 nm, which is larger compared to the calculated t_{acc}. As established in

previous research, a quantum well thinner than λ_D would result to an enhanced S due to modification in the density of states near the conduction band edge when the electrons are confined in the narrow quantum well [18, 26]. In this case, the S-σ coupling that is observed in most thin film systems is likely weakened in the case of the InGaZnO TFT because of the extremely narrow thermoelectrically active region.

The effect of V_G on the power factor, which was calculated from the equation $PF = S^2\sigma$, is shown in Fig. 4.8b. An exponentially increasing trend can be observed similar to the V_G-σ relationship in Fig. 4.6b. Although S should induce a greater effect on PF as dictated by the equation, the small variation in S with V_G is strongly overpowered by the exponential increase in σ. It can therefore be established that the significant improvement in PF by V_G modulation can be achieved primarily owing to the formation of the accumulation layer at the GI/channel interface, which extremely narrows down the thermoelectrically active region. Interestingly, the thermoelectric properties are also in effect "turned on" when the transistor is on. This implies that the TFT can potentially simultaneously act as an effective thermoelectric device in its on state, provided that there is an effective thermal gradient between the source and drain.

The theoretical behavior of S and σ based on the Kamiya-Nomura percolation model is also illustrated in Fig. 4.10a. The theoretical values, shown as light blue lines, were obtained by varying the σ and Φ parameters of the percolation factor while maintaining a constant τ. Also plotted are experimental data on a-InGaZnO from past literature [8, 27], the c-InGaZnO samples discussed in Chapter 3 [7], and the InGaZnO TFT. As shown, all experimental results corroborate well with the theoretical model. However, as more clearly illustrated in Fig. 4.10b, the experimental results for thin films and TFT can be fitted under different percolation factor parameters. This suggests that there is a difference in the shape of the potential barriers between the two material systems. As mentioned earlier, the Φ and σ parameters signify the average

and distribution widths of the potential barriers, respectively. The TFT exhibited a larger Φ and smaller σ compared to thin films, which suggest that the potential barriers are composed of taller and more uniform peaks. This could have been caused by a phenomenon called energy filtering. In this phenomenon, the low energy electrons are filtered out, which means that the high energy electrons are solely responsible for the conduction transport. As an effect, the Seebeck coefficient is allowed to increase without compromising the high electrical conductivity [28]. In this case, the S-σ coupling can be said to be successfully suppressed.

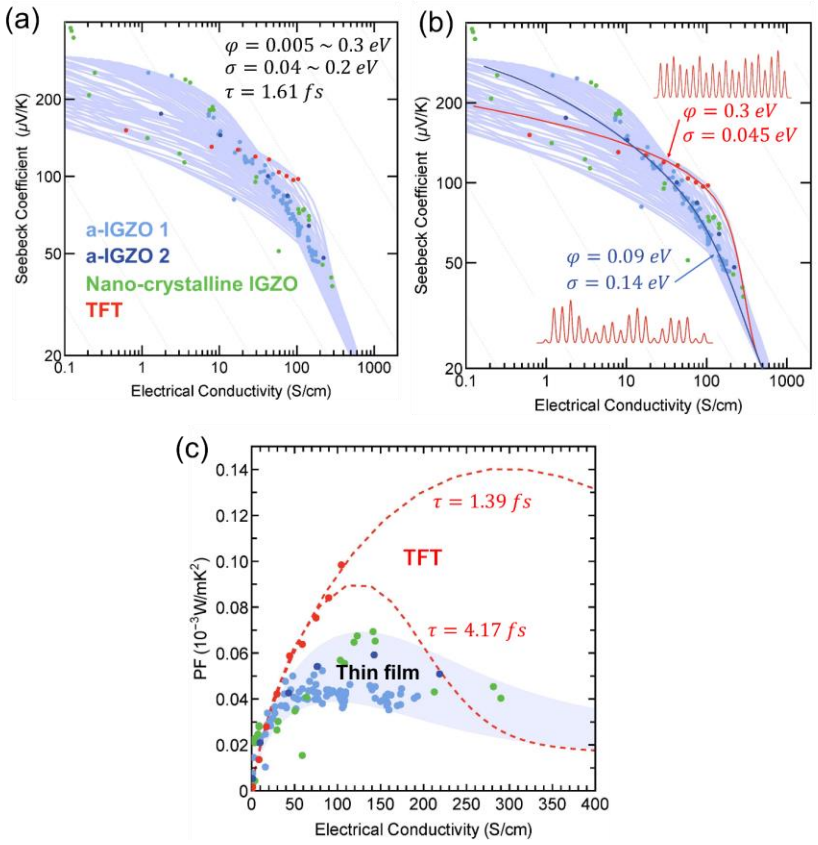

Fig. 4.10. (a) S vs σ plot and (b) PF vs σ plots showing both experimental and theoretical results.

The theoretical PF vs σ is then shown in Fig. 4.10c. As the plot clearly indicates, under the same τ = 1.39 fs, the TFT appears to reach higher PF values compared to the pristine thin films. The maximum PF achieved by the TFT is about 42% higher than that of thin films. This can be attributed to the suppression of the S-σ coupling caused by the energy filtering. In addition, the TFT can still be fitted at a higher τ, wherein a maximum of ~0.15 mW/mK^2 can be reached at a conductivity of ~400 S/cm when τ = 4.37 fs. The energy filtering could have been caused by quantum confinement arising from the extremely narrow thermoelectrically active region [28-29].

Finally, it is important to investigate how the thermal gradient application affects the TFT chracteristics. Fig. 4.11 depicts the effect of increasing ΔT on the I_D-V_G curves measured at V_D = 0.1 V. Evidently, the threshold voltage (V_{TH}) slightly negatively shifts when ΔT is increased from 0 to 6 K. This means that at higher ΔT, the TFT is switching on earlier than intended. This could have been caused by the free electrons from the channel band gap that were thermally-activated [30]. These thermally-activated free electrons may be released from the trap sites to below the conduction band. Moreover, high temperature exposure may create additional free carriers from oxygen vacancies that may have been induced by thermal excitation. Under an even higher temperature operation, the negative V_{TH} shift of an InGaZnO/SiO_2 TFT can be as high as 6.9 V at an operation temperature of 353 K [30]. This suggests that the TE-TFT could operate well at the near room temperature range, but may begin to display degrading transistor characteristics at a higher temperature. Furthermore, the I_{ON}/I_{OFF} ratios (inset) were slightly decreasing with the ΔT, but is not large enough to interfere with the switching performance.

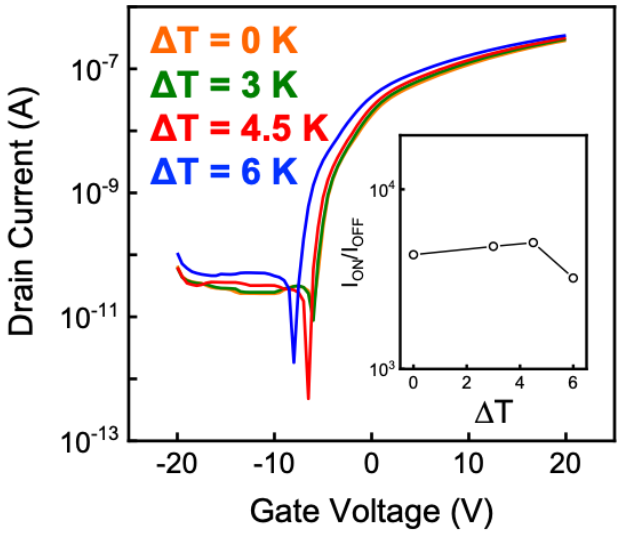

Fig. 4.11. I_D-V_G plots under varying ΔT (0 – 6 K). I_{ON}/I_{OFF} ratio vs ΔT graph is shown as inset.

4.4. Summary

Herein, the thermoelectric properties of a typical InGaZnO/SiO_2 TFT with SiO_2 GI at the GI/channel interface was significantly improved by V_G modulation. When the transistor is on (V_G > 0 is applied), the thermoelectric *PF* increased by up to three orders of magnitude owing to the formation of an electron accumulation layer at the GI/channel interface, which served as an extremely narrow thermoelectrically active region. The Seebeck coefficient, on the other hand, only slightly decreased as a response to the positive V_G, allowing the *PF* to reach >0.1 mW/mK^2. When the transistor is off, the thermoelectric properties are also extremely low. Therefore, if the temperature difference between the source and drain is significantly high, the InGaZnO TFT can simultaneously act as a thermoelectric device. Finally, the Kamiya-Nomura percolation model was used to compare the InGaZnO TFT and pristine thin films. It was observed that all experimental results fit well with the percolation model, but the TFT showed a weaker *S* dependence of *PF* compared to the thin films. The model was also able to estimate a higher maximum *PF* for the TFT compared to the thin film under the same τ, but it can also be fitted using a higher τ to yield a *PF* of up to ~0.15 mW/mK^2, almost twice that of typical pristine thin films.

References

1) K. Nomura, H. Ohta, A. Takagi, T. Kamiya, M. Hirano and H. Hosono, Nature, 432, 488–492 (2004).

2) H. Hosono, Nature Electronics, 1, 428, (2018).

3) Y. Zhao, Z. Wang, G. Xu, L. Cai, T. Han, A. Zhang, Q. Wu, R. Wang, T. Huang, P. Cheng, S. Chang, D. Bao, Z. Zhao, M. Wang, Y. Huang, and Y. Yang, Adv. Funct. Mater. 30, 2003285, 2020.

4) H. Zan, C. Yeh, H. Meng, C. Tsai and L. Chen, Adv. Mater. 24, 3509-3514, 2012.

5) Y. Rim, H. Chen, X. Kou, H. Duan, H. Zhou, M. Cai, H. Kim and Y. Yang, Adv. Mater. 26, 4273-4278, 2014.

6) H. Goldsmid, Introduction to Thermoelectricity, 2nd Ed., Springer-Verlag Berlin Heidelberg, 2010.

7) J. Felizco, M. Uenuma, Y. Ishikawa and Y. Uraoka, Appl. Surf. Sci. 527, 14679, 2020.

8) Y. Fujimoto, M. Uenuma, Y. Ishikawa, and Y. Uraoka, AIP Adv. 5, 097209, 2015.

9) N. Nguyen, T. Nguyen, Y. Liu, M. Aminzare, A. Pham, S. Cho, D. Wong, K. Chen, T. Seetawan, N. Pham, H. Ta, V. Tran, and T. Phan, ACS Appl. Mater. Inter. 8, 49, 33916–33923, 2016.

10) H. Ohta, R. Huang and Y. Ikuhara, Phys. Stat. Sol. (RRL) 3, 105-107, 2008.

11) D. Seo, S. Shin, H. Cho, B. Kong, D. Whang, H. Cho, Acta Materialia 59, 6743–6750, 2011.

12) S. Andrews, M. Fardy, M. Moore, S. Aloni, M. Zhang, V. Radmilovic and P. Yang, Chem. Sci. Chem. Sci. 2, 706, 2011.

13) M. S. Dresselhaus, Y. M. Lin, T. Koga, S. B. Cronin, O. Rabin, M. R. Black and G.

Dresselhaus, Low dimensional thermoelectricity, in: T. M. Tritt (Ed.), Semiconductors and Semimetals: Recent Trends in Thermoelectric Materials Research III, V, 71, Academic Press, San Diego, CA, 2001.

14) A. Boukai, Y. Bunimovich, J. Tahir-Kheli, J. Yu, W. Goddard and J. Heath, Nature 451, 168–171, 2008.

15) D. Liang, Y. Zhang, H. Cho and H. Ohta, Appl. Phys. Lett. 116, 143503, 2020.

16) S. Shimizu, M. Bahramy, T. Iizuka, S. Ono, K. Miwa, Y. Tokura and Y. Iwasa, PNAS 113, 23, 2016.

17) H. Ohta, S. Kim, S. Kaneki, A. Yamamoto, and T. Hashizume, Adv. Sci. 5, 1700696, 2018.

18) H. Ohta, T. Mizuno, S. Zheng, T. Kato, Y. Ikuhara, K. Abe, H. Kumomi, K. Nomura and H. Hosono, Adv. Mater. 24, 740-744, 2012.

19) T. Kamiya, K. Nomura and H. Hosono, Appl. Phys. Lett. 96, 122103, 2010.

20) W. Germs, W. Adriaans, A. Tripathi, W. Roelofs, B. Cobb, R. Janssen, G. Gelinck, and M. Kemerink, Phys. Rev. B 86, 155319, 2012.

21) D. Adler, L. Flora, and S. Senturia, Solid State Commun. 12, 9-12, 1973.

22) D. Corsino, J. Bermundo, M. Fujii, K. Takahashi, Y. Ishikawa and Y. Uraoka, Appl. Phys. Express 11, 061103, 2018.

23) J. Jeon, J. Um, S. Lee, and J. Jang, AIP Advances 7, 125110, 2017.

24) S. Sze and M. Lee, Semiconductor Devices, 3rd Ed. John Wiley & Sons, Inc. New York, 2012.

25) M. Kiguchi, M. Nakayama, K. Fujiwara, K. Ueno, T. Shimada and K. Saiki, Jpn. J. Appl. Phys. 42, L1408, 2003.

26) H. Ohta, S. Kim, Y. Mune, T. Mizoguchi, K. Nomura, S. Ohta, T. Nomura, Y. Nakanishi, Y. Ikuhara, M. Hirano, H. Hosono and K. Koumoto, Nature Mater. 6, 129–134, 2007.

27) D. Senaha, “Effect of potential barrier in the a-InGaZnO thin film on the thermoelectric properties”, MS Thesis, Nara Institute of Science and Technology, Japan, 2018.

28) D. Narducci, E. Selezneva, G. Cerofolini, S. Frabboni and G. Ottaviani, J. Sol. State Chem. 193, 19-25, 2012.

29) M. Dresselhaus, G. Chen, M. Tang, R. Yang, H. Lee, D. Wang, Z. Ren, J. Fleurial and P. Gogna, Adv. Mater. 19, 8, 2007.

30) S. Yoon, N. Seong, K. Choi, W. Shin and S. Yoon, RSC Adv. 8, 25014, 2018.

Chapter 5. Summary and Future Work

5.1. Summary

This dissertation proposed several approaches to improve the thermoelectric power factor of ZnO-related thin film materials. Specifically, controlling the carrier concentration and crystal structure of the thin films are suggested as effective solutions. Carrier concentration can be optimized by (1) introducing additional carriers via annealing such as hydrogen or oxygen vacancies, (2) inserting dopant layers within the film, and (3) integrating in a thin film transistor to confine electrons in an extremely narrow thermoelectrically active region. Additionally, shifting the thin film orientation along the c-axis enhances the structural stability leading to improved electron transport.

The main results of this dissertation are summarized as follows:

Chapter 2 proposed the introduction of HfO_2 and TiO_2 layers within an atomic layer deposited ZnO thin film. It was observed that TiO_2/ZnO thin films displayed twice the value of carrier concentration compared to pure ZnO, which results to a significantly enhanced electrical conductivity. HfO_2/ZnO, on the other hand, exhibited superior thermal stability owing to an apparent shift of crystal orientation in ZnO due to the introduction of Hf atoms. After one thermal cycle, both doped ZnO films showed superior PF compared to pure ZnO because the properties of ZnO appears to degrade when subjected to heat, likely arising from defect formation.

In Chapter 3, the effect of hydrogen in the annealing atmosphere on the thermoelectric performance of c-axis aligned crystalline and crystal-embedded c-axis aligned crystalline InGaZnO was investigated. For amorphous InGaZnO, pure N_2 annealing exhibited the highest

PF compared to the ones annealed with a small amount of H_2 owing to the easy formation of oxygen-related defects, which are sources of additional charge carriers. However, it was determined that for the crystalline InGaZnO, the supplemental effect of introducing hydrogen aided in increasing the amount of charge carriers in the film. The crystalline film is likely hindering the easy formation of oxygen-related defects, unlike in the case of amorphous InGaZnO.

Chapter 4 reported that gate voltage modulation in a typical InGaZnO/SiO_2 thin film transistor greatly impacted the PF at the interface. During the transistor ON state ($V_G > 0$) is applied), a tremendous increase in electrical conductivity was observed. This can be attributed to the formation of a charge accumulation layer at the InGaZnO/SiO_2 interface, which significantly narrowed down the thermoelectrically active region. On the other hand, the positive gate voltage modulation introduced only a small decreasing effect on the Seebeck coefficient, which signifies that its coupling effect with σ is successfully suppressed. This led to an increase in the PF amounting to three orders of magnitude. During the transistor OFF state ($V_G < 0$), negligible thermoelectricity was observed. Additionally, modelling the results using the Kamiya-Nomura percolation theory suggests that the InGaZnO TFT can exhibit a PF up to twice the maximum PF of pristine thin films. It can therefore be established that the provided there is a thermal gradient between the source and drain, the InGaZnO/SiO_2 TFT can also simultaneously function as a thermoelectric generator.

5.2. Suggestions for Future Work

5.2.1. Atomic Layer Deposition of New Novel Dopants

As reported in Chapter 2, inserting novel oxide layers within ZnO by atomic layer deposition is a very effective technique in improving the thermoelectric performance and stability. However, only a few ZnO dopants have been utilized for thermoelectric applications at this point. Therefore, it would be interesting to explore other elements as they may not only increase the PF but also bring out unique, interesting properties. Wu, et. al. fabricated an alternating multilayered ZnO/SiO_2 thin film via sputtering, which exhibits a $zT \sim 0.16$ at room temperature [1]. Ce and Dy, on the other hand, were also explored as potential ZnO dopants but their power factors remained inferior [2]. Elements belonging to the lanthanide series are relatively rarely explored ZnO dopants, and would be interesting to study.

In addition, co-doping different elements could potentially lead to synergistic effects. For example, co-doping Ti and Hf onto ZnO may lead to combining the merits of both dopants – high electrical conductivity for Ti and high electrical and thermal stability of Hf. It would be easy to start with Al, since it is a well-established ZnO dopant and widely available as precursor for ALD, then pair it with a less-explored dopant.

5.2.2. Thermoelectric Properties of Nanostructured ZnO-related Materials

It was discussed in Chapter 1 that successful decoupling of S and σ can be achieved by quantum confinement in low dimensional systems. Such low-dimensional systems could come in several nanostructured forms – 0D structures such as quantum dots, 1D such as nanowires or 2D such as 2D electron gas or quantum wells. Nanostructures based on ZnO-related

materials can be utilized for increasing the *PF*. For example, Yang, et. al. synthesized Sb-doped ZnO nanobelts that can generate 1.94 nW power [3]. In a study by Andrews, et. al, $In_{2-x}Ga_xO_3(ZnO)_n$ polytypoid nanowires were fabricated by growing ZnO nanowires followed by coating with In and Ga via solid-state diffusion [4]. The resulting nanowires exhibited a superlattice structure, which led to a power factor of up to 0.6 mW/mK^2. However, there are very few studies on the thermoelectric properties of InGaZnO nanowires, and almost none have used other high surface area nanostructures such as nanotubes, nanorods, nanoparticles or quantum dots.

5.2.3. Alternating Superlattice Structure

Ohta, et. al. has demonstrated a large enhancement in the Seebeck coefficient in an a-InZnO/a-InGaZnO superlattice system [5]. The InZnO layers act as the well while the InGaZnO layers acts as the barriers, which have thicknesses of 1nm and 6.6 nm, respectively. A four-fold increase in the Seebeck coefficient while maintaining the electrical conductivity was observed, which implies a decoupling of the properties brough about by the quantum confinement effect. For future studies, other amorphous oxides may be used, as long as the thicknesses were maintained well below their respective deBroglie wavelengths. The layers of the superlattice structure need not be limited to amorphous oxides. For example, Karttunen, et. al. demonstrated a flexible ZnO-organic superlattice structure deposited onto cotton substrates [6].

References

1) H. Wu, Y. Su, C. Pao and C. Shih, ACS Appl. Mater. Interfaces 11, 14, 13507–13513, 2019.
2) K. Park, H. Hwang, J. Seo and W. Seo, Energy 54, 139-145, 2013.
3) Y. Yang, K. Pradel, Q. Jing, J. Wu, F. Zhang, Y. Zhou, Y. Zhang and Z. Wang, ACS Nano 6, 8, 6984–6989, 2012.
4) S. Andrews, M. Fardy, M. Moore, S. Aloni, M. Zhang, V. Radmilovic and P. Yang, Chem. Sci. 2, 706-714, 2011.
5) H. Ohta, R. Huang and Y. Ikuhara, Phys. Stat. Solid. (RRL) 2, 3, 2008.
6) A. Karttunen, L. Sarnes, R. Townsend, J. Mikkonen and M. Karppinen, Adv. Electron. Mater. 3, 1600459, 2017.

Research Achievements

List of Publications

1. **J. C. Felizco**, T. Juntunen, M. Uenuma, J. Etula, C. Tossi, Y. Ishikawa, Y. Uraoka
2. , "Enhanced Thermoelectric Transport and Stability in Atomic Layer Deposited HfO/ZnO and TiO/ZnO Sandwiched Multilayer Thin Films", *ACS Appl. Mater. Inter.* **12**, 43, 49210–49218 (2020).

3. **J. C. Felizco**, M. Uenuma, Y. Ishikawa, Y. Uraoka, "Optimizing the Thermoelectric Performance of InGaZnO Thin Films Depending on Crystallinity via Hydrogen Incorporation", *Appl. Surf. Sci.* **527**, 146791 (2020).

4. **J. C. Felizco**, M. Uenuma, M. Fujii, Y. Uraoka, "Thermopower Tuning at the InGaZnO/SiO_2 Heterointerface via Gate Bias Modulation" *(In Preparation)*

Related Publications

1. **J. C. Felizco**, M. Uenuma, D. Senaha, Y. Ishikawa, Y. Uraoka, "Growth of InGaZnO nanowires via a Mo/Au catalyst from amorphous thin film", *Appl. Phys. Lett.* **111**, 033104 (2017).

2. M. Uenuma, K. Umeda, **J. C. Felizco**, D. Senaha, Y. Uraoka, H. Adachi, "Flexible TEG Using Amorphous InGaZnO Thin Film", *J. Elec. Mater.* **48**, 4, 1971-1975 (2019).

Research Grants

1. Grant-in-Aid for PhD Students (450K ¥) – Nara Institute of Science and Technology, 2018.

2. Marubun Research Promotion Foundation International Exchange Grant (150K ¥) – 5th Nano Today Conference, Hawaii, USA, Dec. 6-10, 2017.

International Conferences

1. **J. C. Felizco,** M. Uenuma, J. Bermundo, D. Corsino, H. Ikenoue, and Y. Uraoka, "Excimer Laser Irradiation of Amorphous IGZO Thin Films for Thermoelectric Device Applications", *Virtual Conference on Thermoelectrics,* July 21-23, 2020. (Poster Presentation)

2. **J. C. Felizco**, T. Juntunen, M. Uenuma, J. Etula, C. Tossi, Y. Ishikawa, Y. Uraoka, "Atomic Layer Deposition of Hf-Doped ZnO Thin Films with Enhanced Thermoelectric Properties", *2019 Materials Research Society Fall Meeting and Exhibit*, Boston, Massachussetts, USA, Dec. 1-6, 2019. (Oral Presentation)

3. **J. C. Felizco**, M. Uenuma, H. Murakawa, Y. Ishikawa, and Y. Uraoka, "Inducing Thermoelectricity in C-axis Aligned Crystalline InGaZnO Thin Film via Hydrogen Annealing", *International Conference on Solid State Devices and Materials 2019*, Nagoya University, Nagoya, Japan, Sep. 2-5, 2019. (Poster Presentation)

4. **J. C. Felizco**, M. Uenuma, K. Umeda, Y. Ishikawa, Y. Uraoka, "Single Crystalline InGaZnO Nanowires for Potential Thermoelectric Applications", *37th International Conference on Thermoelectrics*, Congress Center, Caen, France, July 1-5, 2018. (Poster Presentation)

5. **J. C. Felizco**, M. Uenuma, D. Senaha, Y. Ishikawa, Y. Uraoka, "Bimetal-catalyzed formation of InGaZnO nanowires from amorphous thin film", *5th Nano Today Conference*, Hawaii, USA, Dec. 6-10, 2017. (Poster Presentation)

6. **J. C. Felizco**, M. Uenuma, D. Senaha, Y. Ishikawa, Y. Uraoka, "Bimetal-catalyzed VLS growth of InGaZnO nanowire from amorphous thin film", *24th International Workshop on Active-Matrix Flatpanel Displays and Devices (AM-FPD 2017)*, Kyoto, Japan, July 4-7, 2017. (Oral Presentation)

Domestic Conferences

1. **J. C. Felizco**, T. Juntunen, M. Uenuma, J. Etula, C. Tossi, Y. Ishikawa, Y. Uraoka, "Thermoelectric Transport in Atomic Layer Deposited Hf and Ti-doped ZnO Thin Films", *The 80th JSAP Autumn Meeting*, Hokkaido University, Hokkaido, Sep. 18-21, 2019. (Oral Presentation)

2. **J. C. Felizco**, M. Uenuma, K. Umeda, Y. Ishikawa, Y. Uraoka, "Thermoelectric Properties of Bimetal-catalyzed InGaO3(ZnO)4 Nanowire", *79th JSAP Autumn Meeting*, Nagoya Congress Center, Nagoya, Sep. 18-21, 2018. (Poster Presentation)

3. **J. C. Felizco**, M. Uenuma, D. Senaha, Y. Ishikawa, Y. Uraoka, "Effect of Au thickness on the Bimetal-catalyzed Growth of InGaZnO Nanowires from Amorphous Thin Film" *The 78th JSAP Autumn Meeting*, Fukuoka International Congress Center, Sep. 5-8, 2017. (Oral Presentation)

4. **J. C. Felizco**, M. Uenuma, D. Senaha, Y. Ishikawa, and Y. Uraoka, "Growth of InGaZnO Nanowires via Mo/Au-catalyzed Vapor-Liquid-Solid Process", *The 64th JSAP Spring Meeting*, Pacifico Yokohoma, March 14-17, 2017. (Oral Presentation)

Related Presentations

1. Y. Ikeguchi, M. Uenuma, **J. C. Felizco** and Y. Uraoka, "Influence of Material and Structure on Output Characteristics of Thin Film Thermoelectric Generator", *17th Annual Meeting of the Thermoelectric Society of Japan (Virtual)*, September 28-30, 2020. (Poster Presentation)

2. H. Murakawa, M. Uenuma, **J. C. Felizco** and Y. Uraoka, "Thermoelectric Properties in Thin Film with pn Junction", *The 17th European Conference on Thermoelectrics*, Limassol, Cyprus, Sep. 23-25, 2019. (Poster Presentation)

3. H. Murakawa, M. Uenuma, **J. C. Felizco**, Y. Ishikawa, and Y. Uraoka, "Evaluation and Application of p-type Thin Film Thermoelectric Materials", *The 80th JSAP Autumn Meeting*, Hokkaido University, Hokkaido, Sep. 18-21, 2019. (Poster Presentation)

4. M. Uenuma, K. Umeda, **J. C. Felizco**, D. Senaha, and Y. Uraoka, "Flexible TEG using Amorphous InGaZnO Thin Film", *37th International Conference on Thermoelectrics*, Congress Center, Caen, France, July 1-5, 2018. (Poster Presentation)

5. K. Umeda, M. Uenuma, D. Senaha, **J. C. Felizco**, Y. Uraoka and H. Adachi, "Amorphous Thin Film for Thermoelectric Application", *17th International Conference on Micro and Nanotechnology for Power Generation and Energy Conversion Applications (PowerMEMS 2017)*, Kanazawa, Japan, November 14-17, 2017. (Poster Presentation)

6. M. Uenuma, **J. C. Felizco**, D. Senaha, and Y. Uraoka , "Transparent Thin Film for Energy Harvesting", *17th International Conference on Micro and Nanotechnology for Power Generation and Energy Conversion Applications (PowerMEMS 2017)*, Kanazawa, Japan, November 14-17, 2017. (Oral Presentation)

Acknowledgements

I would like to express my deepest gratitude to those who helped make this research possible:

To the Lord Almighty, for granting me this once in a lifetime opportunity, and for giving me the wisdom, patience and understanding since day one. I praise You for the strength and guidance all throughout my graduate studies in NAIST.

To Prof. Yukiharu Uraoka, for warmly welcoming me to your lab and allowing me to work on this research for 4.5 years. I have learned a lot of things not only about science and engineering, but also about Japanese culture and everyday life. I will bring these lessons with me wherever the future may bring me.

To Assoc. Prof. Mutsunori Uenuma, my principal investigator for the whole duration of my study in NAIST, for being patient and supportive of me in every step of this research. It was an honor being mentored by a brilliant scientist.

To my other supervisors, Assoc. Prof. Yasuaki Ishikawa, Prof. Yoichiroh Hosokawa, and Prof. Tsuyoshi Kawai, for your wonderful insights that significantly improved my dissertation.

To my beloved members of the Information Device Science laboratory, Asst. Prof. Mami N. Fujii, Asst. Prof. Juan Paolo Bermundo, Asst. Prof. Michael Jallorina, Ms. Yukiko Morita, and all the students that I have met since 2016, for the meaningful discussions and delightful memories in the lab. I will always treasure every moment that I spent with all of you.

To Prof. Ilkka Tittonen, Dr. Taneli Juntunen, Dr. Camilla Tossi and Jarkko Etula from Aalto University, as well as Prof. Roland Schmechel and Dr. Franziska Maculewicz from University of Duisburg-Essen, for giving me the chance to collaborate with you and for giving

me your kind support for my research.

To the Materials Science technical staff, especially Mr. Noritake Koike, Mr. Yasuo Okajima, Mr. Kazuhiro Miyake, Mr.Masahiro Fujihara, Ms. Tomoko Ohno and Ms. Sakiko Fujita, for all the assistance that I have warmly received from all of you. Finishing my research would be impossible without your efforts.

To the NAIST Filipino community, and all the lovely friends and colleagues that I have met since 2016, for playing a big part in making NAIST feel like my home away from home.

And finally, to my family, and to Christian, for the unconditional love and unwavering support. You have been my inspiration in overcoming this endeavor.